

Electrical, Electrochemical, and Optical  
Characterization of Ceria Films

Thesis by  
Tae-Sik Oh

In Partial Fulfillment of the Requirements for the Degree  
of  
Doctor of Philosophy



CALIFORNIA INSTITUTE OF TECHNOLOGY  
Pasadena, California  
2013  
(Defended September 5, 2012)



## ACKNOWLEDGEMENTS

I spent six full years as a graduate student in Caltech, and the time here will be never forgotten. It will always be the most memorable days in my life.

Above all, I would like to thank my wife, Min Ji Hwang, for all the endless support and patience that carried me along my path to PhD. Without her, I could not do this. Now we are moving to yet another stage of our lives, and I cannot thank her enough for being there for me as always.

I should say that I was very lucky to have a wonderful advisor, Prof. Sossina Haile, who always encouraged me and had patience to wait whenever I needed more time than first thought. She is an absolute role model for all research group leaders. Hopefully I can be like her someday.

Gratefully, I had many friends in the lab with helping hands. I would like to thank Dr. Wei Lai, Dr. Peter Babilo and Dr. David Boyd for their kind support in the initial stage of my PhD course. Dr. William Chueh and Dr. Mary Louie taught me many things regarding science. It was my great pleasure to have them around when I wanted to talk about research and all other things in general. I hope to see them thrive in the world of science and look forward to seeing our paths come across either expectedly or unexpectedly. Dr. Evan Brown, Aron Varga, and Dr. Teruyuki Ikeda shared an office with me. My life in Caltech would have been much harder without them. I thank Dr. Ayako Ikeda for many tips from the first day in Haile Lab to the last. With Evan and Ayako, I was able to survive all the tough classes here. Chatr, Rob, BG, Chih-Kai, Vanessa, Dr. Yong Hao and Dr. Yoshihiro Yamazaki were all excellent lab members to work with. Dr. WooChul Jung and Dr. Jaemin Kim made Haile Lab more “Koreanized.” I enjoyed their presence and their advice from experience very much. I also thank Dr. Marion Martin and Eugene with whom I spent many hours in Thomas. They gave me a lot of energy when I felt down.

I also thank friends in Caltech Korean community. They are all warm-hearted, brilliant and cheerful. My family owe much to them in every possible way.

Members at Logos Church and Pasadena Presbyterian Church showed their love to my family. I deeply appreciate it.

My extended family in Korea always supported me from the other side of the Pacific Ocean from day 1. I am happy to show them that their efforts indeed came through.

Lastly, I would like to thank my daughter, Kaylee Sehee Oh, who always makes me laugh even when nothing works out. With that, I can come back next day and fight on.

## ABSTRACT

Acceptor-doped ceria has been recognized as a promising intermediate temperature solid oxide fuel cell electrode/electrolyte material. For practical implementation of ceria as a fuel cell electrolyte and for designing model experiments for electrochemical activity, it is necessary to fabricate thin films of ceria. Here, metal-organic chemical vapor deposition was carried out in a homemade reactor to grow ceria films for further electrical, electrochemical, and optical characterization. Doped/undoped ceria films are grown on single crystalline oxide wafers with/without Pt line pattern or Pt solid layer. Deposition conditions were varied to see the effect on the resultant film property. Recently, proton conduction in nanograined polycrystalline pellets of ceria drew much interest. Thickness-mode (through-plane, z-direction) electrical measurements were made to confirm the existence of proton conductivity and investigate the nature of the conduction pathway: exposed grain surfaces and parallel grain boundaries. Columnar structure presumably favors proton conduction, and we have found measurable proton conductivity enhancement. Electrochemical property of gas-columnar ceria interface on the hydrogen electrooxidation is studied by AC impedance spectroscopy. Isothermal gas composition dependence of the electrode resistance was studied to elucidate Sm doping level effect and microstructure effect. Significantly, preferred orientation is shown to affect the gas dependence and performance of the fuel cell anode. A hypothesis is proposed to explain the origin of this behavior. Lastly, an optical transmittance based methodology was developed to obtain reference refractive index and microstructural parameters (thickness, roughness, porosity) of ceria films via subsequent fitting procedure.



# Table of Contents

<b>List of Figures.....</b>	<b>ix</b>
<b>List of Tables.....</b>	<b>xi</b>
<b>List of Symbols and Notations.....</b>	<b>xii</b>
<b>1. Introduction and background.....</b>	<b>1</b>
1.1 Motivation.....	1
1.2 Fuel cells.....	2
1.2.1 Fuel cell operation principles.....	2
1.2.2 Fuel cell efficiency.....	7
1.2.3 Fuel cell types.....	9
1.3 Thin films for fuel cell application .....	10
1.3.1 Relevance of thin film technology .....	10
1.3.2 State of the art thin/thin film technology.....	11
1.3.3 Chemical vapor deposition for solid oxide fuel cells .....	13
1.4 Thin films characterization .....	14
1.4.1 Electrical characterization .....	14
1.4.2 State of the art thin/thin film technology.....	15
1.4.3 Chemical vapor deposition for solid oxide fuel cells .....	18
<b>2. Film fabrication.....</b>	<b>20</b>
2.1 Introduction.....	20

2.1.1 Chemical vapor deposition of ceria for fuel cell application .....	21
2.1.2 Precursors .....	21
2.1.3 Doping.....	22
2.1.4 Preferred orientation .....	23
2.2 Fabrication details .....	25
2.2.1 CVD reactor setup.....	25
2.2.2 CVD procedure .....	27
2.2.3 Deposition process parameters .....	28
2.2.4 Film morphology .....	29
2.2.5 Doping level control .....	30
2.2.6 Preferred orientation control .....	31
2.2.7 Rocking curves.....	33
<b>3 Electrical characterization.....</b>	<b>35</b>
3.1 Summary .....	35
3.2 Introduction.....	36
3.3 Cell configuration & materials characterization .....	37
3.4 Electrical characterization.....	42
3.5 Conclusion .....	51
<b>4 Electrochemical characterization.....</b>	<b>53</b>
4.1 Summary .....	53
4.2 Introduction.....	54
4.2.1 Electrode resistance .....	54

4.2.2 Background and experiment design.....	55
4.3 Sm doping level effect .....	63
4.4 Preferred orientation effect .....	71
4.5 Asymmetric cell measurement.....	77
4.5.1 Metal comparison at OCV .....	77
4.5.2 Impedance analysis under bias.....	82
4.6 Conclusion .....	89
<b>5 Optical characterization .....</b>	<b>90</b>
5.1 Summary .....	90
5.2 Introduction.....	91
5.3 Experimental methods .....	92
5.3.1 Sample preparation.....	92
5.3.2 Transmittance measurement.....	93
5.3.3 Auxiliary measurements.....	95
5.4 Transmittance modeling.....	95
5.4.1 Ideal thin film and envelope method.....	95
5.4.2 Transmittance of rough films .....	97
5.4.3 Transmittance of porous films.....	98
5.4.4 Sellmeier dispersion and reference refractive index determination .....	100
5.4.5 Fit parameter uncertainties .....	101
5.5 Results and discussion .....	102
5.5.1 Optical parameter .....	102

5.5.2 Microstructural parameter .....	110
5.6 Conclusion .....	119
<b>6 Summary and Conclusions .....</b>	<b>121</b>
 <b>Appendix A ACIS (alternating current impedance spectroscopy) .....</b>	<b>123</b>
A.1 ACIS principles .....	123
A.2 Impedance of individual circuit elements .....	126
A.3 Impedance of combined circuit elements .....	127
A.4 Constant phase element (CPE) .....	130
 <b>Appendix B Optical transmittance .....</b>	<b>133</b>
B.1 Transmittance basics .....	133
 <b>Appendix C Effective medium theory .....</b>	<b>136</b>
C.1 Effective medium theory basics .....	136
 <b>Appendix D Thin film characterization by X-ray .....</b>	<b>141</b>
D.1 X-ray diffraction .....	141
D.2 X-ray reflection .....	142
 <b>References .....</b>	<b>145</b>

# List of Figures

Figure 1.1: Schematic fuel cell polarization and power density curve .....	5
Figure 2.1: Electrochemical vapor deposited dense films of SDC .....	20
Figure 2.2: Electrochemical vapor deposition setup.....	21
Figure 2.3: Precursor structure and thermal behavior.....	22
Figure 2.4: Schematic view of an MOCVD setup.....	23
Figure 2.5: Precursor effect on preferred orientation .....	24
Figure 2.6: Experimental setup of the homemade MOCVD reactor .....	25
Figure 2.7: Precursor evaporator design .....	26
Figure 2.8: SEM images of Ceria films .....	29
Figure 2.9: Depth profile for a film with nonuniform dopant concentration.....	30
Figure 2.10: Depth profiles for films with in situ dopant level control .....	31
Figure 2.11: $\theta$ - $2\theta$ scans of ceria films .....	32
Figure 2.14: Omega scans about (200) peak for undoped ceria films on MgO.....	33
Figure 2.15: Omega scans about (200) peak for undoped ceria films on YSZ.....	34
Figure 3.1: Schematic view of thickness-mode measurement sample.....	38
Figure 3.2: Representative SEM images of samples .....	40
Figure 3.3: $\theta$ - $2\theta$ scans of ceria films before and after annealing.....	42
Figure 3.4: Impedance arcs at fixed temperature with different water vapor pressure .....	43
Figure 3.5: Normalized arcs superposition .....	44
Figure 3.6: Effective DC properties of film 1 .....	46
Figure 3.7: Arc deformation metric behavior .....	48
Figure 3.8: Resistivity isotherms.....	50
Figure 4.1: Polarization curve of an electrode .....	54
Figure 4.2: Gas composition map .....	56
Figure 4.3: Cell sketches for symmetric measurements and asymmetric measurements.....	58
Figure 4.4: Sm cation molar fractions.....	60
Figure 4.5: Top down view of the YSZ (100) substrate with platinum line pattern atop.....	60

Figure 4.6: $\theta$ - $2\theta$ scans for SDC films grown with different deposition pressures.....	61
Figure 4.7: Superposition of impedance arcs without area normalization.....	62
Figure 4.8: A proposed explanation for the origin of the high frequency arc.....	62
Figure 4.9: Impedance spectrum of SDC painted electrode on Pt paste current collector ...	63
Figure 4.10: ASR behavior map for two doping levels (3Torr films) .....	65
Figure 4.11: ASR behavior map for two doping levels (10Torr films) .....	68
Figure 4.12: Impedance arcs for films grown at different pressures.....	69
Figure 4.13: ASR behavior map for films grown at different pressures .....	70
Figure 4.14: Offset resistance is assumed to stem from the spreading resistance .....	75
Figure 4.15: ASR comparisons for the three metals at OCV condition.....	76
Figure 4.16: Impedance arcs under bias.....	77
Figure 4.17: Variation of electrochemically active area under bias.....	78
Figure 4.18: Oxygen chemical potential profiles under anodic bias.....	79
Figure 4.19: ASR comparisons of Ni and Pt under 4 biased conditions.....	80
Figure 4.20: Impedance arcs superposed for various biases .....	80
Figure 5.1: Transmittance measurement setup .....	85
Figure 5.2: Simulated dispersion behavior of refractive index .....	91
Figure 5.3: Microstructural images of dense PLD films .....	96
Figure 5.4: Transmittance analysis for dense PLD films .....	96
Figure 5.5: Derived dispersion behavior of PLD grown films.....	98
Figure 5.6: Transmittance analysis and XRR for porous undoped CVD films .....	104
Figure 5.7: Transmittance analysis for porous undoped PLD films .....	104
Figure 5.8: Transmittance analysis for ultra-thin CVD films.....	109
Figure 5.9: XRR for an ultra-thin CVD film .....	109
Figure 5.10: Surface maps .....	110
Figure 5.11: X-ray rocking curves .....	111
Figure A.1: AC impedance measurement scheme.....	117
Figure A.2: Two common impedance data presentations .....	117
Figure A.3: Impedance spectrum and corresponding fit .....	121
Figure A.4: ZARC circuit impedance Nyquist plot.....	123

Figure A.5: Distribution of relaxation times .....	124
Figure C.1: Graphical description of effective medium theory.....	128
Figure C.2: Effective dielectric constant of a mixture.....	132
Figure D.1: Bragg-Brentano geometry for typical X-ray diffractometer.....	133
Figure D.2: XRR pattern example and interpretation.....	135
Figure D.3: XRR pattern examples .....	136

## List of Tables

Table 1.1: Candidate fuel cell reactions and their open cell potentials.....	8
Table 1.2: Summary of thin/thick film techniques in solid oxide fuel cell study .....	12
Table 2.1: Governing factors for thin film structure evolution .....	24
Table 2.2: Film growth parameters for doped/undoped ceria film deposition .....	28
Table 3.1: Film growth conditions for chemical vapor deposition of undoped ceria.....	38
Table 3.2: Physical characteristics of films used for electrochemical measurements .....	41
Table 4.1: Gas reaction order and ASR trend on Sm doping levels.....	66
Table 4.2: Summary of the three films with different deposition pressures .....	71
Table 4.3: Gas reaction order and ASR trend for orientation controlled films.....	72
Table 5.1: Summary of ceria film characteristics .....	95
Table 5.2: Dispersion relation fit parameters and Wemple-DiDomenico energy terms obtained for dense PLD films on YSZ(100). .....	101
Table 5.3: Comparison between measured and fit microstructural parameters for dense, flat, thick ceria PLD films.....	103
Table 5.4: Summary of microstructural fit parameters obtained from transmittance spectra analysis .....	106
Table 5.4: Summary of fitting results for ultra-thin films .....	108
Table A.1: Nyquist plot on impedance/admittance plane for combined elements .....	120

# List of Symbols & Notations

$n$	number of electrons
$F$	Faraday's constant
$E_r$	thermodynamic reversible cell potential (Nernst voltage)
$\delta$	oxygen nonstoichiometry
$\eta$	overpotential
$\eta_{\text{thermo}}$	thermodynamic efficiency
$\omega$	angular frequency or incident angle of the X-ray
$Z$	complex impedance
$Y$	complex admittance
$C$	capacitance
$R$	resistance
$M$	complex modulus
$L$	inductance
$T$	transmittance
$n$	real part of complex refractive index
$\varepsilon$	dielectric constant
$I_{111}$	intensity of X-ray diffracted beam from (111) atomic plane
$\mu_{\text{O}}$	chemical potential of atomic oxygen
$h$	Planck's constant
$c$	speed of light



**Abbreviations**

ACIS	AC impedance spectroscopy
ALD	atomic layer deposition
AFM	atomic-force microscopy
ASR	area-specific resistance
BSCF	$\text{Ba}_{0.5}\text{Sr}_{0.5}\text{Co}_{0.8}\text{Fe}_{0.2}\text{O}_{3-\delta}$
EDS	X-ray energy dispersive spectroscopy
GDC	Gd doped $\text{CeO}_2$
HF	high frequency
LF	low frequency
LSGM	$\text{La}_{0.9}\text{Sr}_{0.1}\text{Ga}_{0.8}\text{Mg}_{0.2}\text{O}_3$
LSC	$\text{La}_{0.6}\text{Sr}_{0.4}\text{CoO}_3$
LSM	$\text{La}_{0.8}\text{Sr}_{0.8}\text{MnO}_3$
MOCVD	metal-organic chemical vapor deposition
OCV	open circuit voltage
PLD	pulsed-laser deposition
SDC	Sm-doped $\text{CeO}_2$
SEM	scanning electron microscopy
SOFC	solid oxide fuel cell
SWLI	scanning white light interferometry
XRD	X-ray diffraction
XRR	X-ray reflection
YSZ	yttria-stabilized zirconia

# Chapter 1

## Introduction and background

### 1.1 Motivation

The most urgent challenge to humankind at the moment is the energy problem.. There are varieties of research activities all over the world to meet this grand challenge of environment-friendly, sustainable energy for the future. It is hard to imagine that there will be one energy conversion technology that will solve all the aspects of complicated energy landscape. Fuel cells have long been considered to make significant contribution due to its high efficiency and its compatibility with the existing energy consumption pattern. Since Grove's pioneering work on fuel cells [1], it has found applications under special circumstances such as power source for space shuttles and unmanned air vehicles. However, even though fuel cells are already proven to perform as a steady power source, widespread acceptance has not been achieved mostly due to its high cost per electricity generated.

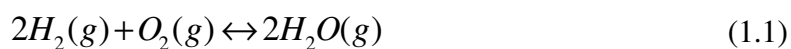
This can be changed if we can develop a high power density ( $>2\text{W}/\text{cm}^2$ , current state of the art [2]) solid oxide fuel cell operating at the intermediate temperature (400~700°C) that is compatible with mass production. To do this, fundamental understanding of the related material's bulk property and interface/surface property is required to make rational fuel cell design possible. The material of interest is ceria which can serve as a solid electrolyte in oxidizing condition and electrode in reducing condition. In this work, we aim for a fabrication route that is already widespread in microelectronics

industry for mass production: chemical vapor deposition. Chemical vapor deposition of ceria has been done before; however, it is very rarely done in the context of fuel cell application. Electrical, electrochemical, and optical property of ceria films grown by metal-organic chemical vapor deposition were investigated since electrical (chapter 3) and electrochemical (chapter 4) aspects can provide valuable information in fuel cell design while optical aspects (chapter 5) are related to thermo-chemical water-splitting process based on solar radiative heating. Impact of thin film microstructure on resultant properties is of most interest throughout this study.

## 1.2 Fuel cells

### 1.2.1 Fuel cell operation principles

Fuel cells are electrochemical energy conversion device that generate electricity from energy stored in chemical bonds. Any chemical reaction with negative  $\Delta G$  (Gibbs free energy difference,  $\Delta G = \sum G_{\text{(PRODUCTS)}} - \sum G_{\text{(REACTANT)}}$ ) can be utilized as long as it can be separated into two half-reactions occurring at the electrodes with appropriate electrolyte in the middle that conducts current carrying ions. For solid oxide fuel cells, oxygen ions and protons are two common ions that transport charges in the solid electrolytes. In the case of hydrogen fuel, the global reaction is a simple water generation reaction.



The forward reaction is for the fuel cell operation resulting in electrical current through outer circuit and concomitant electrical work (powering up light bulbs, etc.) from

the system. The reverse reaction is water splitting in solid oxide electrolyzer cell operation consuming electrical energy to generate hydrogen fuel.

From thermodynamics, it is known that the maximum nonexpansion (hence, electrical) work from a system is related to Gibbs free energy change,  $\Delta G$ . The well-known Nernst equation relates  $\Delta G$  and the thermodynamic reversible cell potential,  $E_r$  at the equilibrium.

$$\Delta G = -nFE_r \quad (1.2)$$

Here,  $n$  is the number of electrons going around the external circuit per one overall reaction, and  $F$  is Faraday constant [3]. For a reaction as in Eq. (1.1),  $n$  equals 4. Considering that  $\Delta G$  is dependent on the chemical potentials of products and reactants, we can get  $E_r$  under realistic fuel cell operation condition (still, no current flowing) as follows;

$$E_r(T, i=0) = E^\circ(T) + \frac{RT}{4F} \ln P_{O_2}^{(cathode)} + \frac{RT}{2F} \ln \frac{P_{H_2}^{(anode)}}{P_{H_2O}^{(anode)}} \quad (1.3)$$

$R$  and  $T$  have usual meaning, and  $E^\circ(T)$  is the cell potential when all the gases assume standard pressure making this quantity as a function of temperature only. In a typical SOFC (solid oxide fuel cell) operation condition,  $E_r$  turns out to be 1.13~1.18 V [4]. Considering gas phase equilibrium between water vapor, hydrogen and oxygen at the anode chamber, one can reduce equation (1.3) into more simple expression.

$$E_r = \frac{RT}{4F} \ln \frac{P_{O_2}^{(cathode)}}{P_{O_2}^{(anode)}} \quad (1.4)$$

Thus, one can regard a fuel cell with oxygen-ion conducting electrolyte as an oxygen concentration cell. If the electrolyte conducts protons, then one considers gas phase

equilibrium at the cathode chamber since water evolves at the cathode in this case. Then, one can view the fuel cell as a hydrogen concentration cell. However, equation (1.4) holds only when the electrolyte conducts ions exclusively as in the case of zirconia-based oxygen sensor. If there is an electronic conduction in the electrolyte, internal leakage current occurs and resultant open circuit voltage (OCV) is less than what Nernst equation predicts. Rigorous derivation of this effect demands Wagner's theory on oxygen concentration cell [5]. According to Wagner, an electrical potential develops across a given binary oxide such that

$$E = -\frac{1}{F} \int_{\mu_{O,anode}}^{\mu_{O,cathode}} \frac{t_{ion}}{z_O} d\mu_O, \quad (1.5)$$

where  $F$  denotes Faraday constant,  $t_{ion}$  the overall ion transference number including all mobile ionic species, and  $Z_O$  the valence of the oxygen ion ( $Z_O = -2$ ). Thus, the theoretical voltage depends on the “average” ionic transference number across the oxygen partial pressure range of operation. Typical anode oxygen partial pressure is  $10^{-20}$  bar, and typical cathode oxygen partial pressure is 1bar. When the electrolyte is not a binary compound, this argument still holds if the constituent cations are practically immobile [6].

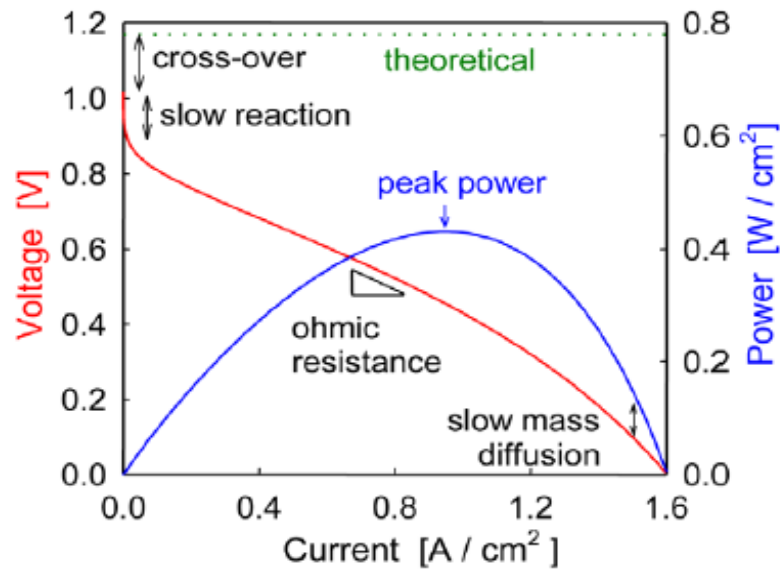


Figure 1.1 Schematic fuel cell polarization and power density curve [7].

In practice, without drawing current, OCV assumes further reduced value from theoretical voltage due to fuel cross-over as seen in Fig.1.1. This effect is less severe in SOFC compared to the polymer based fuel cells. This occurs by the anode-cathode gas mixing through the microcracks in the electrolytes. The result is a molar transfer of gas from one to another electrode and subsequent global reaction without producing electric current. Thus, thin dense gas tight layer of electrolyte is desired.

Under realistic fuel cell operation condition (trade-off point between efficiency and peak power), the cell voltage becomes lower than the OCV due to three major loss components: ohmic, activation, concentration.

Fig.1.1 shows the typical polarization curves of a SOFC and power density curves. In this figure, one can see that the activation overpotential dominates when the current density is low, and the concentration overpotential occurs in the highest current range. The ohmic loss is linearly dependent on the current density with simple ohm's law behavior.

This loss is minimized when the thickness of the electrolyte is reduced. However, one needs to pay close attention to the electrolyte thickness control if the electrolyte in use can show electronic conductivity in reducing condition. In this case, thin electrolyte can have severe leakage current between two electrodes. For Sm-doped ceria electrolyte, a theoretical simulation has been performed to predict the best electrolyte thickness [8].

The activation overpotential is often modeled by the well known Butler-Volmer equation [9] in electrode kinetics even though it is not always clear that charge transfer is indeed the rate-determining step. There are two different activation overpotentials in a cell, one comes from the cathode reaction and the other comes from the anode reaction. Usually, cathode reaction is the sluggish one and larger part of the activation overpotential comes from this step. Fundamental reason is that oxygen molecules are very stable requiring high energy to break the oxygen-oxygen bond [4]. It is hard to make an oxygen gas molecule to separate from each other and take two oxygen lattice sites in the bulk ceramic solid. On the contrary, oxidation of the hydrogen is relatively easier. Therefore, it is common practice to support a single cell with the thick anode that has lower overpotential compared to cathode overpotential. In addition, one can expect in-situ reforming of hydrocarbon fuel to occur in the porous, thick body of the anode. If cathode overpotential is less than anode overpotential, then one can consider thick cathode as a supporting layer.

Gas phase mass transport can be rate determining if its rate is slower than the reaction rate at the electrodes. As greater current is drawn, the reactant depletion layer right above solid surface thickens and by-products accumulate at the solid-gas interface leading to eventual mass transport control. In reality, a fuel cell will never operate in this current range since peak power density is achieved at lower current level, and better efficiency will

be achieved at even lower current density. In reality, a fuel cell operates in a current range which compromises the peak power and best efficiency.

In sum, the cell voltage at finite current density,  $j$ , can be written as

$$E(j) = E_{OCV} - \eta_{electrolyte}^{ohmic} - \eta_{anode}^{activation} - \eta_{cathode}^{activation} - \eta_{anode}^{concentration} - \eta_{cathode}^{concentration} \quad (1.6)$$

There are analytical expressions reported in literature for these respective terms, and one can fit the I-V polarization curve to extract individual contributions to losses [10].

### 1.2.2 Fuel cell efficiency

The distinct merit of a fuel cell relies on its high energy conversion efficiency, at least in the thermodynamic sense. Conventional thermodynamic efficiency for a thermo-mechanical system is given as [11]

$$\eta_{thermo.} = \frac{\Delta G}{\Delta H} = \frac{\Delta H - T \Delta S}{\Delta H} = 1 - T \frac{\Delta S}{\Delta H} \quad (1.7)$$

This definition regards  $\Delta H$  as maximum available energy. This causes problem since there are reactions with positive entropy change accompanying negative enthalpy change making the efficiency larger than 1 as seen in table 1.1. In this definition, the extra energy flowing into the system from surroundings to keep the system isothermal becomes available for electrical work conversion. Instead of  $\Delta H$  (a maximum mechanical work available, and historically used for fuel cell systems), if we use  $\Delta G$ , the maximum non-expansion work available (electrical work is non-expansion work), then the thermodynamic efficiency of the fuel cell becomes just 1. The point here is that fuel cells are very efficient in thermodynamic perspective. All losses are related to kinetics and practical limitations.



Fuel cell efficiency is not determined by the Carnot efficiency, which is the limiting factor for internal combustion engines.

This imposes fundamental difference in terms of temperature dependence of the efficiency. In a Carnot cycle, as  $T_{\text{high}}$  increases, thermodynamic efficiency also increases. In a  $\text{H}_2/\text{O}_2$  fuel cell, for example, as operational temperature increases the thermodynamic efficiency as in Eq. (1.7) decreases. The cross-over is around  $700^\circ\text{C}$  when one assumes the rejection temperature  $T_{\text{low}}$  of the Carnot cycle is at  $0^\circ\text{C}$  [12]. Above this temperature, Carnot cycle has higher efficiency than a  $\text{H}_2/\text{O}_2$  fuel cell. Disregarding the slower kinetics at lower temperature, a  $\text{H}_2/\text{O}_2$  fuel cell performs better, in theory, at lower temperature range. Comparing to a coal power plant, a fuel cell bypasses the heat and mechanical work step in electricity generation leading to its higher efficiency. Furthermore, fuel cell efficiency is independent of the size (in terms of number of megawatts), which supports its applicability as distributed power sources.

Table 1.1 Candidate fuel cell reactions and their open cell potentials  $E^\circ$  ( $T=25^\circ\text{C}$ ) [11]

Reaction	$-\Delta G^\circ$ (kJ/mol)	$-\Delta H^\circ$ (kJ/mol)	$\Delta G^\circ/\Delta H^\circ$	$-T\Delta S^\circ$ (kJ/mol)	$E^\circ$ (Volt)
$\text{H}_2 + \frac{1}{2} \text{O}_2 = \text{H}_2\text{O}$	237.1	285.8	0.83	-48.7	1.23
$\text{C} + \text{O}_2 = \text{CO}_2$	394.4	393.5	1.002	0.86	1.02
$\text{C} + \frac{1}{2} \text{O}_2 = \text{CO}$	137.2	110.5	1.24	26.6	1.42
$\text{CO} + \frac{1}{2} \text{O}_2 = \text{CO}_2$	257.2	283.0	0.91	-25.8	1.33

### 1.2.3 Fuel cell types

Fuel cells are categorized by electrolyte materials. Depending on which electrolyte is in use, the operational temperature of that fuel cell is determined. At the lowest temperature end, polymer-based electrolyte supports high ionic conductivity ( $\text{H}_3\text{O}^+$  conduction) below  $110^\circ\text{C}$ . Low operational temperature is convenient for rapid start-up; however, precious metal catalyst such as platinum is needed to facilitate sluggish electrode reactions, and water management brings up additional complication. At the highest temperature end, solid oxide-based electrolyte can conduct oxygen ions fast enough (ion conductivity of Sm-doped ceria at  $650^\circ\text{C} \sim 0.025 \text{ S/cm}$  [13]) with relatively high electrode kinetics due to high temperature. There is no need for precious metal catalyst. In addition, at high temperature it is easier to break C-C bonds so that hydrocarbons can be utilized without external reforming [14]. This fuel diversity is also a merit for solid oxide fuel cells making itself a bridging technology to the pure hydrogen fuel era. These characteristics of solid oxide fuel cell make itself an attractive energy conversion device, and we focus on this type of fuel cell. However, rapid start-up is not possible, and more importantly, expensive high temperature compatible materials are needed for construction. This motivates current research efforts to reduce the operational temperature of SOFC while maintaining advantages coming from high temperature operation. This concept is called intermediate temperature ( $400\sim 700^\circ\text{C}$ ) SOFC. For instance, low operational temperature may allow usage of ferritic stainless steel for interconnects rather than expensive ceramic-based interconnects or high-chrome alloy interconnects [15]. It also reduces thermal stress and chemical reaction between components; thus, longer life time is expected for lower operational temperature [16]. However, Low operation temperature introduces necessary

changes in SOFC design. The electrolyte should be changed from zirconia-based to ceria-based or lanthanum gallate-based due to low ionic conductivity of zirconia-based electrolytes. The thickness of the electrolyte should be decreased ( $<20\mu\text{m}$ ) to minimize ohmic overpotential while suppressing leakage current through the electrolyte. Furthermore, electrode activation overpotential becomes a limiting factor at low temperature where thermally activated electrochemical/electrical processes get sluggish. To achieve low electrode activation overpotential at intermediate temperature, it is necessary to focus on technologically relevant electrochemical system; for example, ceria-based electrode exposed to fuel gas.

## **1.3 Thin films for fuel cell application**

### *1.3.1 Relevance of thin film technology*

Thin film technology was not involved in fuel cell fabrication in its initial development. The 1<sup>st</sup> generation fuel cell featured thick electrolyte (100~200 $\mu\text{m}$ ) that supports both cathode and anode [17]. To lower the operational temperature, as already mentioned in preceding section, the thickness of the electrolyte should be decreased. In this geometry, electrolyte is no longer the thickest part that mechanically supports the whole assembly. One of the two porous electrodes should support the thin, dense electrolyte. Thin film deposition can produce thin and dense electrolyte supported on porous electrode. This was the main motivation to turn to thin film technology for fuel cell fabrication. In practice, electrolyte depositions have been made directly on porous electrode [18] or on dense composite electrode with subsequent pore generation step [2, 19].

Application of thin film technology is not limited for electrolyte fabrication. It can be used for high performance electrode fabrication with the possibility to produce nano-structured material with high surface area [20, 21]. Another driving force to use thin film technology in electrode fabrication comes from the need of model electrode. With porous electrode structure as in the real operating fuel cell, it is hard to control the microstructure (especially, triple phase boundary where gas, electrode, and electrolyte meet or dual phase boundary where two out of the three components meet) so that clear interpretation on sample electrochemical response is hard to get. For fundamental understanding on fuel cell electrochemistry, it is required to have a dense electrode, typically in disc shape, with controlled physical dimensions such as diameter and height [22, 23].

### 1.3.2 *State of the art thin/thick film technology*

Thin/thick film technology has been adopted in fuel cell fabrication especially for the dense, gas-tight, thin electrolyte fabrication. In industry, vacuum-free ceramic process techniques are widely used. Screen-printing is the state-of-the-art electrolyte fabrication method mainly due to low cost and scalability [17]. Vacuum-based methods are not yet realized in industry level for solid oxide fuel cell fabrication even though they are widely used in microelectronics industry. Sputtering [18], pulsed laser deposition [2] and atomic layer deposition [19] are demonstrated in literature for electrolyte fabrication. Among these vacuum-based methods, pulsed laser deposition (PLD), a proven tool for oxide film fabrication, has been the method of choice in model electrode fabrication with defined geometric parameters and negligible porosity [22, 23]. Fuel cells with PLD-derived thin

film electrolyte have shown record-high power density [2]. Even though PLD has found wide application in the fundamental research, especially for dense electrolyte film fabrication, it has a huge disadvantage; scaling up is not trivial for this method. Table 1.2 summarizes thin/thick film technologies adopted in solid oxide fuel cell literature. Only one or two papers are presented for each technique.

Table 1.2 Summary of thin/thick film techniques in solid oxide fuel cell study.

	Technique	Achievements in literature
Vacuum	Pulsed laser deposition [2,24]	Dense LSGM electrolyte (~5 $\mu\text{m}$ ) Deposition on dense anode (NiO(Fe <sub>3</sub> O <sub>4</sub> )– SDC mixture) Anode later becomes porous upon reducing. 2Wcm <sup>-2</sup> at 600°C
		Dense electrode films (~2 $\mu\text{m}$ ) Materials : Sm-doped CeO <sub>2</sub> Deposition on YSZ wafer Model system to study electrochemistry of hydrogen electrooxidation.
	Sputtering [18, 25]	Dense YSZ electrolyte (~5 $\mu\text{m}$ ) Negative DC bias on porous LSM cathode substrate with pore size ~0.5 $\mu\text{m}$
		Dense YSZ electrolyte (50~150nm) Deposition on silicon wafer. Etching process to remove silicon.
	Atomic layer deposition [19]	Dense YSZ electrolyte (~80nm) Deposition on corrugated silicon
Nonvacuum	Screen printing [26, 27]	Porous LSC cathode (~5 $\mu\text{m}$ ) printed on polycrystalline SDC electrolyte
		Dense YSZ electrolyte (~15 $\mu\text{m}$ ) printed on NiO+YSZ 0.95Wcm <sup>-2</sup> at 700°C

	Spray pyrolysis [28]	Porous LSCF cathode (200~250nm) Deposited on PLD YSZ electrolyte
	Electrophoretic deposition [29]	Dense electrolyte films Materials : LSGM, YSZ, GDC

LSGM -  $\text{La}_{0.9}\text{Sr}_{0.1}\text{Ga}_{0.8}\text{Mg}_{0.2}\text{O}_3$ , SDC - Sm-doped  $\text{CeO}_2$ , LSM -  $\text{La}_{0.8}\text{Sr}_{0.8}\text{MnO}_3$ , LSC -  $\text{La}_{0.6}\text{Sr}_{0.4}\text{CoO}_3$ , GDC - Gd doped  $\text{CeO}_2$ , YSZ – yttria stabilized zirconia

### 1.3.3 Chemical vapor deposition for solid oxide fuel cells

We chose metal-organic chemical vapor deposition for ceria thin film fabrication. This choice is based on three merits of chemical vapor deposition. Chemical vapor deposition is easy to scale up, making itself a suitable fabrication tool for microelectronics industry. One can design a CVD chamber that can handle a batch process with multiple substrates in one deposition run [30]. CVD also gives conformal coating, which becomes important when the substrate surface has roughness or complex morphology. For electrolyte deposition, it is desired to adopt a deposition tool that can tolerate the realistic surface irregularity of SOFC electrode substrates. This will also make the scale-up easy unless we want to prepare polished electrode surfaces in a mass production process. For electrode fabrication, one can think of coating complex current collecting backbone structure with electrochemically active electrode material. This enables flexible design for electrode structure. Lastly, CVD process can produce films with high purity [30]. High purity materials (carbon nanotubes [31], SiC [32],  $\text{TiO}_2$  and  $\text{ZrO}_2$  [33]) have been obtained by chemical vapor deposition.

There are not many reports that utilized chemical vapor deposition in fuel cell related studies. Most of the study focused on the fabrication itself with no application/characterization towards fuel cell operation. Yttria-stabilized zirconia (YSZ) has a long history as a solid electrolyte, and hence more reports are available for YSZ films grown by MOCVD. Chour deposited YSZ films on yttria doped ceria polycrystalline disc and measured OCV (0.87V at 650°C). Before CVD deposition of YSZ, the OCV was 0.7V at 650°C [34]. This increase means either closing out of open channels or higher average ion transference number. Given the small YSZ film thickness (2~5µm) compared to total disc thickness, it is likely that OCV increased by closing out pores. However, this demonstration is far from real fuel cell situation since the yttria doped ceria substrate disc was not porous. For fuel cell application, the substrate (electrode) should have enough porosity for facile gaseous product removal and reactant arrival. This is reported recently using porous cathode as a substrate. The OCV is measured at 0.66V at 925°C [35]. However, for ceria CVD films, OCV measurements have never been reported.

## **1.4 Thin film characterization**

### *1.4.1 Electrical characterization*

Electrical conductivity measurement on fuel cell related thin/thick film materials have been reported. In most cases, the in-plane conductivity is measured due to experimental simplicity. The substrate, in principle, should be resistive to suppress currents through it. In AC impedance measurements, it is possible and necessary to compensate the influence of the substrate [36]. Through-plane conductivity is less often measured since it is

challenging due to measurement geometry. It is important to suppress pin-hole generation to avoid short circuiting. This is close to the real fuel cell operational condition. In a thin film electrolyte, the ionic current is along the film thickness direction. The substrate should be conductive in this case. Pt coated oxide wafer, or silicon substrate has been the choice in literature. The influence of the substrate is negligible in this geometry.

There are two main directions in electrical characterization of fuel cell related thin film materials. First is to investigate the effect of strain or substrate-film interface effect using epitaxial film. Doped/undoped ceria films [37] and yttria-stabilized zirconia films [38] have been studied in in-plane geometry. Second is to study the effect of internal/external interface (grain boundaries/grain surfaces) in nanograined structure achieved from thin film deposition [39]. Thin film deposition process usually occurs at much lower temperature than conventional ceramic sintering. Thus, the grain growth is suppressed. With adjustment of deposition parameters (choice of substrate and deposition pressure, for example), it is possible to obtain polycrystalline, nanograined film. In this work (chapter 3), we focus on this second area of study since we intend to investigate the effect of the aligned grain internal/external surface on proton conductivity of ceria film.

#### 1.4.2 *Electrochemical characterization*

Electrochemistry on dense thin film electrode with full density has been studied for cathode materials [22, 23, and 40] as well as anode materials [24]. Pulsed laser deposition has been the fabrication tool that produces pore-free structure for fundamental study. There are two approaches for pore-free model electrodes. One is the patterned electrode, and another is microelectrode. In patterned electrode geometry, the electrode pattern width and



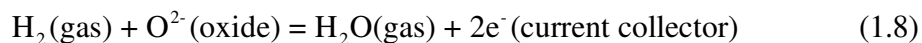
spacing between pattern lines can be controlled independently. This enables variation of triple phase boundary (gas-electrode-electrolyte interface) density while keeping dual phase boundary (either gas-electrode or electrode-electrolyte interface) density at the same level, or vice versa. This method has been proved to be effective in unambiguous determination of the electrochemically effective phase of the composite electrode [24].

Microelectrode is a modernized version of the classical point electrode. With precise dimension control, typical strategy involves variation of the radius and height of the disc shaped microelectrodes. Triple phase boundary is confined around the circumference of the disc (proportional to radius), and dual phase boundary is proportional to the circular area of the microelectrode (proportional to radius<sup>2</sup>). Thus, one can change the radius of the microelectrode at fixed height and see how the electrode resistance scales. If resistance scales with radius, then it can be concluded that rate determining step of the electrochemical reaction occurs at the triple phase boundary [22, 23]. If resistance scales with radius<sup>2</sup>, then the rate determining step should be the interface reaction (either gas-electrode or electrode-electrolyte interface). To determine which dual phase boundary is important, one can insert an interlayer between electrode and electrolyte to see its impact. In the case of  $\text{SrTi}_{1-x}\text{Fe}_x\text{O}_{3-\delta}$  cathode, the gadolinium doped ceria interlayer did not impact on the electrode resistance leading to a conclusion that the surface reaction occurring gas-electrode interface is rate determining [41].

Porous thin film electrodes were also studied with focus on performance.  $\text{Sm}_{0.5}\text{Sr}_{0.5}\text{CoO}_{3-\delta}$ - $\text{Sm}_{0.1}\text{Ce}_{0.9}\text{O}_{2-\delta}$  composite electrode was fabricated by combustion chemical vapor deposition [20]. The structure is not well defined, but high surface area electrode with low electrode resistance is achieved by deposition parameter optimization.

Furthermore, by utilizing columnar growth mode in pulsed laser deposition, it is possible to have a porous thin film electrode with structure well defined enough to establish surface area-column height relationship. By comparing electrochemical resistances of different thickness (column height) electrodes, hydrogen electrooxidation kinetics on Sm-doped ceria electrode is proven to be ceria-gas interface reaction limited up to 10.8 micrometer thickness [21].

From previous studies [21, 24], it is clear that Sm-doped ceria has high hydrogen electrooxidation activity (higher than platinum and nickel), and the overall kinetics is limited by ceria-gas interface reaction. However, “surface” reaction can be broken down further, and the ultimate rate determining step in this surface reaction should be elucidated. Since there are two gas species involved (reactant  $H_2$  and product  $H_2O$  as seen in Eq. (1.8)), it is a natural approach to vary the content of these two gases independently.



Surprisingly, this is rarely done in literature. Only three papers [42, 43, and 44] report systematic, independent control of the two gases for model anodes (pattern electrodes), and they were performed on Ni pattern on YSZ single crystalline electrolyte. There is no systematic gas composition variation study reported on Sm-doped ceria electrode which becomes increasingly important because of its high electrochemical activity and compatibility with ceria-based electrolyte. This is the motivation for this work (chapter 4). Using symmetric cell geometry, we map out the electrode resistance dependence on each gas as a first step to understand surface reaction that governs overall hydrogen electrooxidation kinetics. Especially, we look into the effect of Sm doping level

and growth conditions on electrode resistance. The absolute magnitude of the resistance and gas dependence are of interest.

In an operating fuel cell, there is net current flowing through anode, electrolyte, and cathode. Therefore, it is necessary to understand the electrochemistry under biased condition which mimics the real fuel cell operational situation. The best experimental setup is known to be an asymmetric cell with reference-less geometry [45], and we adopt this geometry to study hydrogen electrooxidation with net current present. We try to compare different metals in this experimental setup to see if choice of metal has any impact on electrode kinetics.

#### 1.4.3 *Optical characterization*

Recently, a ceria-based thermochemical water splitting cycle is proposed and shown to be practical [46]. In this thermochemical scheme, ceria catalyst is exposed to solar radiation to be heated. This necessitates studying light-matter interaction for ceria. The fundamental materials property that governs this phenomenon is the refractive index. There are many reports for ceria refractive index in literature [47-52]. However, one should remember that effective refractive index changes when a material's mass density deviates from its theoretical, full density. Thus, it is needed to have the reference refractive index for fully dense case and a framework to deal with porosity. Either single crystal or epitaxially grown thin films can provide the reference refractive index. Here, we turn to epitaxially grown thin films for reference data derivation since we recognize that this study will give us an opportunity to develop a methodology to estimate thin film porosity. From refractive index measurement, it is possible to estimate mass density (porosity) through effective

medium theory (Appendix C) which relates effective refractive index of a composite to individual component's refractive indices. The optical dispersion behavior of undoped and 20 mol% Sm-doped ceria thin films, both dense and porous, were evaluated by UV-Vis optical transmission measurements. Reliable reference refractive index data are obtained for films with full density. Reliable determination on film thickness, porosity and roughness were made for films with thickness ranging from 500 to 2500nm. Physically meaningful microstructural parameters can also be extracted even for ultrathin films (<20nm thick). The developed methodology should be applicable to arbitrary substrate-film combinations since we tested the method for cases where substrate refractive index is higher than film's refractive index or lower than film's refractive index.

## Chapter 2

# Film fabrication

### 2.1 Introduction

#### 2.1.1 Chemical vapor deposition of ceria films for fuel cell application

Ceria MOCVD film has also been grown in a context of SOFC. Combustion CVD is used to fabricate porous nanostructure to enhance the surface area of the electrode [20].  $\text{Sm}_{0.5}\text{Sr}_{0.5}\text{CoO}_{3-\delta}$ - $\text{Sm}_{0.1}\text{Ce}_{0.9}\text{O}_{2-\delta}$  composite cathode is co-deposited on YSZ or GDC dense polycrystalline substrate. Deposition temperature effect on microstructure and area specific resistance of this composite has been studied. For electrolyte application, only electrochemical vapor deposition (EVD, a variation of chemical vapor deposition) seems to be able to produce dense enough ceria film on top of the porous polycrystalline substrate (Fig. 2.1). This technique is not widely spread due to additional complexity in the setup (Fig. 2.2). There is no OCV reported yet for a dense ceria electrolyte from EVD process.

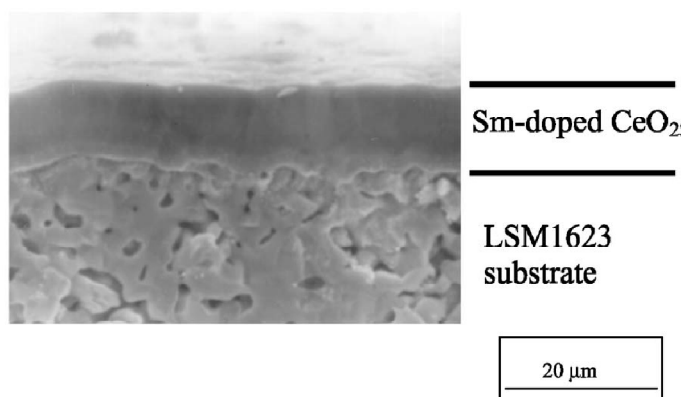


Figure 2.1 Cross-sectional SEM image of a dense film of Sm-doped ceria deposited using EVD on  $\text{La}_{0.81}\text{Sr}_{0.19}\text{MnO}_{3-\delta}$  porous cathode [53].

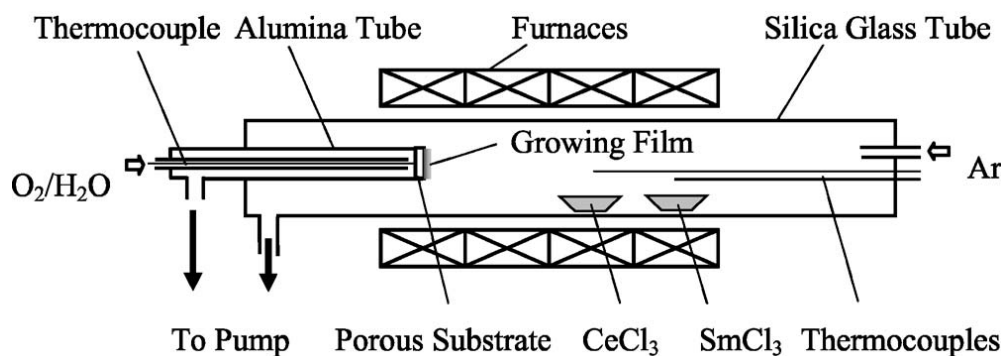


Figure 2.2 An electrochemical vapor deposition setup designed for Sm-doped ceria film growth [53]. It is made of two chambers. Oxygen source and metal source are separately supplied.

### 2.1.2 Precursors

Choice of precursors is important since growth behavior varies depending on what precursor is involved. In the literature,  $Ce(tmhd)_4$  is the most common precursor which has been used for chemical vapor deposition and atomic layer deposition (tmhd = 2,2,6,6-tetramethyl-3,5-heptanedionato. Sometimes, it is called dpm). It has 8 oxygen atoms in the molecular formula, and does not have fluorine. Also, it is water insoluble and nontoxic. Precursors with this ligand have been used for YBCO deposition [54] and PBT ( $Pb_xBa_{1-x}TiO_3$ ) deposition [55]. Unfortunately, this precursor is in solid form with continuously changing surface area under evaporation condition, making the evaporation rate unstable during deposition runs. To minimize this problem, solid precursors have been coated on the surface of steel balls [54]. For Sm source,  $Sm(tmhd)_3$  is chosen to have the same ligand as Ce source. This choice is arbitrary; there is no necessity to go with  $Sm(tmhd)_3$ . However, its evaporation behavior is already reported in a literature along with  $Ce(tmhd)_4$  giving us a good starting point.  $Sm(tmhd)_3$  is also in solid form, and coated on steel balls.

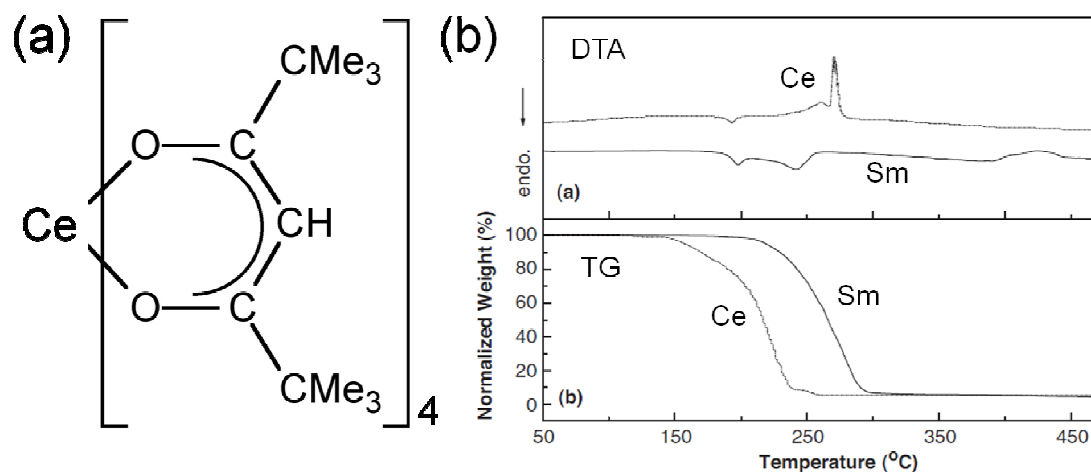


Figure 2.3 Precursor structure and thermal behavior. (a) Structure of  $\text{Ce}(\text{tmhd})_4$  molecule. (b) Differential thermal analysis curve and thermogravimetry curve for metal sources [56].

From Fig. 2.3 (b), one can see that Ce source evaporates at lower temperature than Sm source does. In addition, Ce source shows clear exothermic decomposition peak ( $\sim 270^\circ\text{C}$ ) while Sm source shows broad endothermic peaks representing partial decomposition, and broad exothermic peak above  $400^\circ\text{C}$  for complete decomposition/oxidation.

### 2.1.3 Doping

A specially designed device with a moving cartridge [57] has been employed for flash evaporation of a mixture of solid precursor of  $\text{Ce}(\text{tmhd})_4$  and  $\text{Y}(\text{tmhd})_3$ . Since  $\text{Ce}(\text{tmhd})_4$  and  $\text{Y}(\text{tmhd})_3$  share similar thermal and volatile property, the cation ratio in deposited film was close to the initial cation ratio in the solid precursor mixture [58]. In aerosol-assisted MOCVD or direct liquid injection MOCVD, it is common practice to dissolve many components in a common solvent to form multi-component compounds or solid solutions. This is often called “cocktail” precursor, and it has been proven successful

for YBCO deposition [59] and PZT ( $\text{PbZr}_x\text{Ti}_{1-x}\text{O}_3$ ) deposition [60]. Sm-doped ceria has been already grown in this way. Due to the difference in thermal decomposition kinetics of the two precursors (Ce and Sm sources), it was found that resultant Sm doping level depends on deposition temperature even when the precursor molar mixing ratio is fixed for all temperatures [61].

#### 2.1.4 Preferred orientation

Preferred orientation of a thin film depends on many factors. Even the tilt angles of the substrate with respect to precursor stream and substrate distances from the nozzle have effects on preferred orientation of ceria film [62] (Fig 2.4).

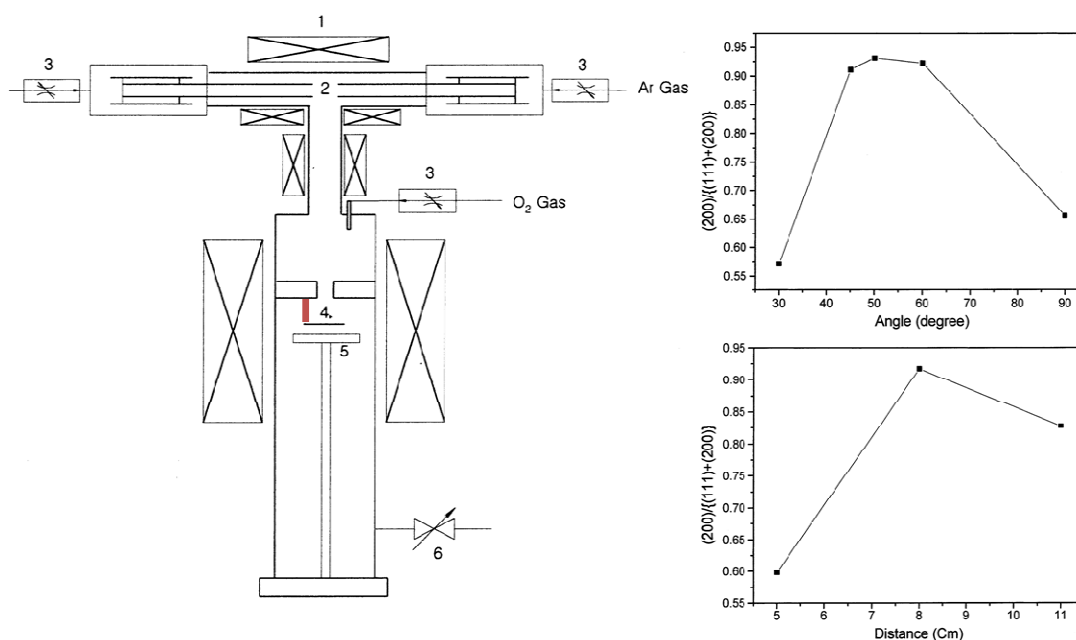


Figure 2.4 Schematic view of an MOCVD setup reported in literature. 1: Heater, 2: source material, 3: MFC, 4: substrate, 5: substrate support, 6: pump. Nozzle to substrate distance is marked as a red vertical bar. Substrate tilting angle and distance from the nozzle affect final film preferred orientation. In all cases, the substrate is Ni foil [62].



This clearly demonstrates the complexity in the MOCVD process that determines preferred orientation. Furthermore, with all other parameters fixed, change of precursors also affects preferred orientation of ceria films as shown in Fig 2.7 [63].

Table 2.1 lists factors that can affect structure evolution (hence, preferred orientation) in polycrystalline films.

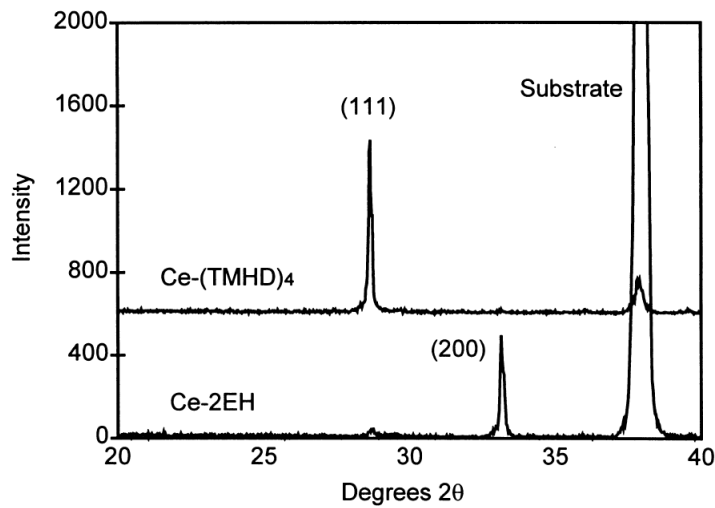


Figure 2.5 Precursor effect on preferred orientation.  $\text{Ce}(\text{tmhd})_4$ : Ce(IV) tetramethylheptanedionate.  $\text{Ce}-2\text{EH}$ : Ce(III) 2-ethylhexanoate. In all cases, the substrate is sapphire (11 $\bar{2}$ 0). Deposition was done by combustion CVD [63].

Table 2.1 Governing factors for thin film structure evolution

Kinetic factors	Process parameters
<ul style="list-style-type: none"> <li>- Adatom diffusivities on the substrates surface</li> <li>- Adatom self-diffusivities on island surfaces</li> <li>- Self-diffusivities in grain boundaries</li> <li>- Grain boundary mobilities</li> <li>- Adatom cluster nucleation rates</li> <li>- Adatom desorption rates</li> </ul>	<ul style="list-style-type: none"> <li>- Substrate temperature (affects all kinetic processes)</li> <li>- Deposition pressure (affects energies of arriving adatoms)</li> <li>- precursor push flow rate (affects energies of arriving adatoms)</li> </ul>

## 2.2 Fabrication details

### 2.2.1 CVD reactor setup

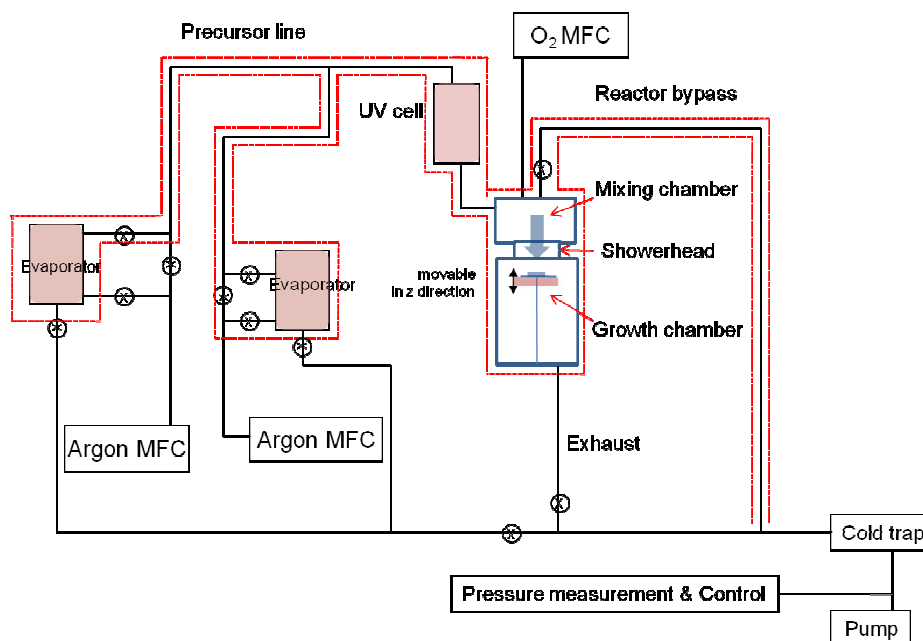


Figure 2.6 Experimental setup of the homemade MOCVD reactor. Red dotted line denotes heated part of the system.

Fig. 2.6 describes the setup for MOCVD reactor used in this work. It is a cold wall vertical reactor. The substrate heater has a circular hot surface measuring 2 inches in diameter. Maximum temperature for this substrate heater is 950°C. The precursor flow is from the top down onto the surface of substrates, MgO(100) and/or YSZ(100). This setup has a disadvantage that precursor flow can be disturbed by buoyancy and precursor molecules can be prematurely heated before reaching substrate surface. However, it is simpler to implement than inverted setup where precursor molecules come from the bottom. All heated hardware parts of the system are wound up by heating ropes. Heating ropes and the substrate heater are operated separately. 7 different temperature set points are

specified; Ce source evaporator (190°C), Sm source evaporator (130°C), precursor line (215°C), UV cell (250°C), reactor bypass line, mixing chamber (240°C), and substrate heater (400~700°C). UV cell becomes useful in long depositions for checking if the precursor is running out. Initially, we wanted to correlate the film Sm doping level to the UV absorption peak ratio of the two precursor vapors. However, they show severe overlap making this attempt futile. The evaporator is heated by a homemade heater made of heating ropes and aluminum foil. All the heating ropes are covered by aluminum foil to suppress accidental Si impurity incorporation.

Fig. 2.7 shows the evaporator design. The top lid with gas inlet and outlet is fixed to the whole MOCVD system. Only the bottom canister part is removed and attached between each run for a refill. For an one-hour long deposition, 0.25grams of  $\text{Ce}(\text{tmhd})_4$  is added and re-coated on the surface of steel balls just before each run.  $\text{Sm}(\text{tmhd})_3$  is much slowly consumed, so it is less frequently refilled but re-coated anyway between each run to keep evaporation conditions as same as possible.

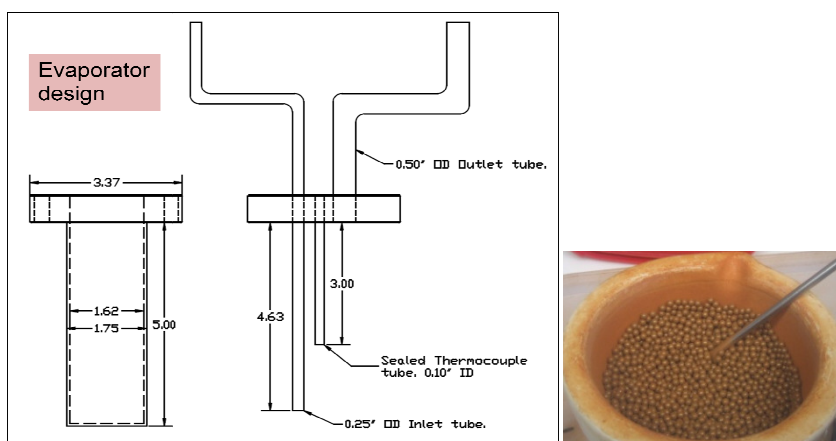


Figure 2.7 Precursor evaporator design. Temperature is measured a K-type thermocouple inserted in the thermocouple tube. This tube is in physical contact with steel balls contained in the precursor canister. Supposedly, only argon gas is in contact with solid precursor surface with copper gasket in place. Ce precursor coated steel balls are also shown.

### 2.2.2 CVD procedure

For a deposition run, following steps were taken.

1. Fill up precursor canisters. Place substrates on the substrate holder.
2. Fasten up all the joints. Draw vacuum down to background pressure ( $\sim 0.02$  Torr) for all parts.
3. Seal off evaporators at the background pressure to prevent precursors' exposure to oxygen. Flow argon and oxygen to reach deposition pressure ( $1\sim 10$  Torr) through evaporator bypass and reactor bypass.
4. Heat up all parts marked in Fig. 2.8.
5. After temperature stabilization at respective set points, open up the evaporator valve and flow argon through evaporators. At this stage, the precursors are pushed into the mixing chamber, but exit through reactor bypass without hitting the substrate surface.
6. Wait until pressure/temperature fluctuation dies out (2~3 minutes).
7. Re-route the precursor flow by closing reactor bypass and opening reactor exhaust. Deposition starts.
8. Monitor process parameters during deposition.
9. After deposition, close the evaporator valve and flow argon through evaporator bypass.
10. Re-route argon/oxygen flow back to reactor bypass.
11. Cool down all parts.
12. Open up reactor to pull out substrates. Open up evaporator to refill/re-coat precursor

### 2.2.3 Deposition process parameters

Table 2.2 summarizes process parameters explored. The reported growth temperature is 100°C lower than the substrate set temperature. This discrepancy is measured in a dummy run where no deposition has occurred. The evaporation temperature for Ce precursor is determined by consulting literature thermogravimetry curves [56, 63]. Sm source evaporation temperature is set to be lower than Ce source evaporation since it is not the main component of the film. If possible, it is better to keep evaporation temperature low to prevent wasteful consumption and thermal degradation of the precursor. At 130°C, Sm precursor shows only sign of sublimation without any sign of melting.

Table 2.2 Film growth parameters for doped/undoped ceria film deposition

Growth temperature (/°C)	400~650
Growth pressure (/Torr)	1~10
Growth time (/min)	0~270
Gas flow (/sccm)	Argon (Sm push flow + Ce push flow):100, O <sub>2</sub> :50
Ce precursor evaporation temperature (/°C)	190
Sm precursor evaporation temperature (/°C)	130

### 2.2.4 Film morphology

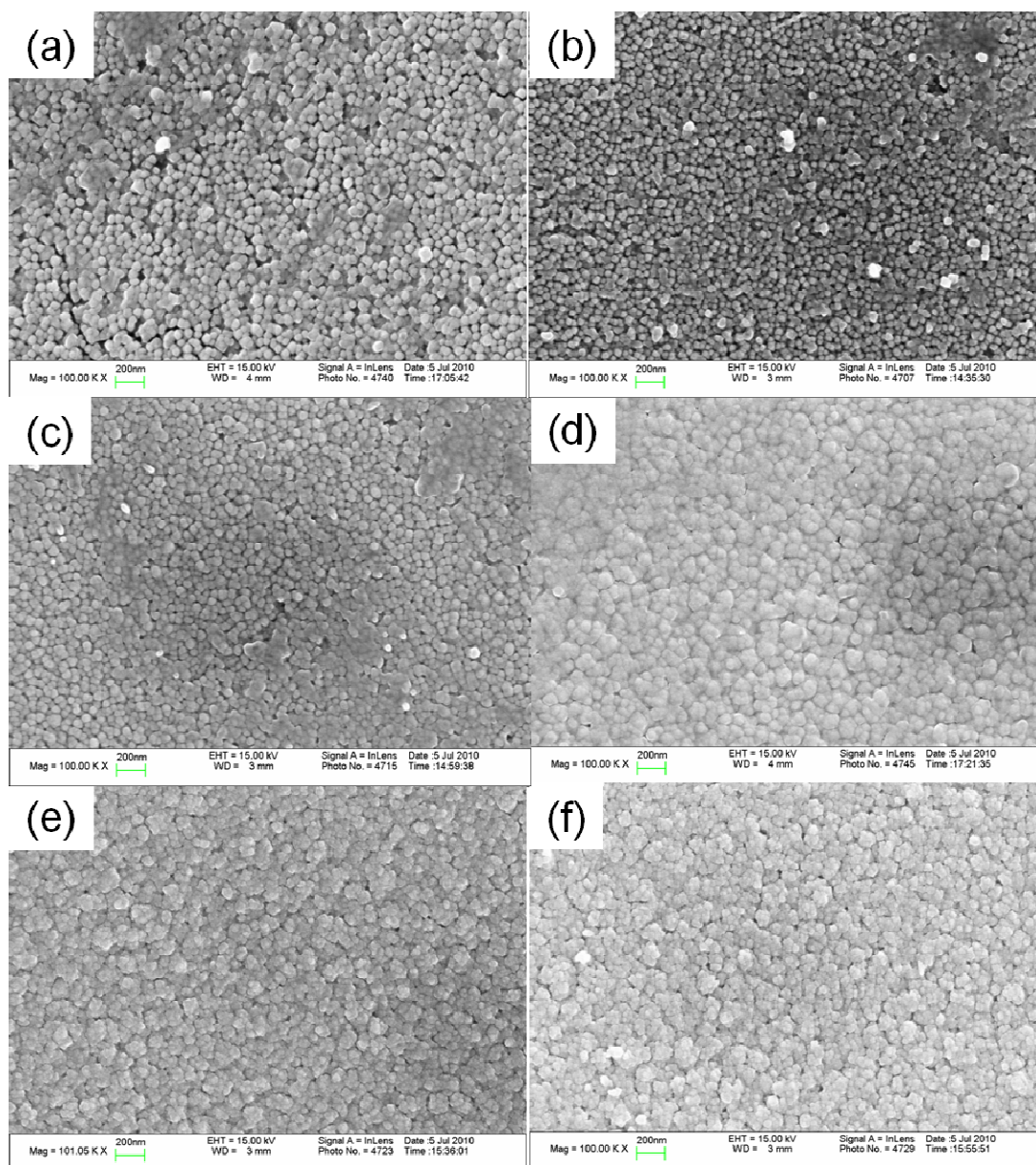


Figure 2.8 Scanning electron microscopy images of  $\text{CeO}_2$  grown by MOCVD on YSZ (100) single crystals at various growth temperatures: (a) 400°C, (b) 450°C, (c) 500°C, (d) 550°C, (e) 600°C, (f) 650°C. Deposition pressure: 3Torr

Fig. 2.8 shows top-down view of undoped ceria films grown at different temperatures. They all show columnar growth in this temperature window.

### 2.2.5 Doping level control

Only Sm doping is tried in this work. As seen in Fig. 2.6, we have two different evaporators for two separate sources set for two different evaporation temperatures. In principle, one can think of two different ways to control doping level; changing evaporation temperature or changing argon push flow rate. We chose to change the argon push flow rate since precursor vapor pressure is very strong function of temperature so that precise control is not easy. When we try to put two precursors in one evaporator kept at 190°C, the rate of consumption is different for the two metal sources leading to Sm dopant concentration gradient along the direction of growth (Fig. 2.9). By using two evaporators separately, it is possible to maintain or manipulate the doping profile at will (Fig. 2.10). For these two figures, depth profiling is done by secondary ion mass spectroscopy facility at UC Santa Barbara (Physical Electronics 6650) using oxygen ion beam to etch away film materials. Individual atomic weights for atomic species are shown in the legend. This type of in situ doping level manipulation is not straightforward for physical vapor deposition methods that use one target of fixed stoichiometry.

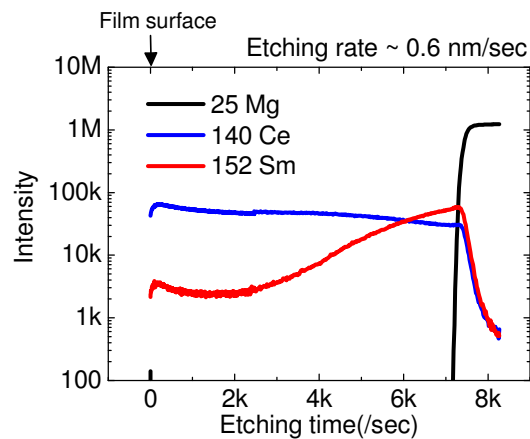


Figure 2.9 Secondary ion mass spectroscopy depth profile for a film with nonuniform dopant concentration along film thickness.

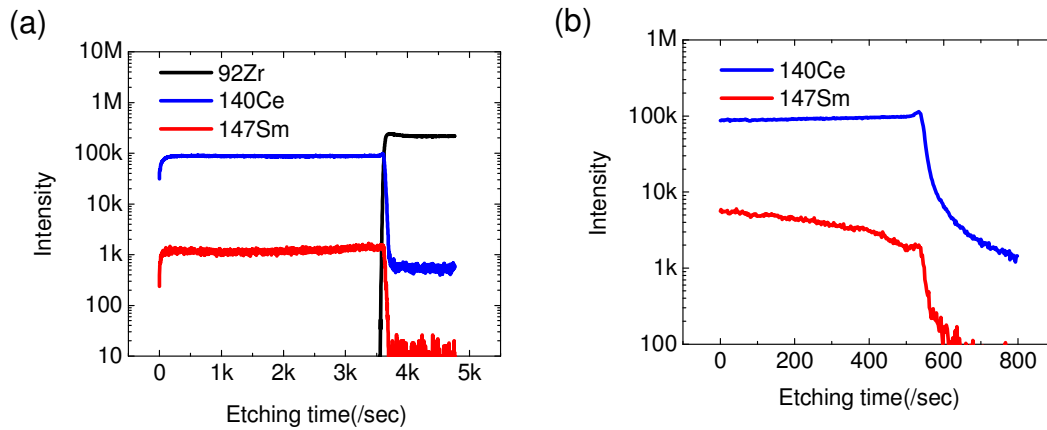


Figure 2.10 Secondary ion mass spectroscopy depth profiles for films with in situ dopant level control. (a) Fixed argon push flow rates for Ce source and Sm source during deposition. (b) Increasing argon push flow rate for Sm source while holding the total argon flow rate at 100sccm.

### 2.2.6 Preferred orientation control

Deposition pressure was the process parameter that we varied to get different preferred orientations. It is not a focus of this work to elucidate the growth mechanism behind this phenomenon. Still, we propose a hypothesis that can explain this behavior. At lower deposition pressure, the mean free path of incoming precursor molecules becomes longer since mean free path is inversely proportional to total pressure [64]. This means that a precursor molecule can avoid collisions between gas molecules while travelling to the substrate surface. With less frequent collision per gas molecule, the homogeneous gas phase nucleation of ceria particles is suppressed. Thus, at low pressure, heterogeneous nucleation and growth at the substrate surface occurs as usually expected for thin film growth, and strain energy minimization drives overall texturing behavior for films with enough thickness so that one can neglect surface/interface energy contribution [65]. With higher deposition pressure, precursor molecules have to bounce around before reaching substrate surface due to short mean free path. This will increase the probability for



homogeneous nucleation of ceria particles, and subsequent agglomeration is possible [56]. When these particles eventually land on substrate surface to get incorporated, their surface mobility is lower than adatom/admolecules' surface mobility due to much larger mass. They cannot quickly take the lowest energy position before the next layer deposition. Thus, at high deposition pressure, it is hard to achieve strain energy minimization as well as surface/interface energy minimization. This explains better alignment (stronger 100 peak relative intensity) with lower deposition pressure though strain energy minimization. In Fig. 2.11, we show the effect of the deposition pressure on undoped ceria films on YSZ (100) and MgO (100) substrates.

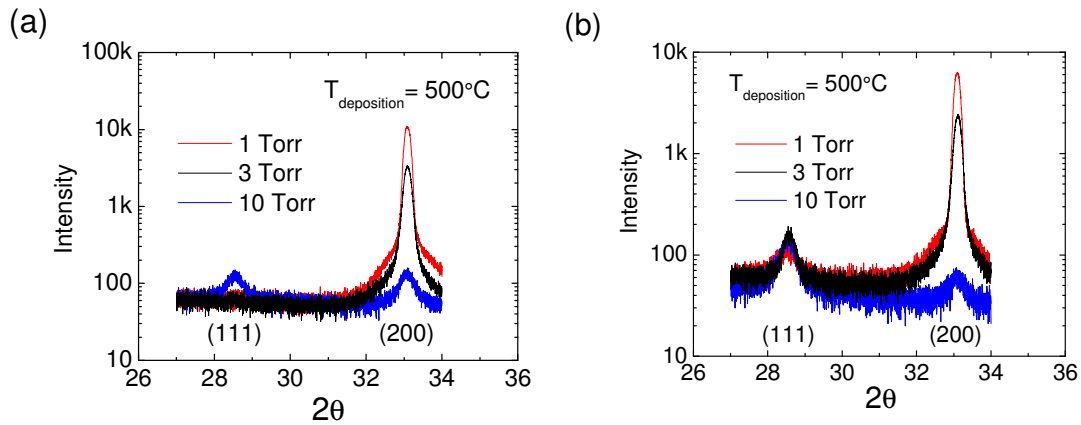


Figure 2.11  $\theta$ - $2\theta$  scans for (a) films grown on YSZ (100) and (b) films grown on MgO (100). One YSZ and one MgO substrates were grown together for each run (three different pressure runs).

### 2.2.7 Influence of substrates

Introduction to rocking curves can be found in Appendix D.

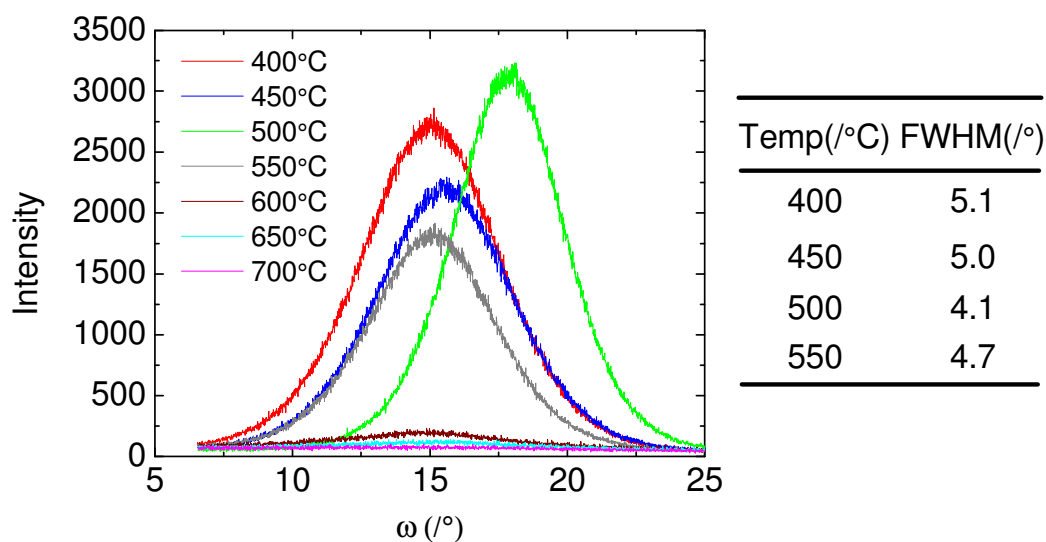


Figure 2.12 X-ray rocking curves for undoped ceria films grown at various temperatures on MgO(100) substrate. Omega scans were performed about (200) diffraction peak. Deposition pressure: 3Torr.

Fig. 2.12 shows the change in rocking curves depending on the growth temperature of the undoped ceria films grown on MgO (100) for 30 minutes. The symmetric axes for all traces would fall on top of one another if X-ray optics alignment were perfect for all measurements. For temperatures  $\geq 600^\circ\text{C}$ , the intensity is weak indicating broad in-plane spread of the out-of-plane texturing. FWHM(full width at half maximum) values are listed for 4 different temperatures.

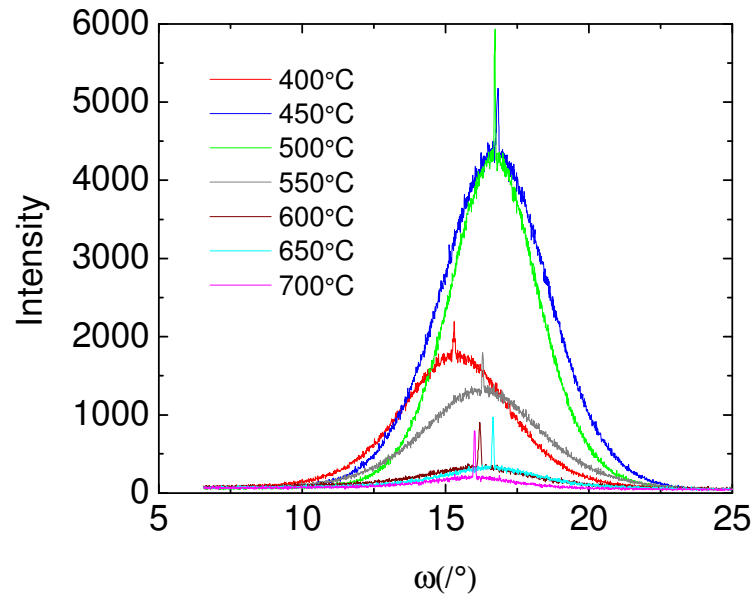


Figure 2.13 X-ray rocking curves for undoped ceria films grown at various temperatures on YSZ(100) substrate. Omega scans were performed about (200) diffraction peak. Deposition pressure: 3Torr.

Fig. 2.13 shows the change in rocking curves depending on the growth temperature of the undoped ceria films grown on YSZ (100). For temperatures  $\geq 600^\circ\text{C}$ , the intensity is weak as in the case of MgO (100) substrate. However, there is a noticeable difference compared with MgO. All omega scan have a sharp tip at the center. This comes from alignment of the film at the initial stages of deposition as a result of better lattice match between ceria and YSZ (6% rather than 28%) rendering epitaxial relationship YSZ (100). This sharp tip has been observed in literature as well [66, 67, and 68] for substrates with reasonable lattice match.

## Chapter 3

# Electrical characterization

### 3.1 Summary

In this chapter, electrical conductivity measurement results of the MOCVD grown undoped ceria films are described. All data presented here are from AC impedance measurement along the film growth direction. This through-plane conductivity measurement is much less frequently reported compared to in-plane conductivity due to experimental difficulties; for example, easy short-circuit formation between the two terminal electrodes physically separated by the films thickness. Bulk conductivity is measured varying temperature and surrounding water vapor pressure in oxygen environment. Water vapor pressure dependence of extracted physical quantities is analyzed.

The through-plane conductivity shows two distinct behaviors. At high temperature - low water vapor pressure conditions, oxygen ion conduction prevails as in the micro-grained bulk processed ceria. At low temperature – high water vapor conditions, proton conduction prevails as in nanograined bulk processed ceria. This behavior is expected given the columnar nature (hence, aligned open pores) of the film, and our measurements confirm this. There was some enhancement (factor of 4) of proton conductivity initially targeted from the experiment design. In addition, we made a new finding on the water vapor pressure dependence of proton conductivity indicating the proton conduction pathway: exposed grain surfaces and parallel grain boundaries.

### 3.2 Introduction

Acceptor doped ceria is a well known oxygen ion conductor that can function as an electrolyte in a solid oxide fuel cell in the intermediate temperature range [69]. In recent years it has been observed that, upon nanostructuring, ceria can display significant proton conductivity at much lower temperatures than required to activate oxide ion motion. The connection between grain size and magnitude of the proton conductivity in the nanostructured materials displaying this unusual phenomenon, as well as the observation that proton uptake and transport in bulk, microcrystalline ceria is negligible [70], has led to the general consensus that the proton conduction occurs through a grain boundary (or surface) mediated process [71, 72]. This insight suggests that a material with an aligned microstructure, with grain boundaries and/or open pore channels parallel to the path of proton transport, may lead to proton conductivities that are even larger than those reported to date. Accordingly, we have prepared in this work thin-film ceria with columnar grains and characterized the conductivity along the film growth direction. Beyond a modest enhancement in conductivity relative to bulk nanocrystalline ceria, the investigation sheds some new light on the proton transport mechanism.

### 3.3 Cell configuration & materials characterization

Undoped ceria films were grown by chemical vapor deposition (CVD) using an in-house constructed, cold-walled vertical reactor. Dopants are not utilized in order to avoid possible composition gradients in the as-grown films. To facilitate through-plane (or thickness mode) conductivity measurements, deposition was carried out on MgO(100) substrates (MTI crystals) first coated with Pt (~200 nm) by DC sputter deposition (AJA International ATC Orion system, Ar 3mTorr, 10 sccm, ambient temperature). The cerium precursor for CVD film growth was the commercially available compound  $\text{Ce}(\text{tmhd})_4$  (Strem CAS#: 18960-54-8, 99.9% cation purity). The as-received solid precursor was used without further purification and delivered to the reaction chamber following a procedure described elsewhere [54]. The deposition conditions are provided in full in Table 3.1. Top Pt electrodes were applied to the films so grown by DC sputtering (as above). It was observed that a minimum of 50 nm in Pt thickness was required to prevent film dewetting and enable reliable measurements. A shadow mask was used to limit electrode deposition to circular regions with nominal diameter of 1.5 to 3 mm. Doing so prevented short circuits from forming at the film edges, and also enabled, by application of multiple isolated top electrodes, multiple conductivity measurements from a single film. Schematic measurement configuration is given in Fig. 3.1.

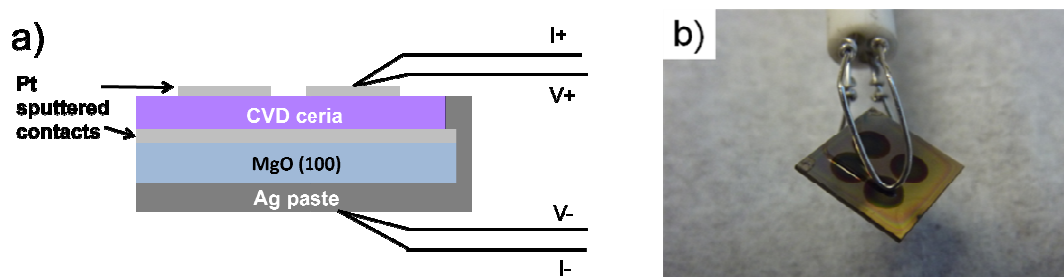


Figure 3.1 (a) Schematic view of thickness mode measurement sample. Ceria films were deposited on platinum coated MgO(100) substrate. Silver paste was painted around the substrate to make electrical contact. Typical thickness for bottom Pt electrode: 200nm, top Pt electrode: 50~250nm (b) A sample loaded on testing fixture. Per one MgO wafer (1cm by 1cm), there are 4 circular top electrodes. Samples were placed in a vertical tube furnace.

Scanning electron microscopy (SEM) and x-ray diffraction (XRD) measurements were performed on the as-deposited films using a Carl Zeiss LEO 1550VP and a Panalytical X'pert pro MRD system (45kV, 40mA), respectively. The grain size was estimated from the XRD peak breadth using the Scherrer equation [73] after accounting for instrumental peak broadening using an YSZ single crystal and data collected under identical conditions. The microstructural features and phase behavior were reproduced many times for many different films and only representative results are reported.

Table 3.1 Film growth conditions for chemical vapor deposition of undoped ceria

Growth temperature (/°C)	500
Growth pressure (/Torr)	3
Growth time (/min)	240~270
Gas flow (/sccm)	Argon:100, O <sub>2</sub> :50
Ce precursor evaporation temperature (/°C)	190

Film conductivity was measured by A.C. impedance spectroscopy (ACIS).

Samples of the configuration shown in Fig 3.1 were placed in a vertical tube furnace equipped with gas control. The gaseous environment was either (i) high-purity oxygen passed through a molecular sieve to remove residual water, or (ii) the same oxygen gas humidified to a specified level. In the latter case, the  $p_{\text{H}_2\text{O}}$  was set by saturating the incoming oxygen gas with water held at a specified temperature. This humidified stream was then either mixed with dry oxygen gas to reach an even lower water level or used directly without dilution. The quoted water partial pressures correspond to the expected values without further experimental confirmation. Measurements were carried out by first heating samples to the highest temperature examined (500°C) under the gaseous environment of interest. A 5hr dwell at this temperature allowed for stabilization of the electrical contacts and equilibration of the ceria film with the gas phase. Measurements were made at several different temperatures upon step-wise cooling from this equilibration condition. The ramp rate was  $\leq 2$  degrees per minute to minimize possible thermal shock, and the dwell time at each measurement condition  $\geq 30$  min. Measurements were limited to a maximum temperature of 500°C, equal to the film growth temperature, to preclude the possibility of evolution of the film microstructure over the course of the data collection. The stability of the Pt film top-electrodes was confirmed by post-measurement SEM imaging. Data were collected using a Solartron 1260 frequency response analyzer over the frequency range from 1MHz to 0.1Hz (24 points per decade) and voltage perturbation amplitude of 20mV with zero DC bias. Data analysis was performed using the ZView2 commercial software package (Version 2.9b, Scribner Associates, Inc.).



Electrical measurements were performed for several different films. However, the essential results are captured in the behaviors of two representative samples, the characteristics and experimental conditions for which are presented in Table 3.2. The transport data presented below are those acquired from these two films.

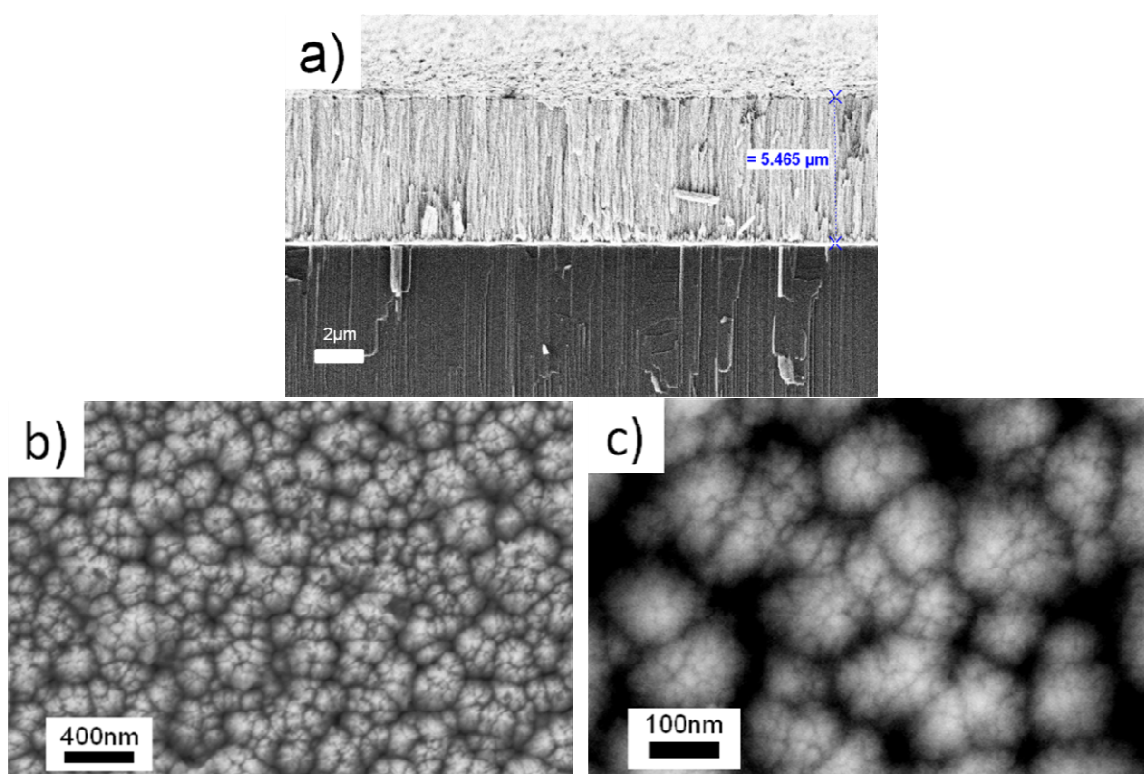


Figure 3.2 (a) Cross-sectional image of a representative ceria sample ( $5^\circ$  tilted). One can see fracture marks on MgO substrate (bottom dark region), and the columnar structure of the CVD ceria film. Bright boundary between ceria film and the MgO substrate is the 200nm thick platinum coating. This particular film was roughly  $5.5 \mu\text{m}$  thick. (b) A top view image from another representative film. (c) A higher magnification image of the columns (same film as in (b)). Contrast is adjusted to make grain boundaries visible sacrificing details of the depressed part of the surface. XRD pattern from this sample is shown in Fig 3.3.

Table 3.2. Physical characteristics of films used for electrochemical measurements

Film.	Top electrode	Thickness ( $\mu\text{m}$ )	Measurements
1	sputtered Pt (250nm thick)	3.6	pH <sub>2</sub> O isobars (dry, 1.27mbar, 8.37mbar)
2	sputtered Pt (50nm thick)	5.9	isotherms (250°C, 300°C, 350°C)

The SEM images, Fig. 3.2, reveal that the desired columnar microstructure has been obtained, with good adhesion of the ceria film to the 200 nm thick Pt bottom electrode. The diameter of the columns is not clearly defined, but can be roughly specified as  $\sim 100$  nm, based on the high contrast image presented in Figure 2c. Individual grains comprising the columns appear to be even smaller, with an in-plane grain size smaller than 40 nm. The X-ray diffraction results, Fig. 3.3, collected both before and after electrical characterization at 500°C, indicate that the films undergo negligible microstructural evolution over the course of the measurements. The data further reveal that despite growth on Pt, the film has a strong (100) preferred orientation. The ratio of the integrated intensities of the (200) and (111) peaks,  $\frac{I(200)}{I(111)}$  is about 32 in the film, many times greater than the expected value for polycrystalline ceria with random crystallite orientation,  $\sim 0.3$ . The out-of-the-plane grain size, based on the breadth of the (200) peak, is calculated to be 33 nm.

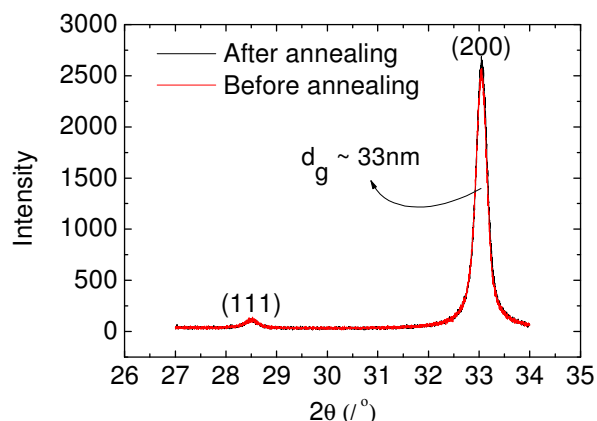


Figure 3.3  $\theta$ - $2\theta$  X-ray scan from 4.3 $\mu$ m thick ceria film grown on Pt coated MgO(100) substrate. Grain size ( $d_g$ ) is calculated from FWHM of the 200 peak by Scherrer formula. Instrument broadening was estimated at 0.015° using a blank YSZ single crystal substrate (step size 0.001°, Gaussian fitting). There was no change in X-ray pattern before and after annealing which matches the thermal history of all the examined films.

### 3.4 Electrical characterization

Selected Nyquist plots ( $Z_{\text{real}}$  vs.  $Z_{\text{imag}}$  as parametric functions of frequency) are presented in Fig. 3.4 for a film exposed to three different gas atmospheres at a fixed temperature of 200 °C. The spectra are qualitatively similar. All three display one high-frequency arc that extends to the origin and a low-frequency response that, at the lowest frequencies (not shown), turns towards the real axis. The latter feature, which was found to vary in response to variations in total gas flow rate, is attributed to the electrode behavior and is not considered further. With respect to the high-frequency response, in a polycrystalline ionic conductor the impedance spectra typically display, in contrast to the present results, distinct bulk and grain boundary arcs [66]. On the other hand, it is not uncommon in the case of nanocrystalline ceria to observe a single, non-electrode response [39, 74-76], as appears to be the case here. Grain boundary resistance in impurity-free ceria

is due to the ion-blocking effect of space charge zones at the grain interfaces. Because the width of the space charge zone is inversely proportional to dopant concentration, the zone can extend in nominally undoped ceria over a distance of tens of nanometers [77]. If the material is additionally nanostructured, the space charge zone can encompass the entire grain such that there is no distinction between bulk and grain boundary regions. Thus, the absence of a distinct grain boundary response in the present measurements is not inconsistent with the presence of grain boundaries normal to the direction of charge transport. The raw impedance data furthermore show that the overall resistance decreases dramatically with increasing water partial pressure.

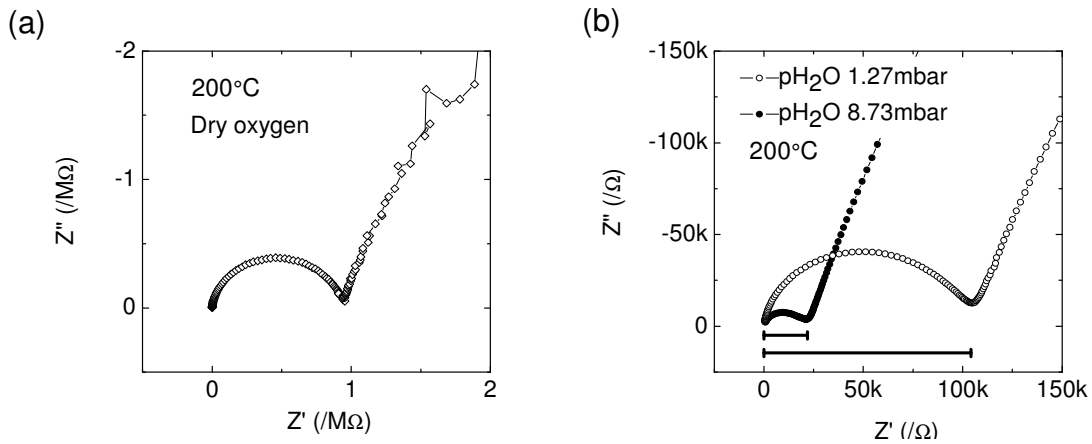


Figure 3.4 Impedance arcs at fixed temperature with different water vapor pressure. (a) Dry oxygen. (b) Two different water levels (1.27 and 8.73 mbar). For conductivity calculation,  $Z'$  resistance is simply taken from  $-Z''$  minimum point as shown by horizontal bars. The length of this bar is defined as  $R_M$ .

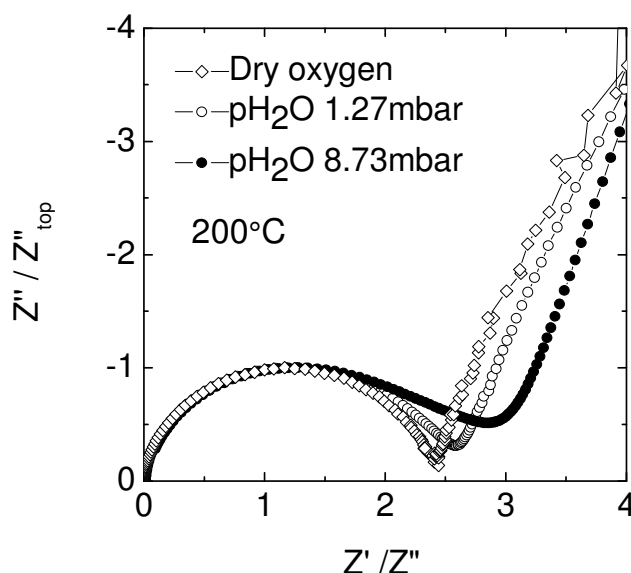


Figure 3.5 Normalized representation of impedance spectra of Fig. 3.4 accentuating changes in the shape of the impedance arcs in response to changes in atmosphere. Normalization is with respect to maximum value of imaginary component of impedance within the bulk response regime.

The general shapes of the spectra suggest, at first glance, that the high frequency data are amenable to equivalent circuit modeling in terms of a single RQ subcircuit. Closer examination, however, reveals a change in the shape of the high frequency arc in response to changes in gas atmosphere, suggesting the inadequacy of a simple RQ to extract frequency independent properties. This behavior is underscored in Fig. 3.5 in which the three spectra of Fig. 3.4 are superimposed after normalization with respect to the magnitude of the imaginary component of the impedance at the characteristic frequency (*i.e.*, at the top of the arc). With increasing water partial pressure there is evidence of the emergence of an intermediate frequency feature that cannot be readily captured by simple equivalent circuit modeling. Thus, in order to avoid artifacts due to fitting according to an inappropriate equivalent circuit, the overall material resistance,  $R_M$ , was defined as the value of the real

impedance at the minimum in the imaginary impedance (as shown for example in Figure 4b). The equivalent ‘overall capacitance’ is defined for completeness as  $C_M = 1/R_M\omega_0$ , where  $\omega_0$  is the frequency at which the imaginary component of the impedance attains a maximum. The conductivity and relative dielectric constant are obtained by the usual transformation using film thickness and electrode area.

The capacitive and transport characteristics for the film are summarized in Fig. 3.6, with the relative dielectric constant presented in Fig. 3.6a and the conductivity in Fig. 3.6b. Whereas the dielectric constant is almost constant over the  $T$  and  $p\text{H}_2\text{O}$  range of the measurements, the conductivity varies by orders of magnitude. Furthermore, the relative dielectric constant is similar to the bulk value as reported for dense, nearly single-crystalline ceria [78]. The slightly lower value measured here is attributed to the obvious porosity of the films, Fig. 3.2. If the difference is attributed solely to such effects, the measured  $\epsilon$  values imply a reasonable porosity of approximately 30% in the CVD grown film. Porous ceria films grown by pulsed laser deposition and with similar microstructural features [21] have been found to display comparable levels of porosity. Rather significantly, the results in Fig. 3.6 show that the dielectric constant (being largely independent of the measurement conditions) is uncorrelated to the observed changes in the shape of the impedance spectra.

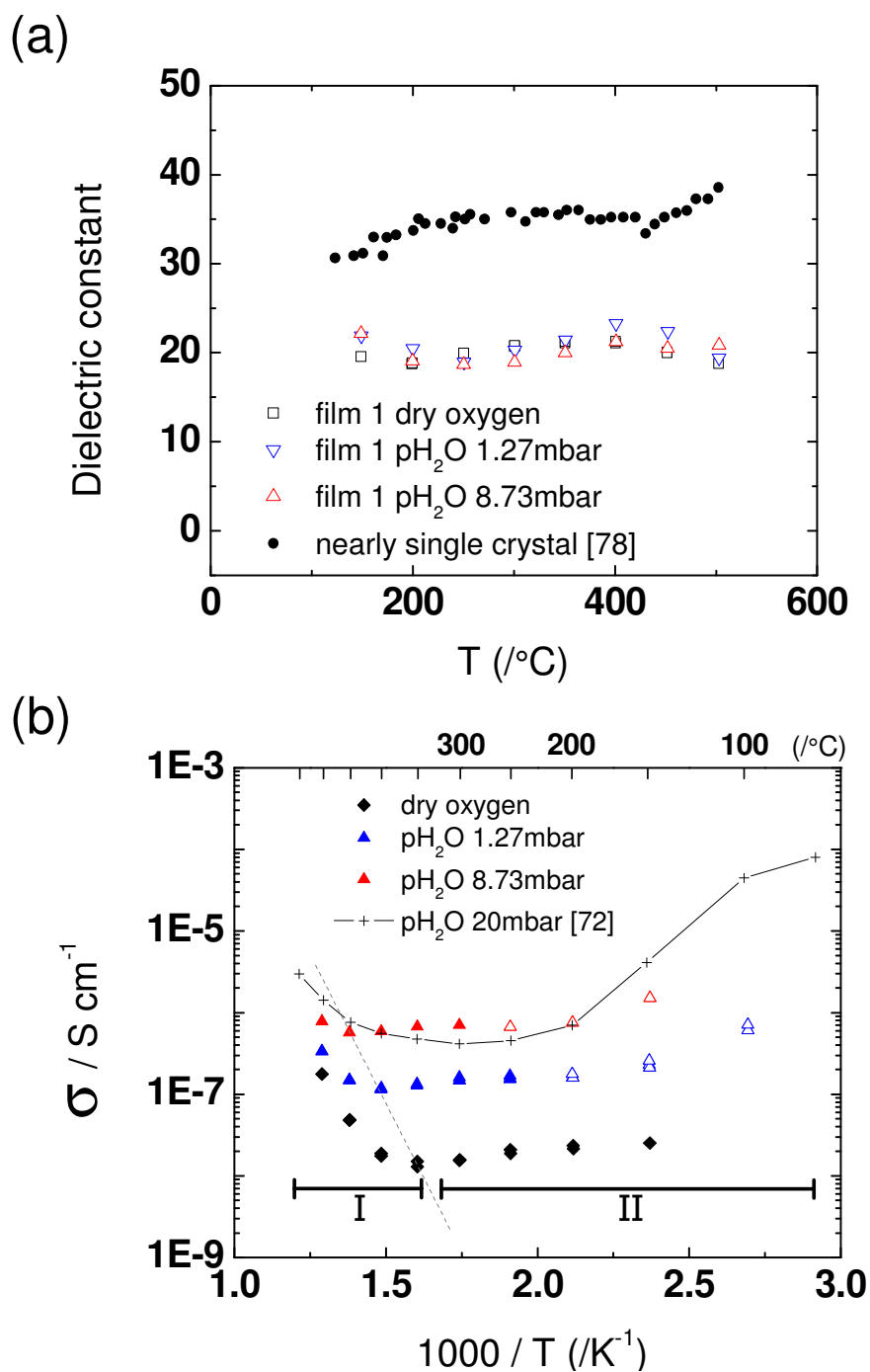


Figure 3.6 Effective DC properties of film 1: (a) dielectric constant, and (b) conductivity. Fully dense ceria dielectric constant is from literature performed under dry oxygen. Two regions are evident in the conductivity behavior. Region I: oxygen ion conduction is prevalent. Region II: proton conduction is prevalent. For comparison, proton conductivity reported for nanograined undoped ceria ( $\text{pH}_2\text{O} = 20$  mbar) is shown [72].

Turning to the results of Fig. 3.6b, the overall dependence of the conductivity on temperature, first decreasing then increasing with increasing temperature, with an inflection point at  $\sim 400^\circ\text{C}$ , and on  $p\text{H}_2\text{O}$ , is consistent with the identification of protons as the dominant mobile species at low temperature and is in good agreement with typical behavior reported in the literature [72]. Remarkably, the non-monotonic dependence of conductivity on temperature holds true even under nominally dry oxygen, at which proton sorption onto or incorporation into the oxide must be extremely limited. At higher temperatures oxygen ion conduction presumably dominates the transport process, as indicated by the observation of increasing conductivity with increasing temperature and a decreasing impact of water partial pressure. Moreover, with decreasing  $p\text{H}_2\text{O}$  the inflection point in the conductivity as a function of temperature shifts to lower temperature, indicating that the temperature regime for oxygen ion conduction expands with decreasing chemical potential of water.

Ignoring for the moment the subtle change in the shape of the impedance response, the material can be roughly represented by an equivalent circuit comprised simply by a capacitor and resistor in parallel. Given what is known about nanocrystalline ceria, we interpret the resistive element to correspond to proton migration along the surface of the parallel grain boundaries and/or open surfaces, and the dielectric element to the bulk. The unchanging dielectric response suggests that although the magnitude of the resistance changes dramatically and even the shape of the impedance response changes, the nature of the pathway is unchanged in response to changes in  $T$  and  $p\text{H}_2\text{O}$ .



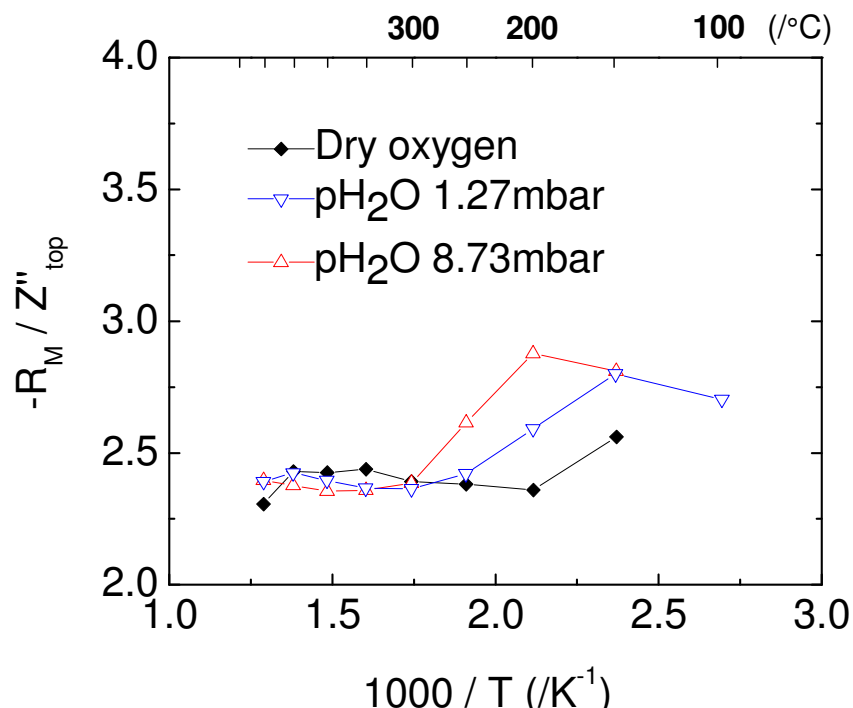


Figure 3.7 The quantity  $-R_M/Z''_{top}$  provides a measure of the non-ideality of the impedance arc and reflects the breadth of the distribution of relaxation times. A value of 2 indicates an ideal, semi-circular impedance arc whereas larger values indicate an oblate shape. For all conditions at  $T \geq 300^\circ\text{C}$ , the arc remains relatively ideal. For  $T < 300^\circ\text{C}$ , arc shape changes depending on the surrounding gas-phase water vapor pressure.

The change in arc shape is reflected in the ratio of the arc diameter,  $R_M$ , to its height,  $-Z''_{top}$  (the value of the imaginary component impedance at the peak of the arc). This quantity attains a value of 2 for a perfect RC circuit and has magnitude greater than that when the arc is depressed due to the presence of a distribution of time constants [79] and/or is composed of multiple overlapping arcs. A plot of this ratio as a function of  $T$  and  $p\text{H}_2\text{O}$ , Fig. 3.7, shows that the deviation from 2 is greatest at intermediate temperatures with a peak value (approaching 3) that occurs at a temperature that shifts upwards with increasing water vapor pressure. These conditions roughly correspond to the conditions at which proton conductivity adopts an intermediate value – not the very high conductivity of low

temperatures, but not the small proton conductivity at high temperatures at which oxide ion conduction begins to dominate the transport. Accordingly, we attribute the change in impedance features to the existence of a distribution of time constants under conditions of intermediate proton surface concentration. Such conditions can plausibly lead to a distribution of proton environments.

A summary of the water partial pressure dependence of resistivity, as measured from both Films 1 and 2, is presented in Fig 3.8. The two samples display comparable resistivities for a given set of conditions, with slightly higher conductivity in Film 1. The capacitance responses of the two films are also comparable (not shown). Film 2 has a slightly reduced volumetric capacitance, by  $\sim 5\%$ , behavior attributed to slightly higher porosity. Differences in surface microstructure may explain the slight differences in resistivity. Under the conditions of these measurements the overall conductivity is large, and the ratio  $-R_M/Z''_{top}$  for Film 2 ranged from 2.38 to 2.47 (comparable to the smallest values reported in Fig 3.7), indicating a relatively ideal, single arc in the impedance response and. The generally unchanging and almost ideal value of  $-R_M/Z''_{top}$  legitimizes a comparison of the resistivity as a function of purely environmental conditions and enabled impedance analysis by conventional equivalent circuit fitting. Significantly, the conductivity measured for Film 2 at 18 mbar  $pH_2O$ , the highest water partial pressure value examined, exceeds that of random nanocrystalline ceria measured at 20 mbar  $pH_2O$  by a factor of 4 at 300 °C [72]. The result suggests that the aligned pore structure has provided measurable enhancement to the protonic conductivity.

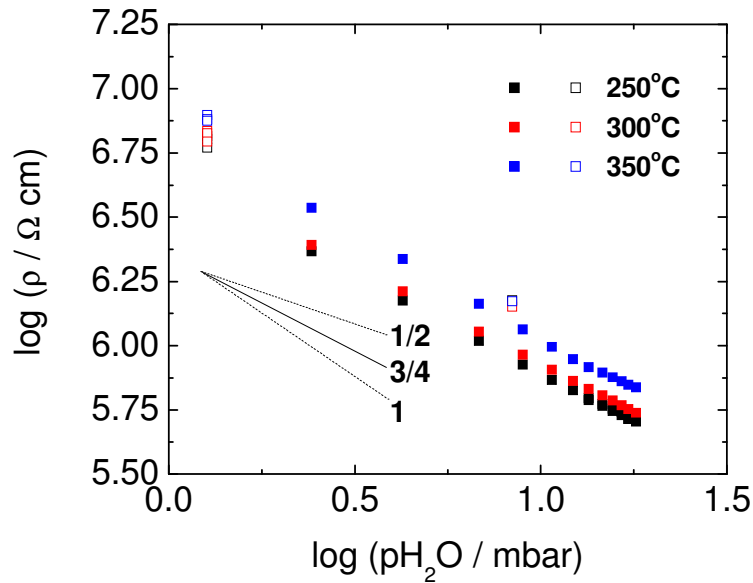


Figure 3.8 Resistivity isotherms presented in double-logarithmic form. Open symbols: film 1. Closed symbols: film 2. For film 2, the isotherms display slopes in this representation of  $-0.758 \pm 0.006$ ,  $-0.750 \pm 0.002$ , and  $-0.81 \pm 0.01$  at 250, 300, and 350°C, respectively.

The double logarithmic presentation of resistivity in Fig. 3.8 not only captures the decrease in  $\rho$  with increasing  $p\text{H}_2\text{O}$  already noted, but also shows the dependence to be exponential. The power law exponent was evaluated for Film 2, examined at a greater range of water partial pressure values, and was found to be to  $-0.758 \pm 0.006$ ,  $-0.750 \pm 0.002$ , and  $-0.81 \pm 0.01$  at 250, 300 and 350°C, respectively, in all cases rather close to  $\frac{3}{4}$ . In an oxide in which proton uptake occurs in the bulk and oxygen vacancies are the predominant positive defects, the dependence of proton concentration on water vapor pressure can be predicted from the generic proton incorporation reaction:



Over a small change in proton concentration (the observed variation on conductivity is only about 10%) and under the approximation of ideal solution behavior, Eq. (3.1), implies that the proton concentration should display a power law factor of  $-1/2$ , as opposed to the  $-3/4$  observed here. It is noteworthy that a  $-1/2$  dependence has, in fact, been previously reported for proton conducting Gd-doped ceria at 200 °C (grain size  $\sim 108$  nm) [80]. There are many factors that could explain a deviation from a power law factor of  $-1/2$  in undoped ceria even for bulk proton uptake, first amongst these being the low intrinsic oxygen vacancy concentration such that the effects of site saturation cannot be neglected. Nevertheless, the preponderance of the evidence suggests that the observed behavior reflects the characteristics of the surface absorption isotherm for  $\text{H}_2\text{O}$  molecules on nanocolumnar ceria. Further experimentation, beyond the scope of the current work, is required to understand the origin of the  $-3/4$  power law exponent.

### 3.5 Conclusion

Through-plane a.c. impedance measurements were performed on MOCVD grown columnar ceria films. Proton conductivity was detected at temperatures below 350 °C regardless of gas phase water vapor pressure, as indicated by an increase in conductivity with decreasing temperature and increasing water vapor pressure. The capacitance, in all cases, is consistent in magnitude with the bulk dielectric response. Accordingly, the material is interpreted to display proton conductivity along the surface of the columnar grains, in parallel with bulk capacitance. At conditions corresponding to intermediate proton conductivity ( $T = 100$  to  $250$  °C) the impedance response changed from a

somewhat ideal arc in the Nyquist representation to one with detectable distortion. It is proposed that under such conditions proton surface uptake adopts an intermediate value relative to the available sites and hence a distribution of proton environments exist, leading to a distribution of relaxation times. In the most extreme cases, two distinct arcs emerged, suggesting two classes of relaxation processes. In the region of proton conductivity (high  $p\text{H}_2\text{O}$ ), a power law dependence of conductivity on water vapor pressure was observed, with a power law exponent of  $-3/4$ . The origin of this behavior is unknown, but given the expectation of a power law exponent of  $-1/2$  for bulk proton uptake, the result is taken to support the conclusion of surface proton conductivity. Grain boundary impedance at the interfaces between the grains forming the columns was not observed under any situation. It can be concluded that such interfacial resistance is either overwhelmed by the parallel proton transport or that overlapping space charge zones originating at the grain boundary interfaces implies no distinction between grain interior and grain boundary regions. It is not uncommon to observe a single-arc impedance response from nanostructured, undoped ceria, as reported here, and the result is most often attributed to the latter effect. Overall, the aligned pore structure of the ceria columnar films resulted in factor of 4 higher proton conductivity compared to nanograined ceria sintered pellets.

## Chapter 4

# Electrochemical characterization

### 4.1 Summary

In this chapter, electrochemical aspects of the MOCVD grown doped/undoped ceria films are studied. Relevant electrochemical reaction is hydrogen electrooxidation, the anode reaction in a hydrogen fuel cell. Two different configurations for AC impedance measurement are adopted for electrochemical characterization: symmetric with embedded current collectors and asymmetric with point contact current collectors. For symmetric cell geometry, Pt line patterns formed on YSZ single crystal electrolyte were used for current collection. Ceria films were grown over the metal lines (embedded current collector). Using this geometry, we looked into effect of (i) Sm doping level and (ii) film growth pressure on area specific resistance (ASR) around zero net current condition. It was found that Sm doping level has no strong correlation with electrochemistry. What overrides the Sm doping level is the microstructural factor, which we interpret as preferred orientation. We tried to control preferred orientation by varying film growth pressure. Most interestingly, preferred orientation is correlated to differences in gas reaction orders and absolute ASR value. A hypothesis is proposed to explain this phenomenon.

For the asymmetric cell geometry, U shaped metal wires (Ni, Pt, and Au) are gently pressed onto the surface of MOCVD grown ceria film forming a working electrode. In this case, all current collectors were directly exposed to experimental gas environment. Comparisons are made for the three metals. For this configuration, AC impedance arcs

were collected under anodic bias and cathodic bias to study electrochemistry under more realistic fuel cell operation condition. It was found that ASR depends on what metal is in place suggesting ceria/gas interface reaction is not the sole factor that determines overall kinetics.

## 4.2 Introduction

### 4.2.1. *Electrode resistance*

In electrochemistry, electrode resistance is a metric that is related to how fast an electrochemical reaction takes place. Because the total current flowing through an electrode is, at a macro scale, proportional to its area, it is most meaningful to evaluate electrode behavior in terms of area normalized quantities (i.e., current density rather than current). The voltage - current relationship of an electrochemical process is typically non-linear as shown schematically in Fig. 4.1. The potential drop across the electrode is often termed overpotential in the fuel cell literature to distinguish this voltage from that resulting from the global fuel cell reaction (e.g.,  $\text{H}_2 + \frac{1}{2} \text{O}_2 = \text{H}_2\text{O}$ ). The slope of the I-V curve is the electrode resistance. When area normalized, this is the electrode area specific resistance, and commonly the specification “electrode” is omitted so that the acronym ASR is used to describe electrode behavior. In an impedance measurement without biasing, the measured ASR corresponds to the slope at the origin (zero overpotential, red colored slope in Fig. 4.1).

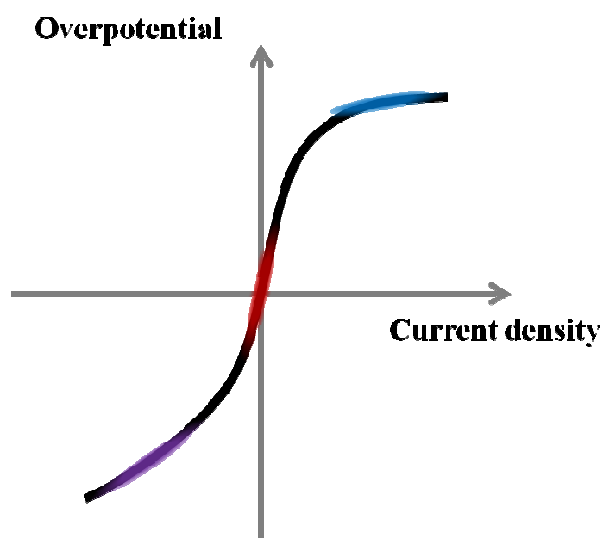


Figure 4.1 Polarization curve of an electrode. Three different ASR values are indicated as slopes along the polarization curve. Positive current is taken to be anodic current.

#### 4.2.2. Background and experiment design

Many efforts have been made to characterize electrochemical aspect of the fuel cell electrode reaction. Cathode reaction, oxygen electro-reduction, is far more often studied compared to anode reaction, hydrogen electrooxidation. Part of reason behind this is experimental simplicity in studying cathode reaction since only one type of gas, oxygen, is involved. Moreover, with traditional cathode materials, cathode reaction has been attributed to comprise major part of the total electrode overpotential. However, with the recently found high performance cathodes such as BSCF ( $\text{Ba}_{0.5}\text{Sr}_{0.5}\text{Co}_{0.8}\text{Fe}_{0.2}\text{O}_{3-\delta}$ ), anode becomes rate-limiting, and it becomes important to understand anode reaction to reduce total electrode overpotential.

In general, unambiguous determination of electrochemical reaction mechanism is quite hard since there are many factors that can affect the magnitude of ASR. Even for the most simple, long studied system, Pt\_YSZ, there are ongoing efforts to understand the



mechanism fully [81]. In many old studies, realistic electrode with porosity is adopted.

This leads to poorly defined geometry, which inevitably complicates the interpretation of the ASR behavior. Recent trend is to employ geometrically and microstructurally well-defined electrodes without porosity eliminating complications [22, 24, 40, and 41].

Historically, there have been two main categories for pore-free model electrodes: patterned electrode and point electrode (microcontact electrode). Patterned electrode is first introduced by Mizusaki [42]. This geometry has already been utilized in the current group to elucidate the catalytic activity of the ceria over metals (Pt, Ni) [24]. Point electrode is first introduced by Kleitz [82], and applied to both cathode and anode materials [83]. Modern variation of this point electrode concept is to form circular microcontact electrodes by microfabrication technique [22, 40, and 41]. Typical approach is to vary diameter and thickness of microcontact electrodes and see corresponding change in ASR.

In the present work, we employed either (i) embedded patterned electrodes which eliminate the complication of applying current collecting metal phase on top of porous columnar structure (symmetric cell), or (ii) very simple point contact electrode made of a U shaped metal wire pressed onto the top surface of columnar film (asymmetric cell). We investigated two factors, (i) Sm doping level and (ii) film growth pressure with the embedded patterned electrode in a symmetric cell setup. Point contact electrode allows biased measurements away from net zero current condition. For this asymmetric cell setup, instead of varying the diameter of the microcontact electrode, we estimate the electrochemically active zone around point contact electrode according to features of collected impedance spectra. This is the only way to estimate the active area since the

electrode under study is not fully dense rendering pre-determination of the electrode area impossible.

In anode electrochemistry study, water vapor pressure and hydrogen pressure should be controlled independently to capture the whole picture, which is rarely done in literature. Only three papers [42, 84, and 85] report systematic, independent control of the two gases for model anodes, and they were performed on Ni-YSZ system. In the present work, 16 different gas compositions were tested per symmetric cell at fixed temperature (650°C) as shown in Fig. 4.2. Experimental sequence ensures gradual change of oxygen pressure to minimize randomness in stress due to volume expansion upon reduction.

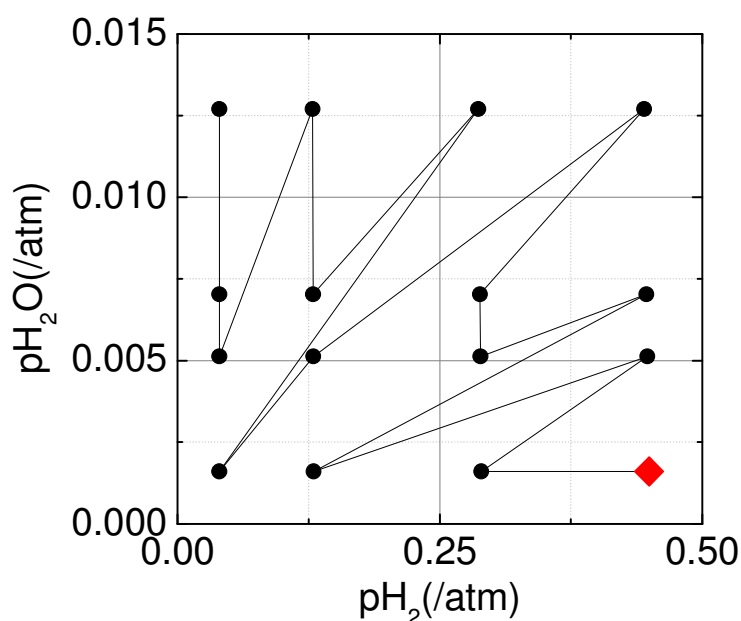


Figure 4.2 Gas compositions. A 4 by 4 matrix is intended to map out the gas dependence of ASR. Lower right corner corresponds to low oxygen partial pressure, and upper left corner corresponds to high oxygen partial pressure. For all cases, measurements were made in the sequence of shown dot connection. Starting point is marked as a red diamond.

For a symmetric cell, what is measured is the slope at zero current density in Fig. 4.1, and the response comes from convolution of forward reaction rate (positive current density) and reverse reaction rate (negative current density). In an asymmetric cell, what is measured is either blue (under anodic bias) slope or purple (under cathodic bias) slope at certain level of current density depending on the polarity and magnitude of bias. Again, the slope,  $(\partial\eta/\partial i)$ , is the ASR. It is possible to investigate only one direction since almost entire voltage drop (after ohmic drop compensation) will occur at the point electrode rather than counter electrode due to much larger resistance. This is the idea behind the asymmetric cell geometry (referenceless setup where counter electrode works as reference electrode at the same time). In an electrochemical setup, what one wants to achieve for a reference electrode is zero current density on it. In referenceless setup, the current density is never zero. However, it is relatively very small compared to that of working electrode so that the extent of isolation,  $\xi$ , becomes close to 1. This extent of isolation,  $\xi$ , is defined as the ratio of the working electrode overpotential to the sum of electrode overpotentials; thus,  $\xi = \eta_{WE}/(\eta_{WE} + \eta_{CE}) = R_{WE}/(R_{WE} + R_{CE})$  [86]. This is a term introduced to assess how well one has designed asymmetric electrode geometry to separate out only working electrode response. In literature [86], it was shown that we need high isolation values ( $\xi > 0.99$ ) to safely neglect the overpotential contribution of the counter electrode.

Fig. 4.3 shows impedance sample setup for electrode ASR measurements.

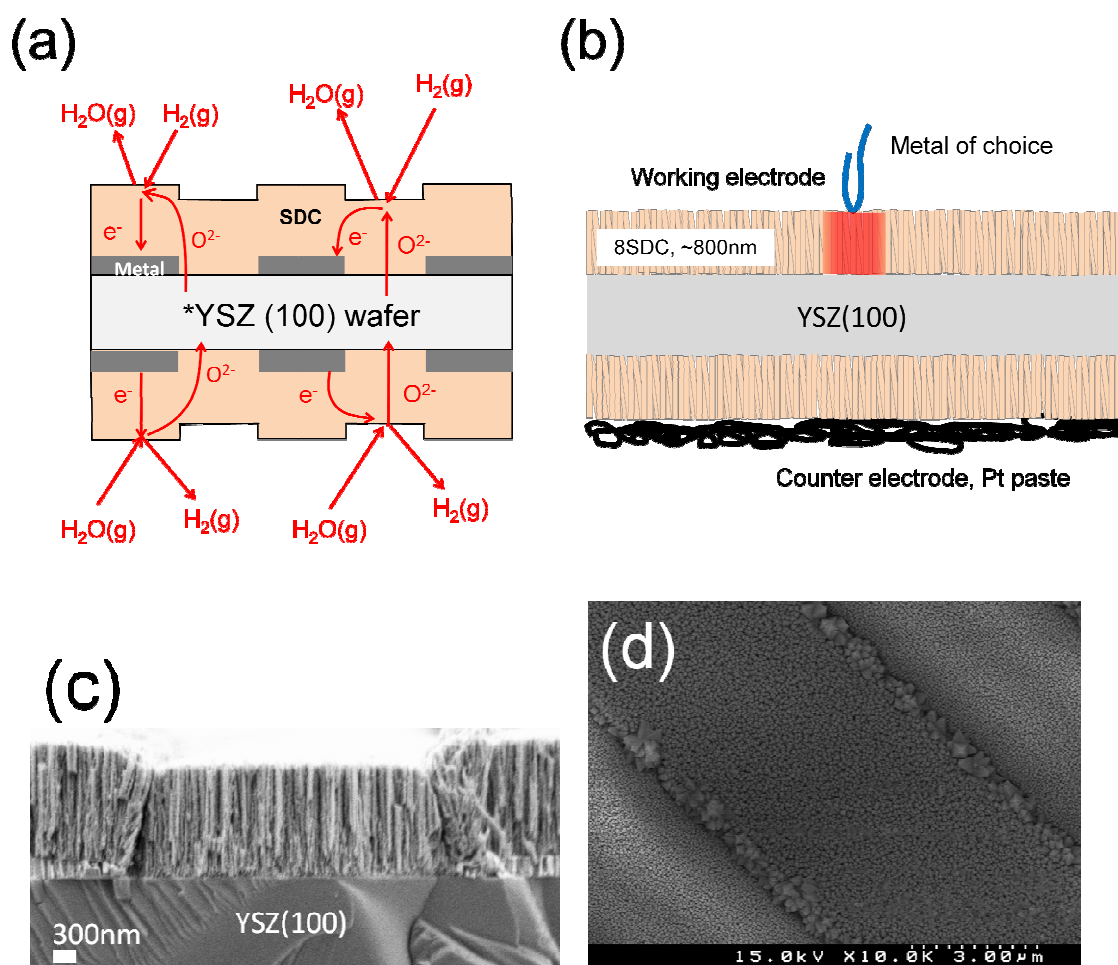


Figure 4.3 (a) Schematic view of a symmetric cell under AC impedance test. SDC (or ceria) films work as an anode on one side and as a cathode on the other side. (b) An asymmetric cell. Working electrode is a classic point electrode. The electrochemically active volume is marked with red shade. (c) Cross-cut view of the symmetric cell. One can see two Pt pattern lines (brightest regions). (d) Top view of the symmetric cell. The center part looks elevated since that part is grown on a Pt line.

All samples reported in this chapter have film thickness ranging from 550 to 900nm. This is confirmed by SEM cross-sectional imaging. Energy dispersive spectroscopy (EDS) is used to estimate Sm doping level (Fig. 4.4). EDS analysis area was selected on the portion of the film that is deposited on Pt borderlines around substrate edge where all the metal lines join together (Fig. 4.5). This is to minimize the effect of grooves coming from metal line height (~200nm) and to minimize surface charging that is detrimental to quantitative element molar ratio determination. It is assumed that doping level will not change whether the film is formed on Pt lines or on bare YSZ (100) substrate surface. The detailed procedure for metal line pattern fabrication has been reported elsewhere [24].

Doping level control is done by changing the argon push flow rates for Ce source and Sm source while keeping the total argon push flow rate at 100sccm. This is believed to be more straightforward than changing source evaporator temperature since precursor vapor pressure is a strong function of temperature. Varying Sm source push flow rate affects the resultant microstructure as reflected in typical  $\theta$ -2 $\theta$  XRD scan (Fig. 4.6). Relative intensity of (111) peak and (200) peak is of primary interest (Fig. 4.6 and Fig 4.7). Deposition pressure also affects the resultant preferred orientation (Fig 4.7). It is not straightforward to change only one factor without affecting other factors. For example, as seen in Fig 4.4 and Fig 4.6, doping level variation by argon flow rate control also has an impact on microstructure. For films grown with different deposition pressures, argon push flow rates had to be adjusted accordingly to keep Sm doping level within acceptable window. In Fig 4.7, one can find a trend in relative intensity (preferred orientation) depending on deposition pressure. Relative intensity approaches the value of randomly

packed powder as deposition pressure increases. As deposition pressure decreases, the resultant film microstructure shows more significant deviation from random powder packing.

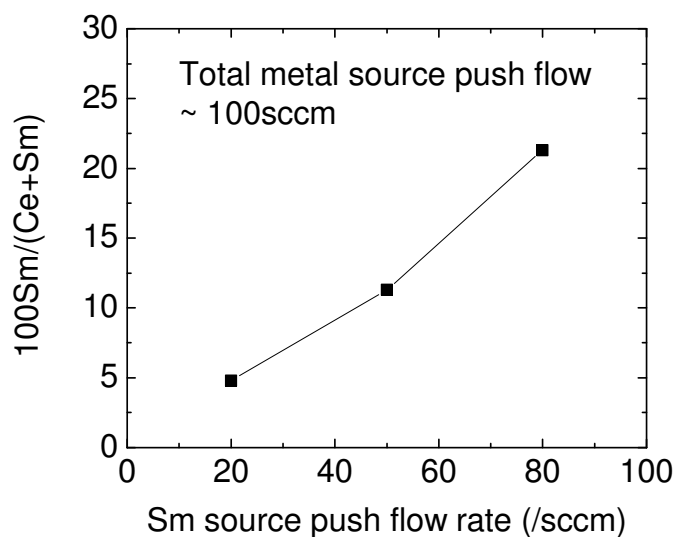


Figure 4.4 Sm cation molar fractions in percentage as measured by EDS. Three different argon push flow rate combinations are shown (Ce:Sm=80:20, 50:50, 20:80). In all cases, oxygen flow is 50sccm. Growth temperature: 600°C. Growth pressure: 3Torr. Growth time: 60min. Substrate: YSZ (100) single crystal wafer with platinum line patterns (Fig. 4.5).

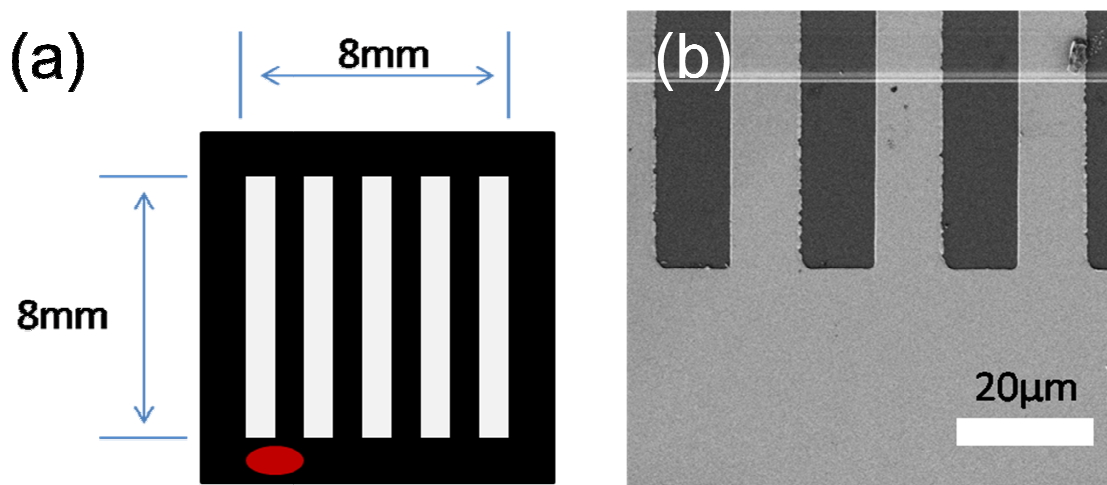


Figure 4.5 (a) Top down schematic of the YSZ (100) single crystal substrate with platinum line pattern atop. Black colored lines stand for platinum line pattern. Gray “lines” are exposed YSZ surface. Pt line patterns cover half of the YSZ surface due to equal width ( $10\mu\text{m}$ ) of the metal lines and YSZ “lines”. After film deposition, EDS composition analysis is done on the area marked in red. SEM image of such area is shown in (b).

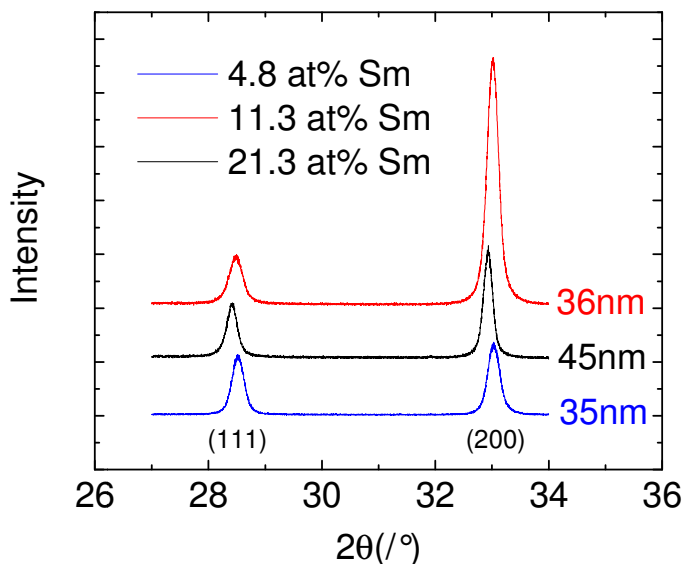


Figure 4.6 XRD patterns of the Sm doped ceria thin films in Figure 4.4. The numbers next to intensity profile are grain sizes calculated from (200) peak broadening. Patterns are vertically shifted for ease of comparison.

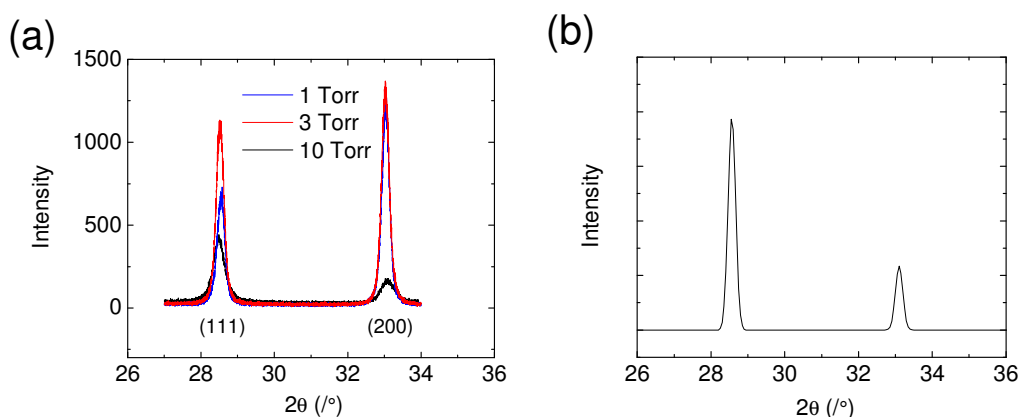


Figure 4.7 (a)  $\theta$ - $2\theta$  scans for Sm-doped ceria films (Sm 5~8 at%) grown with different deposition pressures. Growth temperature:  $600^{\circ}\text{C}$ . Growth time: 60min. The substrates are YSZ (100) single crystal wafer with Pt line patterns (Fig 4.5). Argon push flow rates for 1 Torr film; Ce:Sm=50:50. For the other two films; Ce:Sm=80:20. (b) Calculated diffraction profile for randomly packed ceria powder.

### 4.3 Sm doping level effect

At first, we tried to establish a correlation between ASR and the Sm doping level using symmetric cells with embedded metal line pattern current collector (Fig. 4.3(a)). The deposition pressure was held at either 3Torr or 10Torr.

Fig. 4.8 shows a representative set of impedance arcs (raw data) under different gas compositions. One immediately notices that there are two arcs per spectrum. The one at high frequency does not change upon gas composition variation. On the contrary, the other one at low frequency changes its size when exposed to different gas compositions. From this observation, one can conclude that the low frequency arc is the one related to the surface electrochemistry. It should be noted that the bulk diffusion process contribution is negligible since we are using thin films as test material.

The origin of the high frequency arc remains unclear in a previous study using PLD films. Because this high frequency arc can be eliminated under suitable electrode



geometries (for example, by applying a PLD layer of SDC beneath the patterned metal current collector [87]), it can be concluded that it is not fundamental to the electrochemical process. Accordingly, in the following section, if not noted otherwise, ASR means area specific resistance from low frequency arc, and the area used for normalization is always the total projected area (area of thin film on Pt lines + area of thin film on YSZ “lines”). In Fig. 4.5, this normalization area is marked as 8mm by 8mm square.

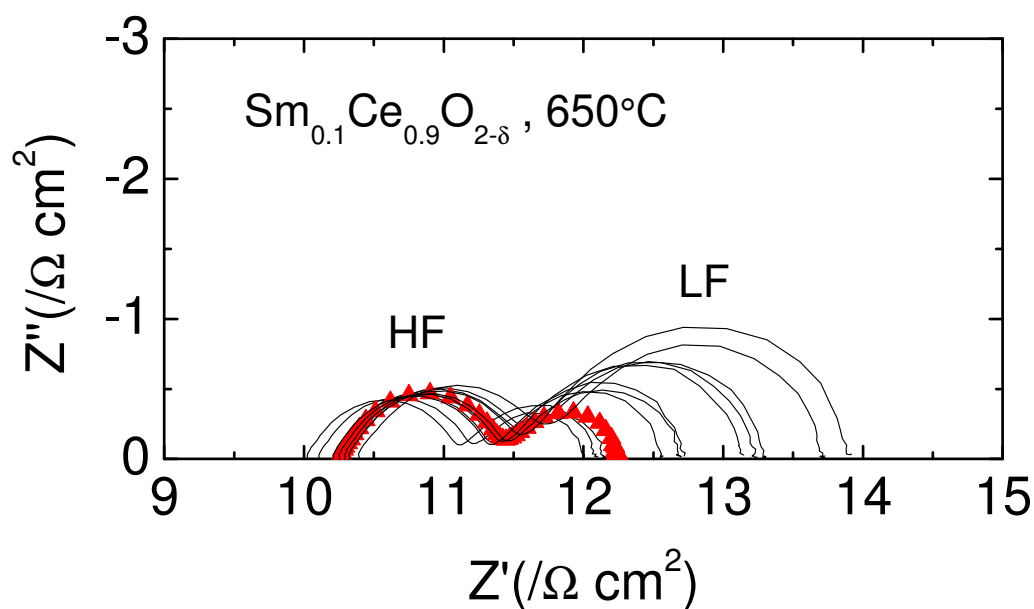


Figure 4.8 Superposition of impedance arcs after area normalization. One spectrum is highlighted to help reader's interpretation. HF: high frequency, LF: low frequency.

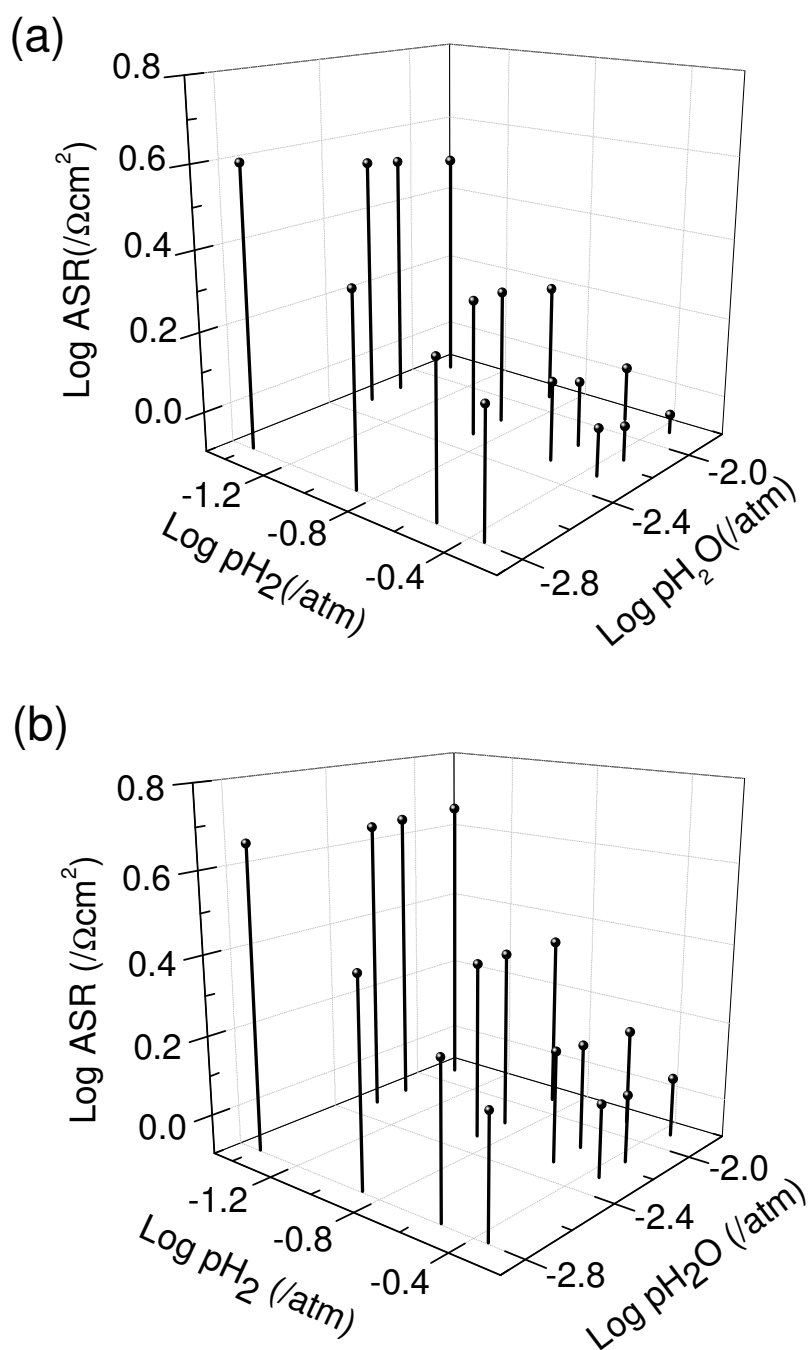


Figure 4.9 ASR behavior map for two different doping levels at 650°C. Both films were grown at 600°C at 3Torr. (a) 5% Sm-doped ceria film. (b) Undoped ceria film. One can see small but non-negligible difference in the gas dependence.

In Fig. 4.9, two doping levels are compared. Reaction order against hydrogen ( $n =$

$$-\frac{\log ASR}{\log pH_2} \bigg|_{pH_2O}) \text{ is very similar, but reaction order against water } (m = -\frac{\log ASR}{\log pH_2O} \bigg|_{pH_2})$$

shows small but noticeable difference between this specific pair. In general, high water content and high hydrogen content leads to the best performance (smallest ASR), and this is the closest condition explored to the real fuel cell anode gas. In the real fuel cell anode condition, hydrogen content and water content will increase replacing argon, and we expect to see even smaller ASR than reported here.

Instead of showing 3D graphs for each sample with different doping level, we summarize the reaction order result in a table (Table 4.1). Specific ASR values at two different gas combinations are included as respective columns to show the general trend.

Table 4.1 Gas dependence and ASR (650°C) trend on Sm concentration (3Torr deposition)

<i>Nominal doping level</i>	<i>pH<sub>2</sub>O / m</i>	<i>pH<sub>2</sub> / n</i>	<i>*ASR / Ωcm<sup>2</sup></i>	<i>**ASR / Ωcm<sup>2</sup></i>
Undoped (4 samples)	0 ~0.2	0.4~0.6	1.1~3.0	2.2~2.5
5% (2 samples)	0.1~0.3	0.4~0.5	0.9	1.8~1.9
10% (2 samples)	0.1~0.4	0.3~0.5	0.4~0.7	0.4~1.3
20% (1 sample)	0~0.1	0.5~0.6	2.3	4.9

\*pH<sub>2</sub> = 0.447atm, pH<sub>2</sub>O = 0.013atm, \*\*pH<sub>2</sub> = 0.13atm, pH<sub>2</sub>O = 0.005atm

The range of values for ASR comes solely from the use of multiple samples. Gas reaction order shows a range of value since there are 4 values per sample (Fig. 4.2, 4 by 4 matrix) in addition to multiple samples. From the table, strong hydrogen dependence and weak water dependence prevails over all doping levels with varying extent. If the rate determining step is a water related process, one should expect a strong dependence on water partial pressure. If the rate determining step is a hydrogen related process, one should see strong hydrogen dependence. For all films grown at 3Torr, strong water dependence ( $m > n$ ) has never been observed. Thus, rate determining step is not water related. In Table 4.1, strong hydrogen dependence appears to be linked to large ASR (undoped films and a Sm 20% doped film). In other cases (5% and 10% doped films) with smaller ASR, even though hydrogen dependence is still stronger than water dependence, the extent is lesser.

Films grown at 10Torr with two different doping levels are compared in Fig 4.10. Again, ASR trend on gas reaction order stays same. The worse electrode (5% nominal Sm doping level) shows strong hydrogen dependence ( $n = 0.4 \sim 0.5$ ) and weak water dependence ( $m = 0 \sim 0.1$ ). The better electrode with 20% nominal Sm concentration shows opposite tendency of strong water dependence and weak hydrogen dependence ( $m = 0.4 \sim 0.5$ ,  $n = 0.2 \sim 0.3$ ).

Even though the ASR-gas reaction order correlation shows remarkable consistency in films grown at two different deposition pressures, it is hard to draw a conclusion on ASR dependence on Sm doping level. Regarding 3Torr films, it is not clear why undoped and heavily doped (20%) films show similar behavior as color-coded in Table 4.1. In addition, 10Torr film with 20% doping shows better performance than 5% doped film in contrast to the trend in 3Torr films.

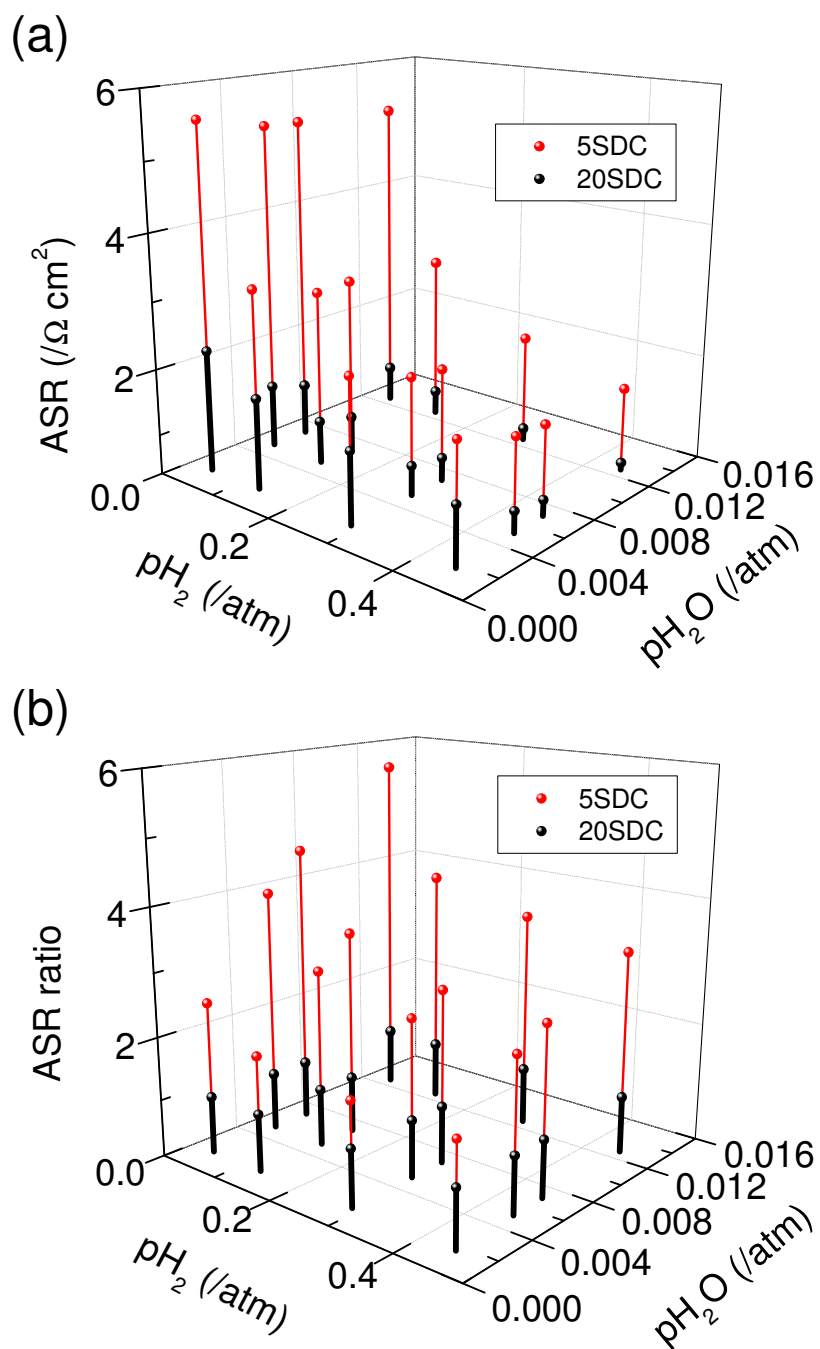
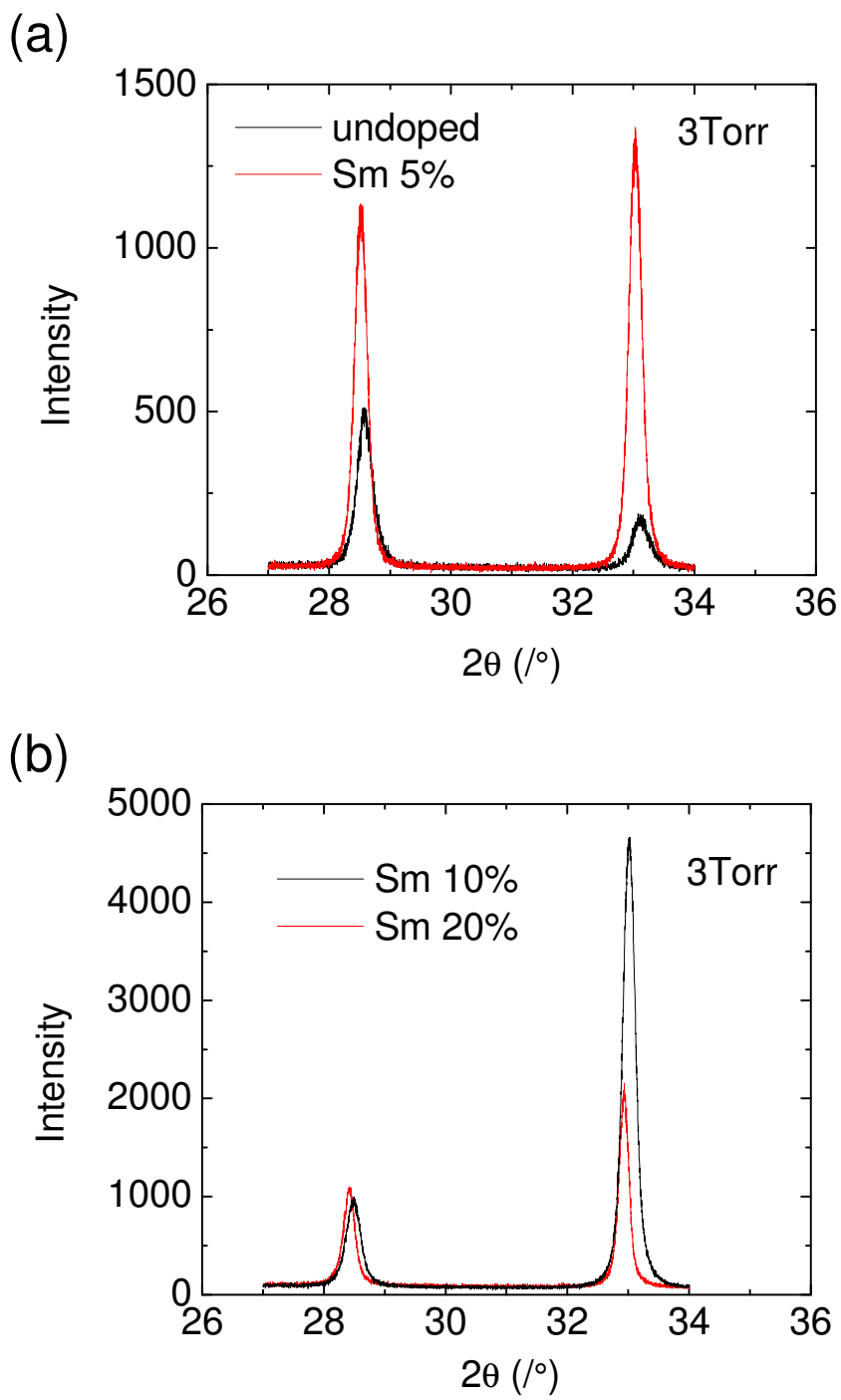


Figure 4.10 ASR behavior map for two different doping levels at 650°C. Films are grown at 10Torr. (a) Linear scale comparison. (b) After normalizing to 20SDC ASR.

Since the doping level does not provide satisfactory correlation with resultant electrochemical performance, we turn to other microstructural features. Fig. 4.11 lists XRD patterns of 6 representative samples in this section.



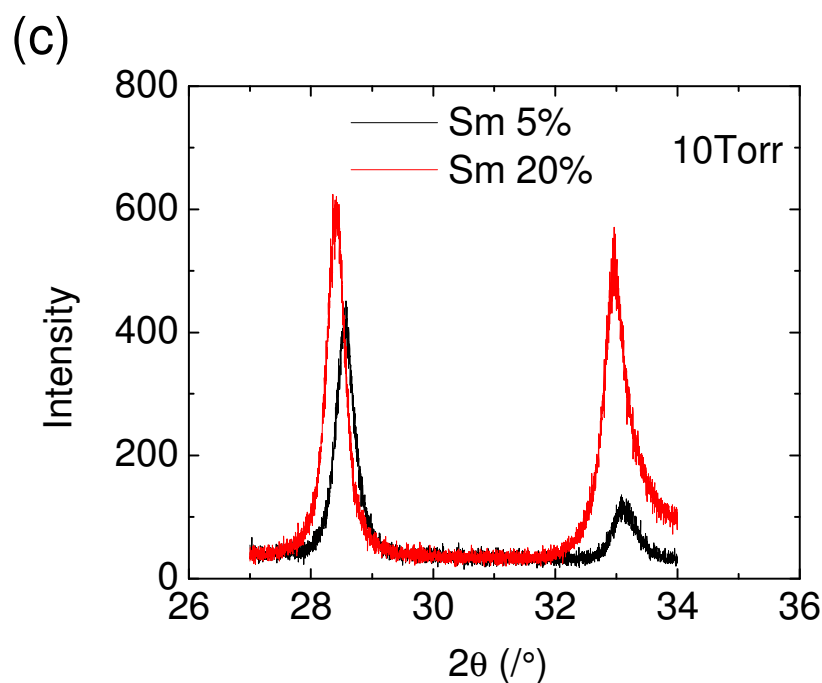


Figure 4.11 XRD patterns for films grown at 600°C for 60 minutes. Deposition pressure is specified in the graph. (a) Films in 1<sup>st</sup> and 2<sup>nd</sup> rows of Table 4.1. (b) Films in 3<sup>rd</sup> and 4<sup>th</sup> rows of Table 4.1. (c) Films in Fig. 4.10.

From Fig. 4.11, it appears that the intensity ratio of 111 peak and 200 peak is related to resultant gas reaction order. Does strong 200 peak over 111 peak lead to high water dependence, and hence better performance? This question motivated the following section where we try to vary preferred orientation only.

#### 4.4 Preferred orientation effect

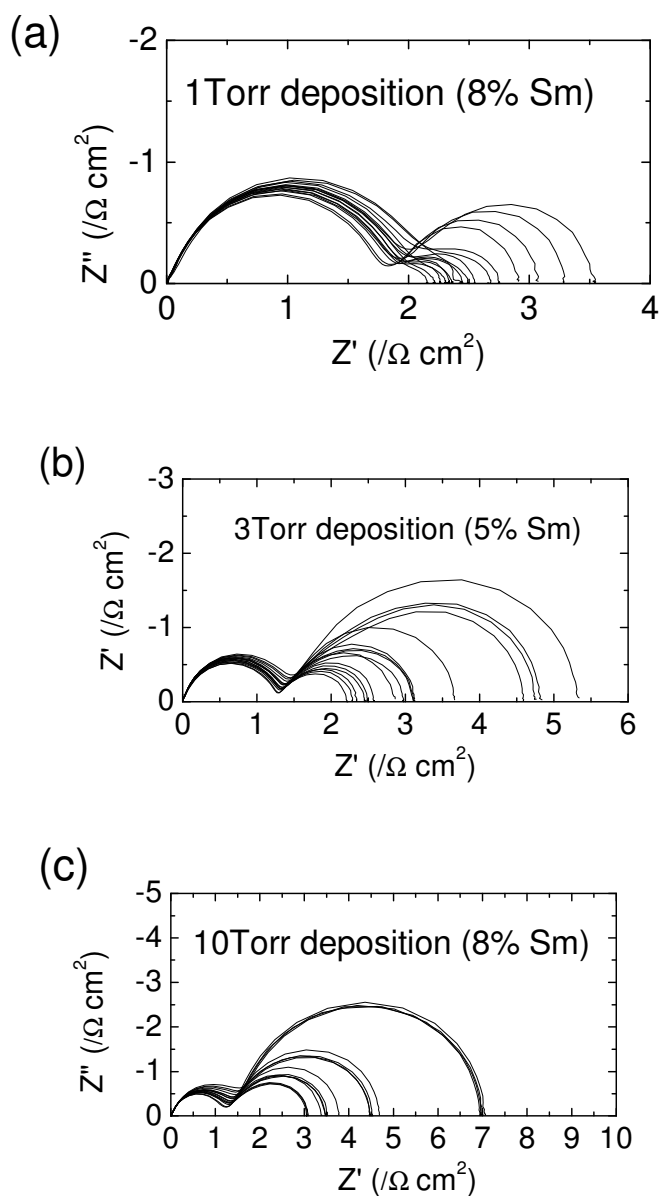


Figure 4.12 Impedance arcs for films grown at different pressures. Electrolyte resistance has been subtracted so that only non-ohmic loss is present. Each panel contains 16 impedance spectra from different gas compositions already mentioned (Fig. 4.2). Measurement temperature: 650°C. Film thickness; 1Torr film: 650nm, 3Torr film: 675nm, 10Torr film: 555nm.



In this section, the preferred orientation effect is studied with symmetric cells with embedded metal line pattern current collector (Fig. 4.3(a)). Three different deposition pressures are used to get the resultant preferred orientation (Fig. 4.6).

Fig. 4.12 shows impedance arcs from films grown at difference pressures. The X-ray scans for these films are already given (Fig. 4.6). It is easy to see that the film grown at 1Torr shows the best performance. This is more clearly shown in Fig. 4.13.

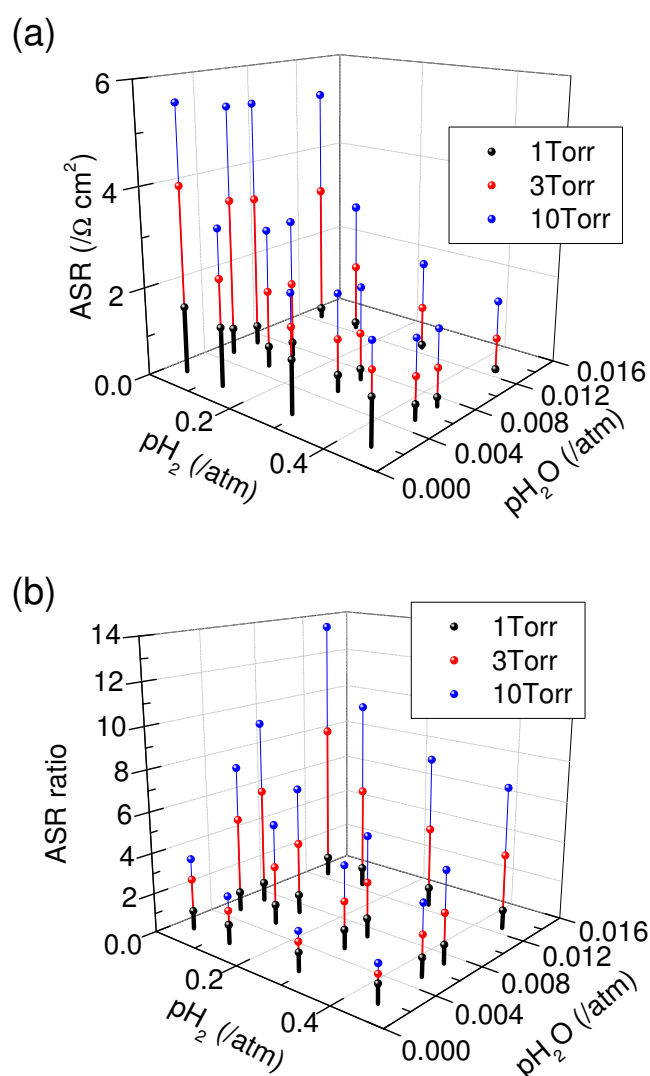


Figure 4.13 ASR behavior map for three films grown at different pressures at 650°C. (a) Linear scale comparison. (b) After normalizing to 1Torr ASR.

Table 4.2 Summary of the three films with different deposition pressures

Deposition pressure (/Torr)	Sm doping level (/%)	Grain size (/nm)	Film thickness (/nm)	X-ray peak ratio $I_{200}/I_{111}$
1	8	29.8	650	1.82
3	5	32.7	675	1.20
10	6	20.6	555	0.35

ASR decreases with deposition pressure as shown in Fig 4.13. The fundamental difference between these three samples lies in the preferred orientations. Quantitative metric for this is the ratio of the diffraction peak intensity, and this can be found in Table 4.2. Doping level (measured by EDS) and grain size (calculated from 200 peak broadening) are kept within acceptable window. Both of them cannot provide self-consistent explanation for the ASR trend.

In addition, it is interesting to see the similarity in ASR ratio shown in Fig. 4.10(b) and Fig. 4.13(b). This suggests that the fundamental factor that determines ASR behavior is not the Sm dopant concentration but the microstructure, probably preferred orientation.

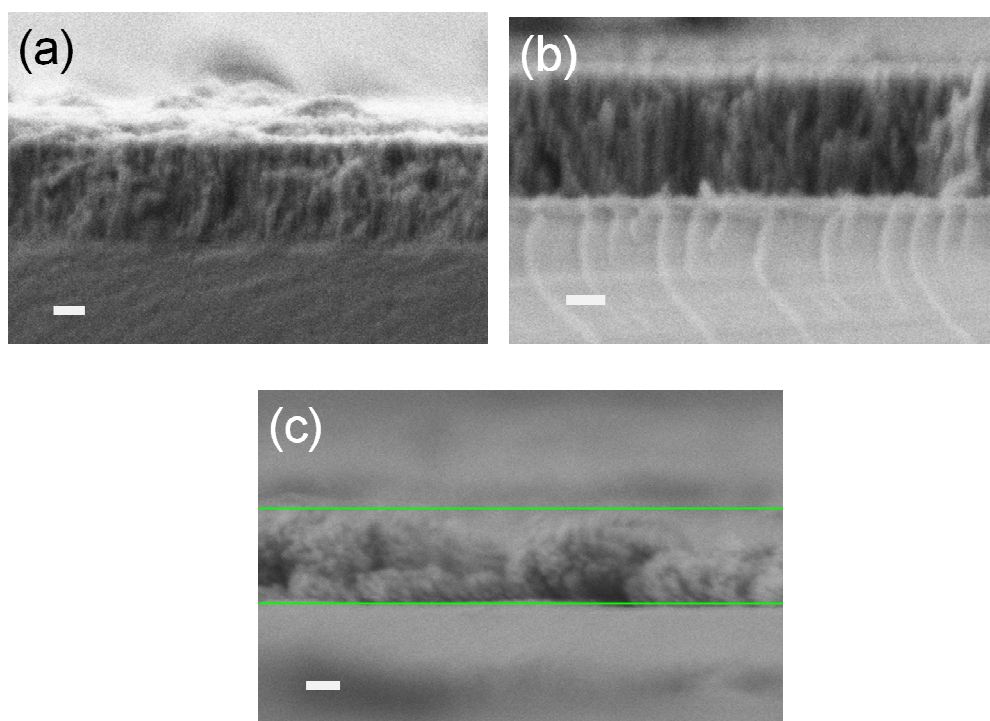


Figure 4.14 Cross-sectional secondary electron microscopy images taken after impedance measurements. 200nm scales bars for all three images. (a) 1Torr film. (b) 3Torr film. (c) 10Torr film.

One can see a significantly different film microstructure for 10Torr deposition in Fig. 4.14. This film does not show columnar structure. It looks like a randomly packed powder assembly. This observation is in good agreement with X-ray peak intensity ratio results.

Table 4.3 summarizes the reaction order results for orientation control measurements. The most interesting feature is that the gas dependence changes along with the degree of alignment. Plus, the best performance is achieved for the most aligned, 1Torr deposition film. Surface area of the films (potentially related to the grain size of the film) is believed not to play any major role here since one cannot expect that gas reaction order will

change by simple increasing or decreasing surface area of the thin film electrode. The water dependence is exceptionally strong for 1Torr deposition film, which is not observed for films grown at different pressures. From this, one can expect that the hydrogen related process is quite fast so that we cannot see the gas dependence (small  $n$ ). Water related process should be the rate determining step with relatively fast kinetics. To our surprise, the strong water dependence and weak hydrogen dependence resembles gas dependence behavior of PLD grown films with Pt nanoparticle decoration.

Table 4.3 Gas reaction order and ASR trend for orientation controlled films

<i>Pressure / Torr</i>	<i>Current collector</i>	<i>pH<sub>2</sub>O dep / m</i>	<i>pH<sub>2</sub> dep / n</i>	<i>*ASR / <math>\Omega\text{cm}^2</math></i>	<i>**ASR / <math>\Omega\text{cm}^2</math></i>
1	Embedded Pt	0.7~0.8	0.1~0.2	0.2	0.6
3	Embedded Pt	0.1~0.3	0.4~0.5	0.9	1.8
10	Embedded Pt	0~0.1	0.4~0.5	1.7	3.0
†PLD	Pt NP decoration (3~4nm)	0.8~0.9	0.12~0.15	0.1	N/A
†PLD	Pt paste	0~0.1	0.7~0.8	0.7	N/A

\*pH<sub>2</sub> = 0.447atm, pH<sub>2</sub>O = 0.013atm, 650°C †WooChul Jung, unpublished work

\*\*pH<sub>2</sub> = 0.13atm, pH<sub>2</sub>O = 0.005atm, 650°C

So far, it seems that great performance is achieved only when the hydrogen related process is fast so that water related process becomes rate determining for porous columnar films from CVD and PLD. For PLD films, strong water dependence is observed only when Pt nanoparticles are dispersed on the surface of ceria columns. It is impressive that orientation control results in the same effect as precious metal decoration.

Here, we propose a hypothesis to explain this phenomenon. When one changes orientation (degree of alignment) of the columnar structure, one cannot avoid changing atomic termination plane population at the column wall surface. It is known in literature that the ceria (111) plane is the most stable plane [88, 89]. It does not form oxygen vacancies easily, for example. If the population of (111) termination becomes lower, then one can expect to have higher apparent electrochemical catalytic activity. This would be the case for the 1Torr deposition film. As the deposition pressure increases, the microstructure approached to random powder packing (Fig. 4.7), and the population of (111) termination will take the value of this random powder packing. This hypothesis is quite hard to prove since it involves statistical determination of the atomic plane termination of the columnar structure.

To do this thoroughly, extensive TEM electron diffraction work is required. Instead, one can grow epitaxial films with (100), (110), and (111) termination with same thickness, and perform asymmetric cell measurement similar to Fig. 4.3(b) to compare ASR.

## 4.5 Asymmetric cell measurement

### 4.5.1. Metal comparison at OCV

Three different metals are compared with asymmetric set up (Fig. 4.3(b)). This was to verify the results from the previous work in the group. In a recent publication, it has been demonstrated that Sm-doped ceria is the electrochemically active phase rather than Pt or Ni [24]. If this is true, then we expect to see no difference between various kinds of metal current collector.

To make a fair comparison, it is absolutely important to have no microstructural difference between comparison samples. This applies to both metal current collector and the ceria thin film electrode. In this work, commercially available metal wires (Ni, Pt, and Au) are shaped into a U loop. To rule out any microstructural change in ceria thin film electrode, only one sample is used. In other words, only metal wires are changed between each measurement run, and everything else is kept same. Details on this single Sm doped ceria film and wires can be found in Table 4.4 and Table 4.5, respectively. Of course, it is impossible to control mechanical contact area between each trial. However, this is not a problem since we can use Newman formula [90] to estimate electrochemically active area, which does not necessarily equal to mechanical contact area. Also, it is not possible to put the point contact electrode at the exact same position for each measurement run. Given the film uniformity, this contact location variation is believed not to result in any experimentally meaningful difference. To change the metal wires, the sample has to be heated up and cooled down several times to collect ASR data. To minimize the effect of degradation by thermal shock/thermal stress, the sample was thermally cycled before

collection ASR data. Thus, the degradation/damage is thought to be already done to the sample before collection impedance arcs for metal comparison even though it is not possible to predetermine if there will be more degradation or not.

Newman formula is first derived by John Newman by solving Laplace equation [90]. It correlates measured resistance to the radius of contact area. This has been used for many publications featuring microcontact experiments in solid state ionics [40, 91]. By using this formula, we assume that the offset resistance (high frequency intercept of the electrode arc) is from the spreading resistance from the bottom surface of ceria cylindrical active volume into the bulk of YSZ substrate. All other possible contributions (metal lead wire resistance, ceria film bulk resistance) are safely ignored given the magnitude of the offset resistance. The situation is described in Fig. 4.15.

Table 4.4 Film specification for asymmetric cell measurement

Deposition pressure (/Torr)	Sm doping level (/%)	Grain size (/nm)	Film thickness (/nm)	X-ray peak ratio $I_{200}/I_{111}$
3	6	25.9	785	10.1

Table 4.5 Metal wire specifics for asymmetric cell measurement

<i>Element</i>	<i>Diameter/ <math>\mu\text{m}</math></i>	<i>Source</i>	<i>Purity/ %</i>
Pt	500	Alfa Aesar (#43288)	99.95
Ni	254	Espi Metals (Knc1225)	99.995
Au	250	Alfa Aesar (#00725)	99.9

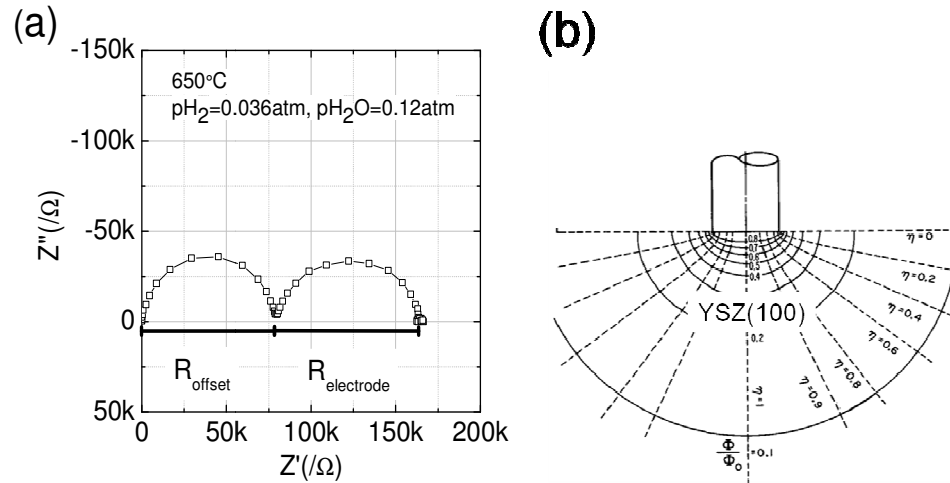


Figure 4.15 (a) A measured impedance spectrum without bias. Offset resistance is assumed to stem from the spreading resistance. The current spreading occurs within the bulk YSZ. Electrochemically active volume within ceria film is the topmost cylinder part in (b). The cylinder height equals to film thickness. Figure (b) is modified from the original [90].

Equation 4.1 presents Newman formula.

$$\sigma_{\text{YSZ}} = \frac{1}{2 R_{\text{offset}} d_{\text{active zone}}} \quad (4.1)$$



$d_{\text{active zone}}$  means the diameter of the circular active area. In reality, the active zone will not be a single circle. It would rather be a sum of irregular shaped contacts between the wire and oxide columns, but we simply treat it as a circle. In addition, derivation of Newman formula does not involve any electrochemistry and holds only when electrochemical reaction rate is infinitely fast (current density becomes infinite at the circumference of the circle). The Newman formula is believed to provide lower bound of the real contact area.

The other extreme where there is no current spreading and hence uniform current density within the circle, one can simply use the following expression;

$$\sigma_{\text{YSZ}} = \frac{t}{R_{\text{offset}} \pi (d_{\text{active zone}} / 2)^2}, \quad (4.2)$$

where  $t$  means the thickness of the YSZ substrate ( $t=0.5\text{mm}$ ). Active area calculated by this equation will correspond to the upper bound of the real contact area.

Using measured values of  $R_{\text{offset}}$ , the calculated active area without current spreading (Eq. 4.2) is always larger than Newman active area (Eq. 4.1) by two orders of magnitude. Even with this overestimated area, the diameter of the contact circle is at most just 15% of the original metal wire diameter. This seems reasonable since it should be hard to make an intimate contact by gently pressing metal wire onto the top surface of columnar film of ceria.

Without knowing the true electrochemically active area which should lie between Newman area and area from equation 4.2, we estimated the active area for each impedance spectrum, and made area normalization based on Newman formula (Eq. 4.1). In this way, random temporal variation of mechanical contact area becomes irrelevant since it will be

corrected ex-situ. Now, we can make direct, fair comparison between three choices of metal.

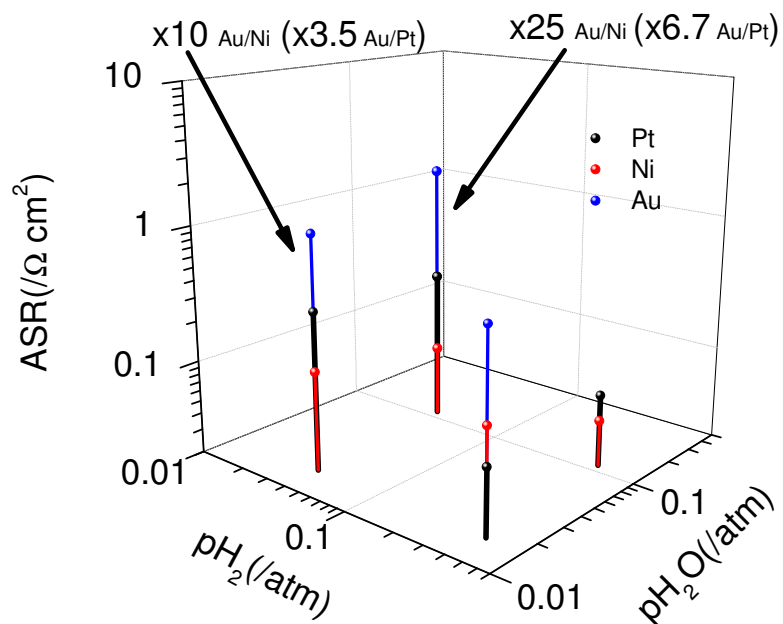


Figure 4.16 ASR comparisons of the three metals at OCV condition (650°C). Point anodes pressed on the surface of the SDC film. Au data point is missing for one gas combination.

In Fig. 4.16, one can see that there is clear difference between metals. In general, Ni shows the best performance, and Au shows the worst performance. Au is well-known for its noncatalytic behavior. If we set aside the fact that ceria is reportedly the active phase in Pt-ceria or Ni-ceria composite, the observed catalytic activity trend would then seem natural. The ASR differs as much as 25 times for gold and nickel. This surely goes beyond the level of experimental random error. The conflict between this work and the recent publication from the group [24] clearly indicates that more study needs to be directed to this issue. The conflict will be resolved if we can find the cause why the electrochemical

kinetics depends on metal choices in point electrode setup and becomes insensitive to metal choices in patterned current collector setup. In both cases, the current collector is not embedded but exposed to the gas.

#### *4.5.2. Impedance analysis under bias*

Fig. 4.17 presents impedance spectra from Nickel point electrode. Each spectrum has two arcs regardless of bias voltage. They clearly change their diameters in response to the change in bias. The impedance decreases with increasing cathodic bias (negative voltage) and increases with increasing anodic bias (positive voltage). The change in the size of the high frequency arc, representing the electrolyte resistance, reflects a change in the active area according to Eq. 4.1.

All polarized impedance arcs are recorded after 12 minute waiting time from bias onset. Then, the impedance data points were collected for 12 minutes. The bias is always set back to zero for 5 minutes between each frequency sweep. In Fig. 4.17, one can see that the arcs fall on top of each other when there is no bias. In many mixed conducting cathodes, anodic/cathodic polarization (usually much stronger than here, up to 5 Volts) is known to activate the cathode surface leading to low ASR [92]. This harsh polarization treatment has not been performed here.

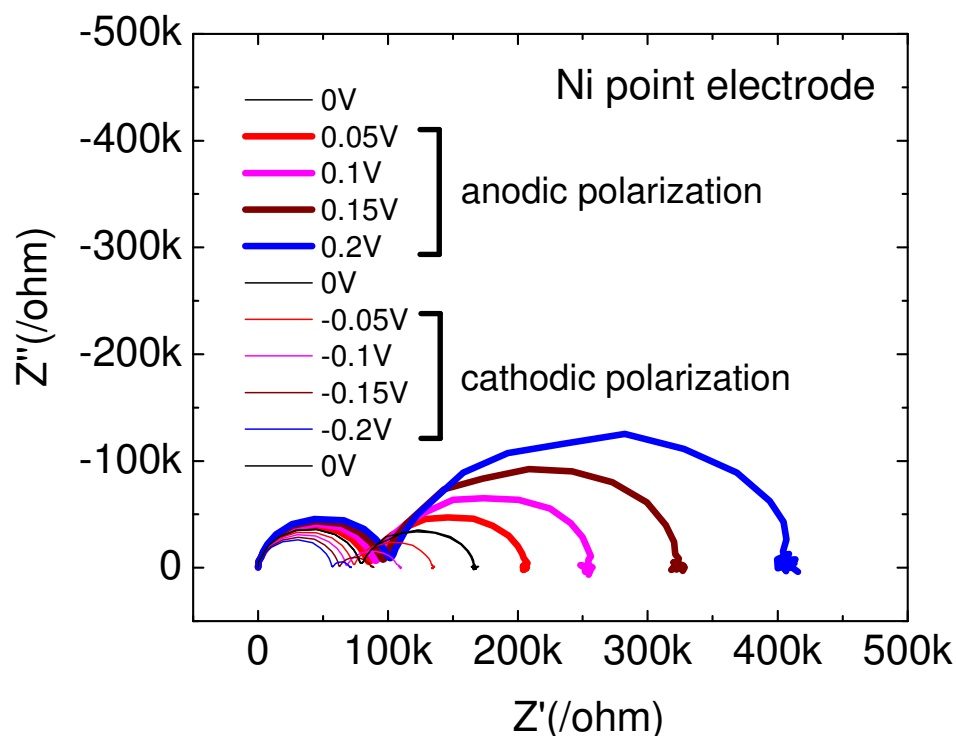


Figure 4.17 Impedance arcs under bias. The biasing sequence is indicated (0V→anodic bias→0V→cathodic bias→0V). Arcs are collected at 650°C with  $p_{H_2}=0.036$  atm and  $p_{H_2O}=0.121$  atm. Frequency range: 10MHz~5mHz.

Active area variation is estimated from Newman formula and plotted against the applied bias in Fig. 4.18. In literature,  $3 \times 10^{-5} \text{ cm}^2$  Newman contact area has been reported for lanthanum strontium manganite point electrode pressed on a polished surface of YSZ polycrystalline pellet [93]. The active area obtained here is reasonable given the columnar nature of the film. Fig. 4.17 shows that anodic bias (+ voltage against the counter electrode), in general, makes the active area shrink, and vice versa. Qualitatively, this can be explained from reduction/oxidation of the oxide by imposing electrical potential. Anodic bias brings about relatively oxidizing condition in the ceria film compared to surrounding gas, and the electronic conductivity accordingly decreases to induce shrinkage of the active area.

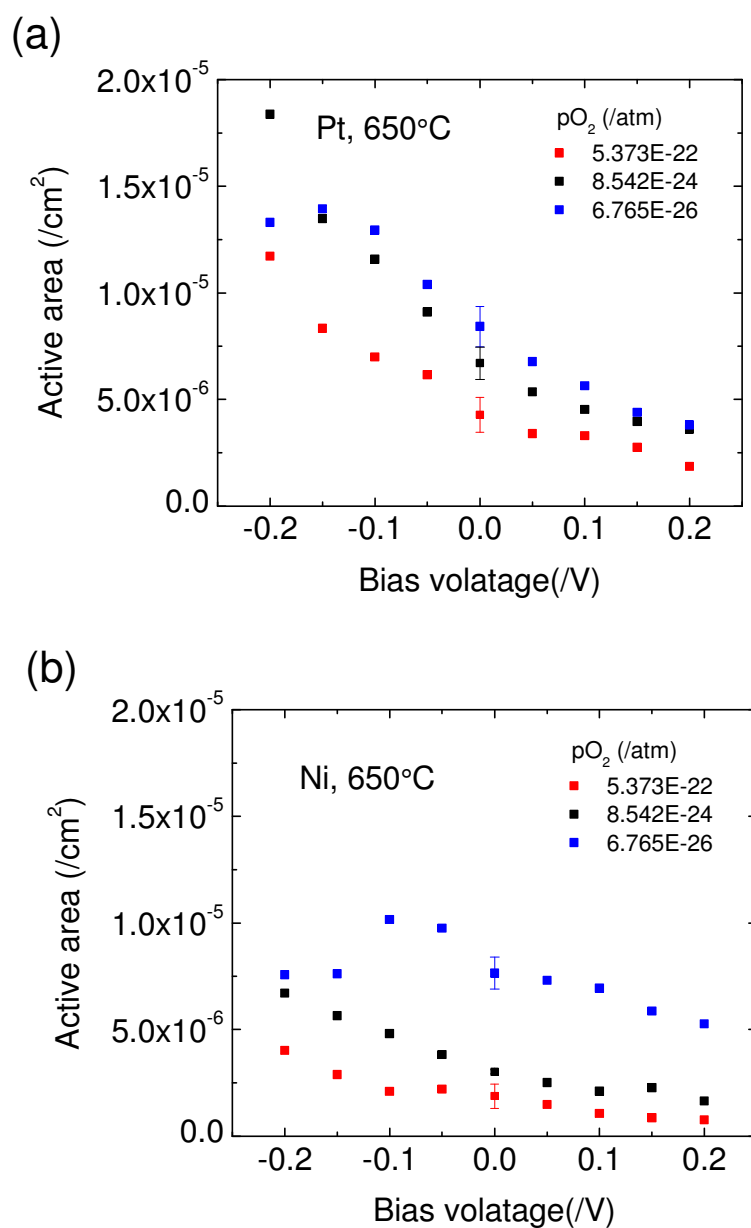


Figure 4.18 Variation of electrochemically active area under bias. Denoted oxygen pressure is the equilibrium oxygen pressure at the counter electrode, not the effective oxygen pressure within the film. Counter electrode is equilibrated to the exposed gas, and the effective oxygen pressure (chemical potential) gets changed by applying voltage.

The decrease of active area at large cathodic bias ( $-0.2\text{V}$ ,  $-0.15\text{V}$ ) and low oxygen partial pressure ( $p\text{O}_2=6.765\times 10^{-26}\text{atm}$ ) is unexpected and hard to explain. It is also hard to make quantitative analyses, since we do not know exactly how much oxygen chemical potential drop is involved at the YSZ | Sm-doped ceria interface.

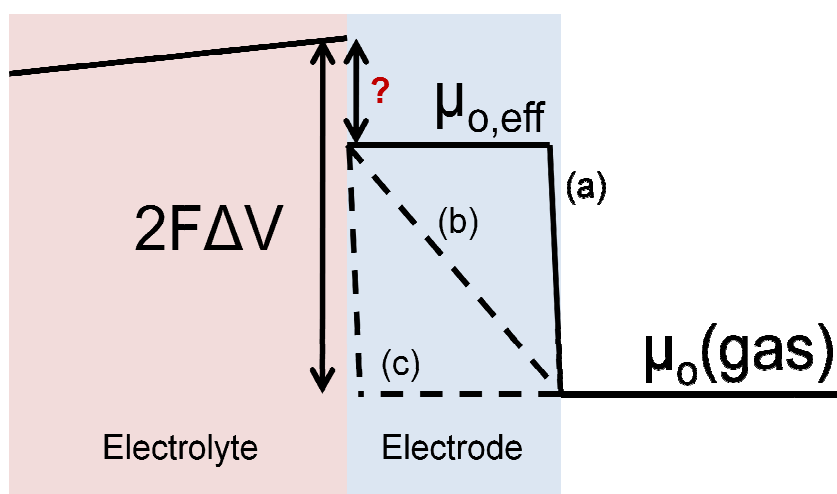


Figure 4.19 Oxygen chemical potential profiles under anodic bias. (a) surface limited case, (b) bulk diffusion limited case, and (c) electrolyte-electrode interface limited case. The discontinuity at the electrolyte-electrode interface is hard to know from collected impedance arcs, and marked with “?” here.

We believe the situation is close to case (a) described in Fig. 4.19 given the short diffusion path of film thickness.

With estimated active area at hand, we can normalize the collected impedance arc. The resultant ASRs are plotted in 3D graphs for Pt and Ni metal point contacts (Fig. 4.20). Comparing with the results at the OCV, one can see the overall gas dependence trend is kept same except the length of the bars gets longer under anodic bias and shorter under cathodic bias. From this, one can see that Butler-Volmer equation cannot explain the

anodic branch behavior. According to Bultler-Vomer equation, the differential resistance should decrease under stronger bias (larger overpotential). Thus, we can say that charge transfer is not the rate limiting step.

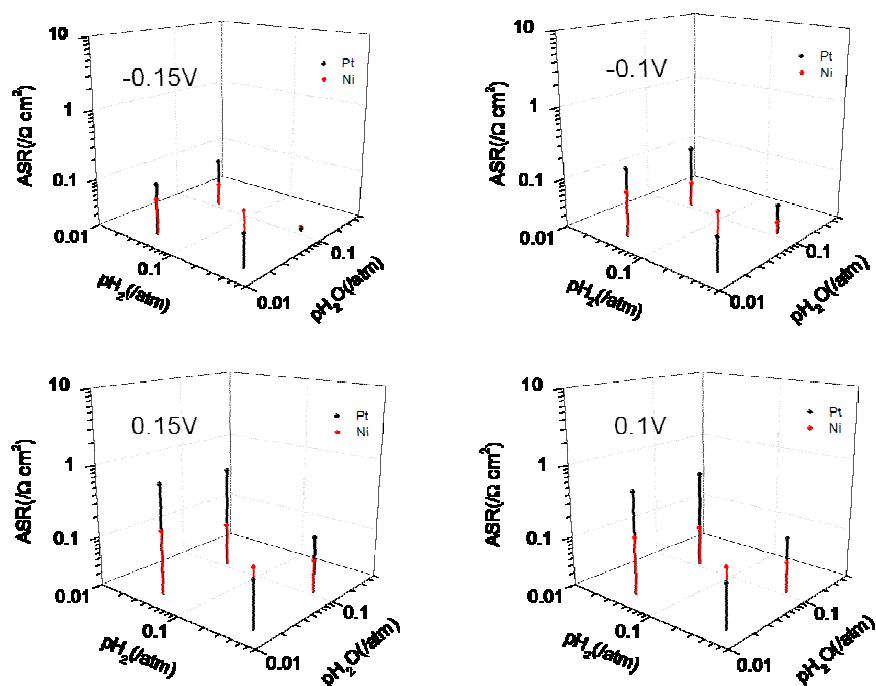


Figure 4.20 ASR comparisons of Ni (red) and Pt (black) under 4 biased conditions (-0.15V, -0.1V, 0.1V, 0.15V). Point anodes pressed on the surface of Sm doped ceria film. All scales are kept same for direct comparison.

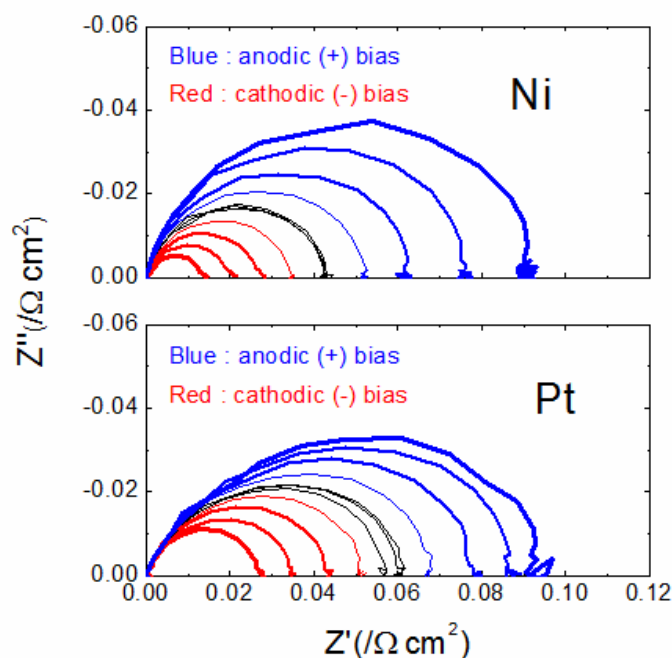


Figure 4.21 Impedance arcs superposed for various biases. Electrolyte contribution is subtracted off. Arcs are collected at 650°C with  $p_{H_2}=0.036$  atm and  $p_{H_2O}=0.121$  atm (-200 to 200mV, 50mV interval). Thicker line means stronger bias. Black line arcs: OCV condition.

Fig 4.21 shows two sets of arcs after normalization by Newman active area. The arc shape changes depending on the DC voltage load such that it becomes hard to apply simple circuit models. This arc deformation is found to be more severe for Ni point electrode; under cathodic bias, there emerges a shoulder at the low frequency side of the semi-circle. For both metals, the arc deformation on anodic bias suggests that in-plane electron migration becomes important [94]. Without fitting to an equivalent circuit, the electrode ASR is determined by the intercept to the real axis. This is shown in Fig. 4.22. Anodic bias increases ASR while cathodic bias decreases ASR.



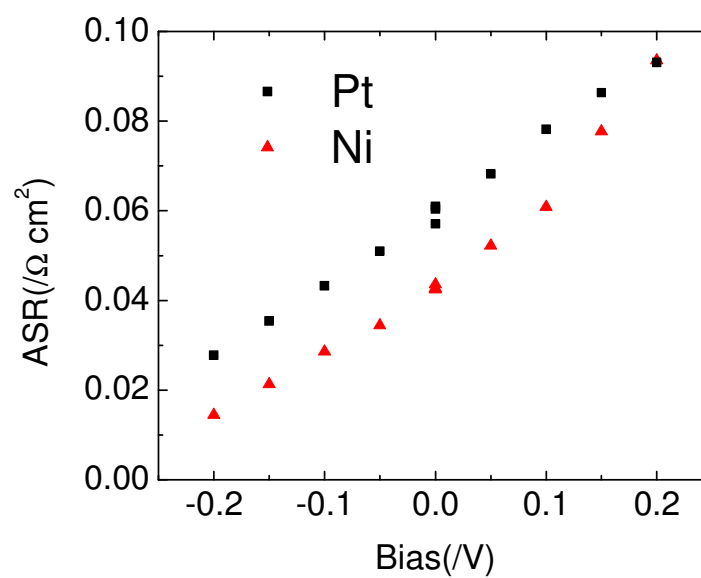


Figure 4.22 ASR behavior on biasing. ASR values are from arcs in Fig. 4.20.

## 4.6 Conclusion

With symmetric cell measurements, we looked into the doping level effect and preferred orientation effect. We found the following.

- (1) Gas reaction orders were generally between 0 and 1, and ASR monotonically decreases with increasing  $p\text{H}_2\text{O}$  or  $p\text{O}_2$ .
- (2) Sm doping level does not provide satisfactory correlation with electrochemical reaction kinetics.
- (3) The ASR gas reaction orders change with degree of film texturing, and more (100) aligned film shows better performance with gas dependence similar to that of Pt nanoparticle decorated PLD porous films.
- (4) Best performance (smallest ASR) is linked to strong water dependence and weak hydrogen dependence. With opposite gas reaction orders, the ASR is large.

With asymmetric cell measurements, three different metal point contacts are compared.

- (1) ASR shows metal dependence conflicting previous metal line pattern work [24].
- (2) Anode polarization behavior deviates from Butler-Volmer type charge transfer mechanism.

## Chapter 5

# Optical characterization

### 5.1 Summary

In this chapter, optical measurement results of the PLD grown doped/undoped ceria films and MOCVD grown undoped ceria films are described. Optical transmittance is measured as a function of light wavelength for films grown by two different fabrication methods: pulsed laser deposition and chemical vapor deposition. Pulsed laser deposition is chosen to represent a fabrication tool in physical vapor deposition category. By including films from two different fabrication processes, it is shown experimentally that developed transmittance fitting procedure can be applied no matter what fabrication is involved. The fitting procedure is made of two separate parts. In the first part, a reference film is analyzed to extract reference value of complex refractive index assuming Sellmeier dispersion relation. A film with full density and uniform thickness is required to carry out this process. Pulsed laser deposition can produce epitaxial films making this possible. We believe that we have measured the “true” refractive index of doped/undoped ceria films given the high quality of the films. Based on this reference refractive index data and effective medium models, it is possible to estimate the porosity of the thin film with unknown thickness. Porosity and thickness are fitting parameters. The results of the transmittance fitting are in good agreement of externally determined values of thickness and porosity. By analyzing refractive index dispersion against wavelength, it was found that ceria does not follow an empirically relation proposed for large class of materials.

## 5.2 Introduction

It is well known that ceria can serve as an oxygen storage material; however, it is only very recent years that a ceria-based thermochemical water splitting cycle is shown to be practical [92]. In this thermochemical scheme, solar radiation is the source of the heating for ceria catalyst. This necessitates studying light-matter interaction in the solar spectrum range (VIS-IR), and the fundamental materials property that governs this phenomenon is the complex refractive index. On the other hand, refractive index is related to the mass density of the material. For thin films, it is often not straightforward to determine the mass density. From refractive index measurement, it is possible to estimate mass density through effective medium theory. Here the optical dispersion behavior of undoped and 20 mol% Sm-doped ceria thin films, both dense and porous, were evaluated by UV-Vis optical transmission measurements, with the objective of determining both intrinsic and microstructural properties of the films. Films ranging from 14 to 2300 nm in thickness, were grown on single crystal YSZ(100) and MgO(100) using pulsed laser deposition (both dense and porous films) and chemical vapor deposition (porous films only). The transmittance spectra were analyzed using an in-house developed methodology combining full spectrum fitting and envelope treatment. The index of refraction of ceria was found to fall from 2.65 at a wavelength of 400 nm to 2.25 at 800 nm, typical of literature values, and was relatively unchanged by doping. Reliable determination on film thickness, porosity and roughness were possible for films with thickness ranging from 500 to 2500nm. Physically meaningful microstructural parameters can also be extracted even for films so thin as to show no interference fringes at all.

## 5.3 Experimental methods

### 5.3.1 Sample preparation

Ceria films were grown by both pulsed laser deposition (PLD) and chemical vapor deposition (CVD). PLD was carried out using a Nocera deposition system equipped with a coherent 102 KrF 248nm excimer laser, operated at a power density of about  $2\text{J}/\text{cm}^2$  and deposition frequency of 20Hz. Targets of either undoped or 20mol% Sm-doped ( $\text{Sm}_{0.2}\text{Ce}_{0.8}\text{O}_{1.9-\delta}$  or 20SDC) were fabricated in-house using commercial powders (undoped: Sigma Aldrich 202975, 99.995% pure; 20% doped: Fuel Cell Materials, 20SDC-HP, trace metal impurity  $\sim 160\text{ppm wt}$ ). To minimize the influence of the limited size of the laser plume on the uniformity of the films, the substrates were arranged at the center of the sample stage and rotated at a constant angular speed. The substrate was maintained a temperature of  $600^\circ\text{C}$ – $650^\circ\text{C}$  during deposition, and a cooling rate of  $10^\circ\text{C}/\text{min}$  was used prevent the films from cracking due to thermal expansion mismatch. Porosity in the deposited ceria film was varied by varying the background pressure of oxygen (5mTorr for dense films, 100mTorr for porous films [24]). Regardless of eventual film porosity, typical PLD growth rate was  $20\text{nm min}^{-1}$ . Film growth by CVD was carried out using an in-house constructed vertical cold-wall reactor, and compositions were limited to undoped ceria. The cerium precursor,  $\text{Ce}(\text{tmhd})_4$  (Strem, CAS : 18960-54-8, 99.9% cation purity), was used without further purification. The precursor was evaporated at a temperature of  $190^\circ\text{C}$ . The total system pressure during deposition was varied within a range of 1–3Torr and the substrate temperature held at between  $450$  to  $500^\circ\text{C}$ . The oxygen to argon flow ratio was kept at 1:2. The typical deposition rate was 15 to  $20\text{nm min}^{-1}$ .

Films were grown on 8mol%  $\text{Y}_2\text{O}_3$ -doped  $\text{ZrO}_2$  [YSZ(100)] and  $\text{MgO}(100)$  single-crystal substrates (MTI Corporation), polished on both sides ( $1\text{cm} \times 1\text{cm} \times 0.5\text{mm}$ ). The root mean square (rms) surface roughness of the as-received substrates, as measured in-house by atomic force microscopy (AFM), was below 0.5nm and the peak-to-valley roughness below 3.5nm. It is noted that  $n_{\text{YSZ}} > n_{\text{ceria}} > n_{\text{MgO}}$  and thus this choice of substrates enables assessment of the applicability of the methods to arbitrary substrate-film combinations.

### 5.3.2 Transmittance measurement

Fig 5.1 shows transmittance measurement setup.

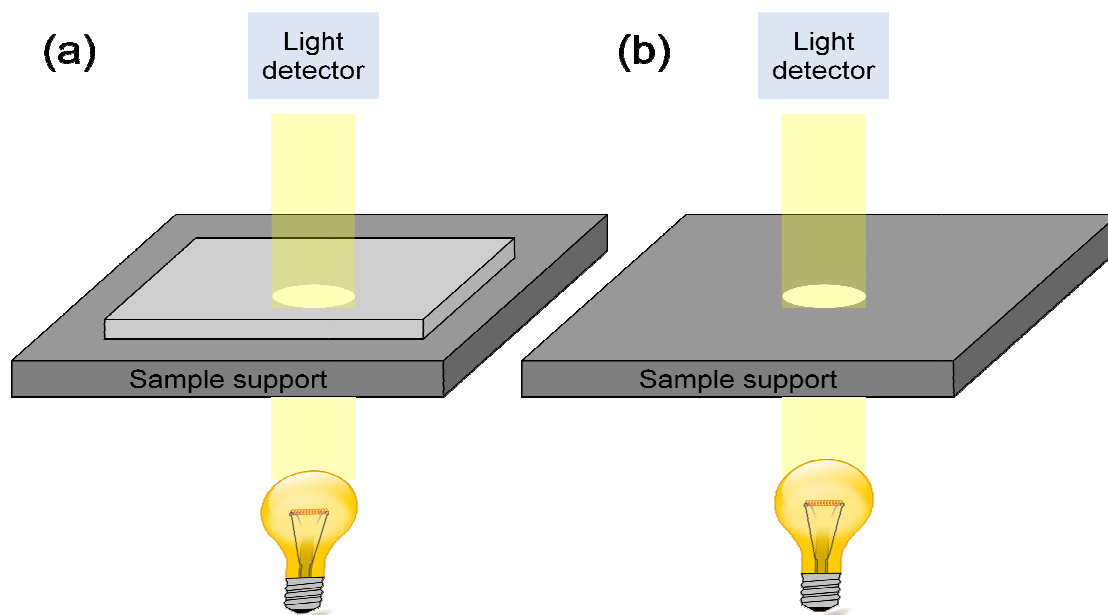


Figure 5.1 Transmittance measurement setup. (a) With sample in the optical path, one measures the sample transmittance. (b) Without sample in the optical path, one measures the baseline. ( $T=1$ ). One also measures the dark signal with a light block on the light detector (not shown) (Appendix B).

In all cases, transmittance measurement starts from establishment of the baseline as seen in Fig 5.1 (b). The experimental setup does not have double beam configuration, so one needs to collect the baseline first, and then put the sample in the optical path as in Fig 5.1 (a) without disturbing any other factor. The transmittance obtained in this way is that of the substrate/film composite. One could use the substrate itself as a reference ( $T$  set to 1 with only the substrate in the optical path), then measure the transmittance of the film only. Since the mathematical form is known in literature for substrate/film composite, we did not try this route. In this setup, sample support has an aperture that defines illuminated area. One can easily get a sense of thin film optical thickness (optical thickness =  $nd$ ,  $n$ : refractive index,  $d$ : physical thickness) in-plane uniformity by moving the sample (substrate + thin film) around the aperture or by changing aperture size.

Optical transmittance was measured using an Ocean optics HR2000CG-UV-NIR high-resolution, miniature, fiber-optic spectrometer, with a data collection range of 200 to 800 nm (beyond 800 nm the data were too noisy to be useful) and a 0.47 nm data point interval. The raw spectra for the wavelength range 400 to 800 nm were each converted to 500 equally spaced data points for analysis. No smoothing of any sort was applied. In all cases, when the sample was physically inverted such that the incident photons interacted with substrate first, there was essentially no change in transmittance trace. Transmittance spectra from blank substrates were also measured over the same wavelength range in order to obtain the substrate index of refraction as required for the analysis.

### 5.3.3 Auxiliary measurements

AFM roughness measurements were performed using a Park Systems XE-70 in noncontact mode. Occasional large particulates that formed on the PLD surface were avoided for the roughness measurement. These particulates were found to have negligible impact on measured transmittance spectra. Plane leveling and subsequent rms roughness estimation were carried out using the Gwyddion 2.25 software package. Film morphology was observed using a ZEISS 1550VP Field Emission Scanning Electron Microscope (SEM). Examination of fractured cross-sections of films provided an external and independent measure of film thickness. X-ray reflection curves to probe film roughness and density were collected using a Rigaku Smartlab diffractometer with  $0.01^\circ$  steps in  $2\theta$  up to  $5^\circ$  and data analyzed using the X'Pert Reflectivity software package. X-ray rocking curves were collected using an X'pert pro MRD system from Panalytical. A scanning white light interferometer (SWLI), Zygo NewView 600, was used to get surface maps for very thin films ( $<50\text{nm}$ ). The field of view was  $140\mu\text{m} \times 105\mu\text{m}$  for all cases.

## 5.4 Transmittance modeling

### 5.4.1 Ideal thin film and envelope method

Mathematical expression for transmittance of ideal thin film can be found in Appendix B (Eq. (B.3)). By ideal thin film, we mean that the film has uniform thickness (zero roughness) and uniform optical property. In reality, this is not necessarily true.

Eq. (B.3) describes an oscillating spectrum overlain on a transmittance that shows an overall increase with  $\lambda$ , where the spacing between maxima and minima is given by  $\phi$ .



The value of  $T$  at any given wavelength thus depends on three parameters, the real component of the index at that wavelength, the imaginary component (at that wavelength), and the film thickness; accordingly, the problem, at a single wavelength, is underdetermined. Swanepoel circumvented this challenge by introducing the envelope method [93]. The approach treats the overall characteristics of the transmittance function, rather than transmittance values at individual wavelengths, and takes advantage of the fact that the difference in transmittance at maxima and minima, interpolated to a given wavelength, depends only on  $n$  (and is independent of both  $d$  and  $k$ ). The transmittance values at the maxima define the upper envelope,  $T_U$ , and those at the minima, the lower envelope,  $T_L$ . Because  $T_U$  and  $T_L$  can be interpolated to arbitrary values of  $\lambda$ , the envelope method allows the index of refraction to be directly computed at any given  $\lambda$ , so long as  $T_U(\lambda)$  and  $T_L(\lambda)$  are appropriately established. With  $n(\lambda)$  known, the spacing between maxima and minima is then used to compute  $d$ . Finally, the extinction coefficient is determined after evaluating the absorbance from the separate expression (Maley [94]),

$$x = \{P + [P^2 + 2QT_\alpha(1 - R_2R_3)]^{1/2}\} / Q, \quad (5.1)$$

$$R_1 = [(1 - n)/(1 + n)]^2, \quad (5.1-1)$$

$$R_2 = [(n - s)/(n + s)]^2, \quad (5.1-2)$$

$$R_3 = [(s - 1)/(s + 1)]^2, \quad (5.1-3)$$

$$P = (R_1 - 1)(R_2 - 1)(R_3 - 1), \quad (5.1-4)$$

$$Q = 2T_\alpha(R_1R_2 + R_1R_3 - 2R_1R_2R_3), \quad (5.1-5)$$

$$T_\alpha = \sqrt{T_U T_L}. \quad (5.1-6)$$

The ultimate effectiveness relies on accurate positioning of the envelope values and identification of the order number of the interference fringes.

#### 5.4.2 Transmittance of rough films

As recognized by Swanepoel [95], roughness on the film surface has the effect of “softening” the interference fringes in the transmittance spectrum such that  $T_U$  and  $T_L$  approach each other, but without modification to the wavelength dependence of the position of the extrema. Treatment of the problem requires a physical model of the manner in which the thickness varies. Here, each film is considered to display a mean thickness and a Gaussian distribution of thicknesses about this mean. Numerical implementation is achieved by dividing the film into 5000 equal-footprint vertical columns with heights reflecting the Gaussian distribution. In the Matlab code, this is realized by producing 5000 random numbers with Gaussian distribution around zero ( $\sigma=1$ ), and then multiplying them with roughness  $r$ . One thickness value,  $d$ , is then added to these 5000 random numbers to give 5000 different column heights. This is just pseudorandom, not truly random since they are generated by an algorithm built in Matlab. Nevertheless, this should serve our goal to simulate surface roughness of a film. The transmittance is then computed assuming a spatial average over the transmittances through each column,  $T_j$ , given by

$$T = \frac{1}{5000} \sum_{j=1}^{5000} T_j(d_j) \quad (5.2)$$

This standard deviation corresponds to the root-mean-square roughness measured directly by AFM. In this approach, it should be also noted that the film-substrate interface roughness is neglected. All contribution from roughness is attributed to film-air interface

roughness. For dense epitaxial films, this is easy to justify. For porous films, this is not straightforward. However, by transmittance fitting, it is impossible to distinguish the two contributions. Thus, we simply put all the contribution to surface roughness.

#### 5.4.3 Transmittance of porous films

Porosity in the film has the effect of lowering the effective index of refraction by rendering it an average, in some way, of the bulk properties of the film material ( $>1$ ) and of air ( $\sim 1$ ). Following the general approach of effective medium theory, here, the microstructure-specific optical properties of the porous material or two-phase composite (of the solid and air) are replaced with those of a hypothetical dense film with equivalent properties. Effective medium models are introduced in Appendix C.

Fig. 5.2 illustrates the sensitivity of predicted behavior of refractive index to the choice of model. In fact, the  $n_{eff}(\lambda)$  computed for the three different models at two different representative porosity levels (assuming realistic  $n$  for the oxide), shows that the two Bruggeman approaches, symmetric Bruggeman (S-BG) and asymmetric Bruggeman (A-BG), yield almost indistinguishable results. In contrast, the LLL model implies an  $n_{eff}(\lambda)$  that is quite distinct from the Bruggeman behavior. Accordingly, analysis of porous films was carried out using only the S-BG and LLL models.

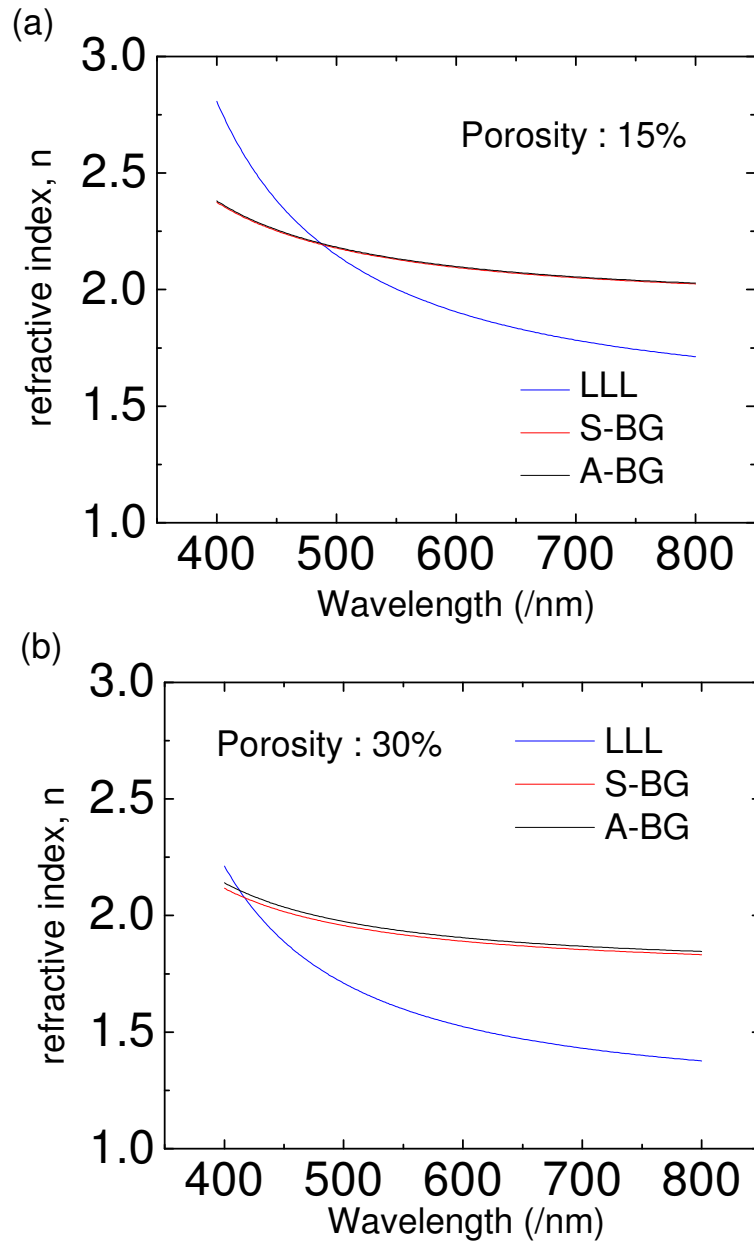


Figure 5.2 Simulated dispersion behavior of refractive index (real part) for different effective medium models. (a) assumed porosity: 15%, (b) assumed porosity: 30%. The two BG models are indistinguishable in terms of dispersion behavior.

#### 5.4.4 Sellmeier dispersion and reference refractive index determination

Swanepoel overcame the underdetermined problem by envelope method. Alternatively, if one has knowledge of the functional forms of  $n(\lambda)$  and  $k(\lambda)$ , then one could adjust the parameters of those functions so as to fit a spectrum, calculated according to Eq. (1.20), to the measured spectrum. Such an approach would utilize the full set  $\{T_i\}$  to determine a limited set of parameters, eliminating the situation of an underdetermined problem. The behavior of  $n(\lambda)$  for transparent materials has been treated and is discussed in greater detail below. The behavior of  $k(\lambda)$  can ideally be obtained from  $n(\lambda)$  utilizing the Kramers-Kronig relation. Because the wavelength range of the measurement is finite, however, the treatment is not entirely straightforward. Bhattacharya et al. applied such an envelope-free approach to the study of films of  $\text{Zn}_{1-x}\text{Mg}_x\text{O}$  with good success, but could do so only upon dividing the spectra into arbitrary regions [96].

In the present work we employed a strategy that combines aspects of full spectrum fitting and envelope treatment. This strategy is for the reference complex refractive index determination. The index of refraction,  $n(\lambda)$ , is assumed to behave according to the Sellmeier equation;

$$\frac{1}{n^2 - 1} = -\frac{A}{\lambda^2} + B. \quad (5.3)$$

This is an expression that has been found to accurately represent the behaviors of a large number of transparent materials (Shannon [97]). In this view, a material is regarded as a collection of atoms whose electron clouds are displaced from its equilibrium position by the oscillating electrical fields of the light. This electron motion is described by Abraham-Lorentz equation. As the dispersion characteristics arise from the interaction of light with

the bonding electrons, the A and B constants suitably parameterize the behavior for subsequent analysis. For those measurements in which the objective is to determine optical properties rather than microstructural features, starting estimates of A and B are employed to provide initial estimates of  $n$  through Eq. (5.3) and of  $k$  through Eq. (5.1), where the latter relies on determination of the envelope values  $T_U(\lambda)$  and  $T_L(\lambda)$ . In other words, we utilized envelope method to get  $k$  from  $n$  rather than complicated Kramers-Kronig relation. Full spectrum fitting is performed by computing and minimizing the error,  $\chi^2$ , defined as

$$\chi^2 = \sum_1^N \frac{1}{\sigma_i^2} (T_i^{calc} - T_i^{meas})^2, \quad (5.4)$$

where  $T$  is that given in Eq. (1.20),  $N$  is the number of points in the calculation ( $= 500$ ), and  $\sigma_i$  is the experimental uncertainty in each transmittance point. The latter is taken to be 0.01 over the entire wavelength range of interest based on the transmittance measured from an empty cell ( $T = 1$ ). In the procedure described so far, the search for reference (“true,” or “bulk,” or “full-density”) complex refractive index becomes a search for A/B pair that minimizes  $\chi^2$ . For this search, all other micro structural factors are externally determined and fed to Eq. (1.20). This process is called “dispersion fit” in the following sections.

#### 5.4.5 Fit parameter uncertainties

The statistical uncertainty in the parameters,  $\delta x_j$  (where  $\{x_j\}$  is the set of fit variables), was estimated by evaluating the expression

$$\delta x_j = \left[ \left( \frac{\partial T}{\partial x_j} \right) \bigg|_{\{x_{i \neq j}\}} \right]^{-1} \delta T, \quad (5.5)$$

with  $\delta T$  being equivalent to the experimental uncertainty, estimated above as 0.01 from the noise level. This is the maximum possible error on the each parameter of interest. The total uncertainty should have contributions from multiple fit parameters (error propagation). All calculations were performed using in-house written MATLAB codes.

## 5.5 Results and discussion

### 5.5.1 Optical parameter

A summary of the film-substrate systems prepared and examined in this work are provided in Table 5.1. The first set of samples are three thick ( $\sim 2\mu\text{m}$ ), dense films of two different composition prepared by pulsed laser deposition and applied to two different types of substrates. With these films we determine the material properties to a high degree of accuracy, evaluate their variation with stoichiometry, and determine the influence, if any, of the substrate on the transmission analysis. The second set of samples constitute three thinner films (500~700nm) grown under various conditions so as to yield microstructural differences. Analysis is carried out using fixed values of  $n(\lambda)$  and  $k(\lambda)$  obtained from the evaluation of the dense films. The final set of samples are a pair of extremely thin films for which the envelop method is entirely unsuitable. It is shown that, despite the absence of interference fringes, meaningful microstructural data can be obtained.

Fig 5.3 shows the SEM cross-sectional and AFM topological images of two dense ceria films (films 1 and 2, obtained by PLD) of differing stoichiometries grown on YSZ(100) with (SEM determined) thicknesses of 1820 and 1900nm for dopant

concentrations of 0 and 0.20, respectively. The films have negligible porosity and the rms roughnesses are, respectively, 2.5 and 2nm. As described elsewhere, such PLD films adopt an epitaxial relationship with the YSZ substrate and are stoichiometrically identical to the target material [24]. The transmittance spectra obtained for these films are shown in Fig 5.4, along with the results of two fits. Because the films are thick and relatively smooth, the spectra show a large number of sharp interference fringes in the wavelength range of the measurement. Such films are amenable to treatment by a traditional envelope method just as they are to the full spectrum fitting undertaken in this work. Here, the inherent dispersion properties for the two compositions were determined by fixing rms roughness and film thickness at the independently, experimentally determined values just quoted, setting porosity to zero, and performing least squares fitting with only A and B as varied parameters. The resulting fits are shown in red in the plots in Fig 5.4 (“dispersion fit”).

Table 5.1 Summary of ceria film characteristics ( <sup>a</sup> ~ 2μm, <sup>b</sup> 500 – 1000nm, <sup>c</sup> < 50nm)

Film #	Deposition method	Composition	Substrate	Thickness	Film density
1	PLD	undoped	YSZ(100)	thick <sup>a</sup>	dense
2	PLD	20SDC	YSZ(100)	thick <sup>a</sup>	dense
3	PLD	undoped	MgO(100)	thick <sup>a</sup>	dense
4	CVD	undoped	YSZ(100)	moderate <sup>b</sup>	porous
5	PLD	20SDC	YSZ(100)	moderate <sup>b</sup>	porous
6	PLD	20SDC	YSZ(100)	moderate <sup>b</sup>	porous
7	CVD	undoped	MgO(100)	thin <sup>c</sup>	porous
8	CVD	undoped	YSZ(100)	thin <sup>c</sup>	dense



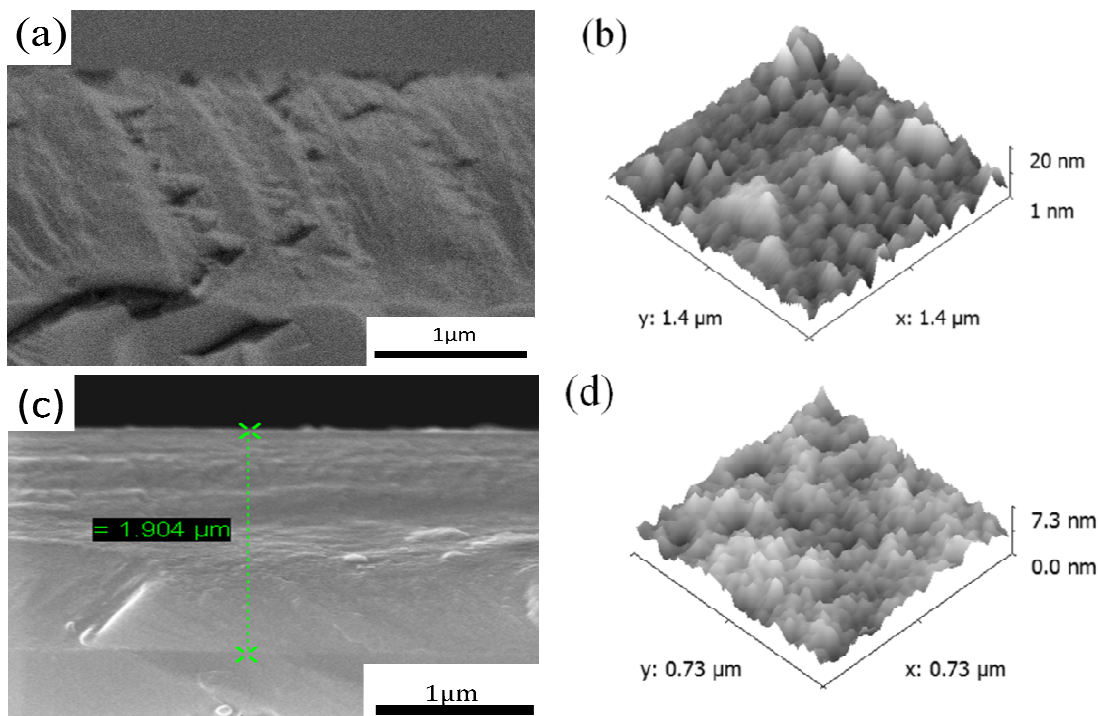


Figure 5.3 Microstructural images of dense PLD films on YSZ (100): (a) SEM cross-sectional and (b) AFM topological images of undoped ceria (Film #1); and (c, d) analogous images for 20SDC (Film #2).

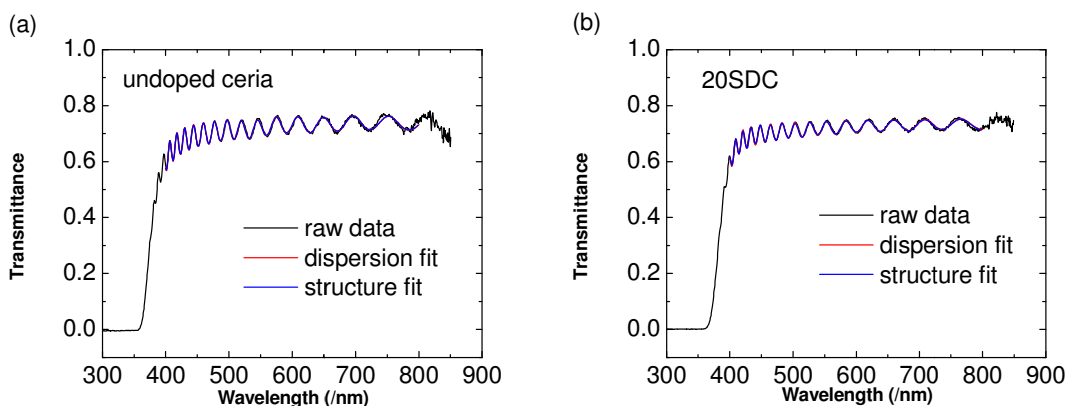


Figure 5.4 Transmittance measurement and analysis for dense PLD films (a) undoped ceria (Film #1); (b) 20SDC (Film #2), of comparable thicknesses. Dispersion fits obtained upon varying A, B parameters in the Sellmeier dispersion relation, Eq. (5.3), with thickness and roughness fixed. Structure fits obtained upon varying porosity, thickness, and roughness, with known dispersion relationship from dispersion fits.

The dispersion behavior implied for undoped and 20% Sm-doped ceria is summarized in Fig 5.5, where Fig. 5.5(a) compares the present results for undoped ceria with literature values [47-52], and 5(b) compares the three films studied here to one another. The index of refraction of undoped ceria obtained in this study is in general agreement with the many literature reports on this material. In all cases, the long-wavelength index falls between 2.1 and 2.4, and an upturn occurs around 400 nm as the photon energy approaches the average oscillator energy. As shown in Fig. 5.5(b), despite a difference in substrate, the results from the two undoped ceria films are almost identical in this film thickness range, suggesting that artifacts arising from differences in substrate are negligible. The slightly lower index for CeO<sub>2</sub> on MgO (film 3) relative to that on YSZ (film 1) may be due to lattice mismatch in the former case, which can, in turn, generate defects that lower material density. The index of refraction of the Sm-doped film is slightly lower still than either of the two doped films, but the impact of doping is small.

Turning to the literature, only one prior study of the optical properties of Sm-doped ceria, which specifically focuses on the 15% Sm composition, could be found [98]. Those authors reported that the doped composition had a slightly higher index than the undoped (in contrast to the present work), but for both doped and undoped compositions the reported index was unusually low, below 2 over 400~800nm. The low index of refraction suggests that porosity in the sol-gel derived films of that study, though not reported, was not negligible, and thus trends with composition cannot be established from those results. The present study, comparing films 1 and 2 (both with 100% density), suggest a lowering of  $n$  by 0.03 at all wavelengths upon introduction of 20% Sm. Because Sm<sup>3+</sup> ion has a higher dielectric polarizability than Ce<sup>4+</sup>, an increase in  $n$  could be expected [99]. On the other

hand, because the fluorite lattice expands upon doping, the opposite would be expected.

The competition between these two characteristics prevents a straightforward prediction.

The experimental results suggest the latter effect is slightly more significant.

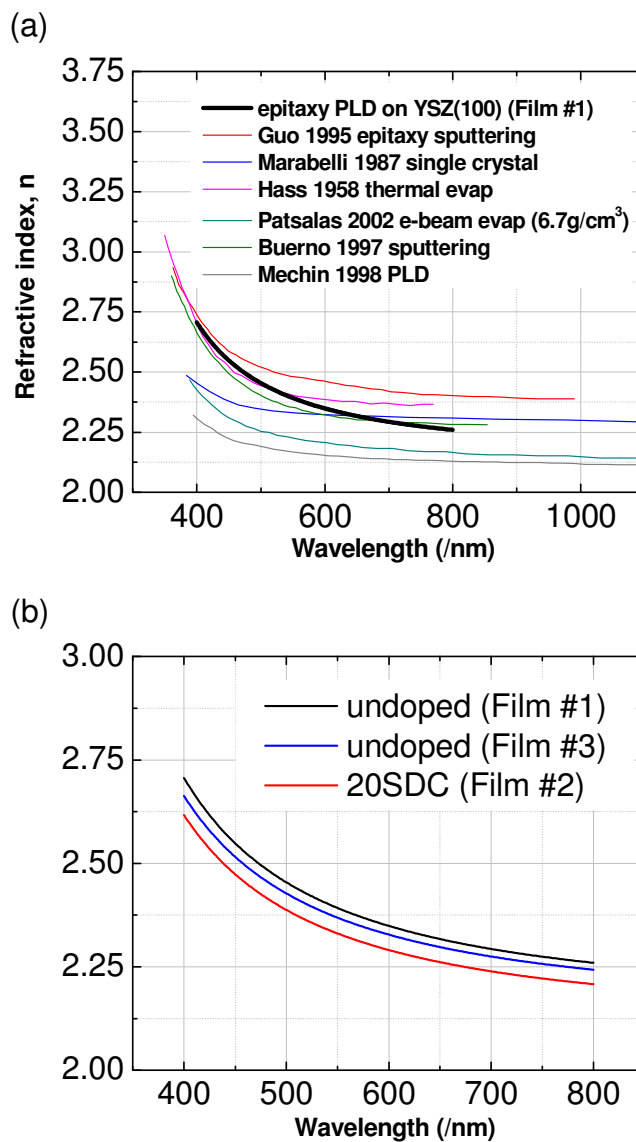


Figure 5.5 Derived dispersion behavior of PLD grown films: (a) undoped ceria (Film #1) compared to literature results [47-52]; (b) substrate and dopant effects. Deposition on MgO(100) (Film #3) leads to a slight decrease in  $n$  relative to deposition on YSZ(100) (Film #1), likely due to poorer crystallographic registry between film and substrate creating a slightly lower density. Sm doping leads to a marginal decrease in  $n$  by 2%~3% over the wavelength range of interest, indicating minimal impact on the electronic characteristics.

The dispersion behavior can be interpreted in terms of the electronic properties of the solid. Specifically, the optical band gap,  $E_g$ , is related to the absorption coefficient (Eq. (1.20)) accordingly to the expression [47, 50, and 52]

$$\alpha E_{ph} \propto (E_{ph} - E_g)^\eta, \quad (5.6)$$

where  $E_{ph}$  is the photon energy (given by  $E_{ph} = hc/\lambda$ , where  $h$  is Planck's constant and  $c$  is the speed of light) and  $\eta$  is a constant of value 0.5 for a direct transition and 2 for an indirect one. This expression was used here only for the determination of the indirect band gap ( $E_g^{\text{indirect}}$ ), which is smaller than  $\sim 3.5\text{eV}$  in ceria, because transmittance data in the range below  $\sim 350\text{nm}$  display too much scatter for analysis of the higher energy, direct band gap.

An alternative method for interpretation of the dispersion behavior is provided by Wemple and DiDomenico [100]. These authors have shown that the Sellmeier expression is expected for a material in which the electronic excitations are described in terms of a single oscillator approximation. The index, in this approximation, depends on the  $E_O$  (average oscillator energy) and  $E_d$  (dispersion energy, which describes the dispersion of the refractive index) according to

$$n^2 = 1 + \frac{E_O E_d}{E_O^2 - (E_{ph})^2}. \quad (5.7)$$

Comparison to Eq. (5.3) immediately yields

$$\begin{aligned} E_O &= hc \sqrt{\frac{B}{A}}, \\ E_d &= \frac{hc}{\sqrt{AB}}. \end{aligned} \quad (5.8)$$

Wemple and DiDomenico further observed an empirical relationship between  $E_d$  and atomic bonding structure:

$$\beta = \frac{E_d}{N_c Z_a N_e}, \quad (5.9)$$

where  $N_c$  is the cation coordination number,  $Z_a$  the formal anion valency,  $N_e$  the effective number of valence electrons per anion, and  $\beta$  is an empirical parameter, found to be a constant depending on the nature of the type of bond:  $\beta_{\text{ionic}} = 0.26 \pm 0.04\text{eV}$ ,  $\beta_{\text{covalent}} = 0.37 \pm 0.05\text{eV}$ . This relationship permits an a priori estimate of the dispersion energy. In addition, the lowest direct band gap energy,  $E_g^{\text{direct}}$ , is empirically related to the oscillator energy according to

$$E_g^{\text{direct}} \approx \frac{2}{3} E_o. \quad (5.10)$$

The derived values for these various terms are summarized in Table 5.2, The indirect band-gap energy obtained directly from Eq. (5.6) for undoped ceria, 3.23eV, falls within the range of values reported in the literature [47, 49-52]. Introduction of Sm has almost no impact on this band energy (the decrease to 3.15eV is too slight to be considered significant), implying that the rare-earth dopant has negligible impact on the band structure.

Table 5.2 Dispersion relation fit parameters and Wemple-DiDomenico energy terms obtained for dense PLD films on YSZ(100). Statistical errors ( $<0.1\%$ ) are too small to reflect the true uncertainty and values are simply reported to three significant digits.

Film	A (/nm <sup>2</sup> )	B (unitless)	$E_g^{\text{indirect}}$ (/eV) Eq. (5.6)	$E_d$ (/eV) Eq. (5.8)	$E_o$ (/eV)	$E_g^{\text{direct}}$ (/eV) Eq. (5.10)
#1, ceria	18200	0.272	3.23	17.6	4.79	3.19
#2, 20SDC	18600	0.287	3.15	17.0	4.88	3.25

Analysis based on the Wemple and DiDomenico approach (Eq. (5.8)), leads to energy terms,  $E_d$  and  $E_o$ , that are small relative to typical oxide values. Specifically,  $E_d$  for undoped ceria is determined to be 17.6eV, whereas Wemple and DiDomenico report a range of values spanning from 17 to 28eV [100]. Similarly,  $E_o$  here is 4.79, as compared to the reported range of 5 to 14eV. As the latter correlates directly to the band gap, one could interpret the small  $E_o$  to result simply from an intrinsically small  $E_g^{\text{direct}}$ . However, from the accepted value of the direct band gap energy of ceria, ~3.7eV [101], the expected value of  $E_o$  is ~5.6eV, somewhat higher than obtained. It is further noteworthy that the value of  $\beta$  derived from the present analysis is also small, only ~0.14eV (taking, for the fluorite structure,  $N_C = 8$ ,  $Z_a = 2$ , and  $N_e = 8$ ).

This set of slight discrepancies between the derived and expected energy values could plausibly be explained as an artifact of an inaccurate and too large value of  $A$  (Eq. (5.8)). However, attempts to fit the transmittance data using smaller  $A$  yielded poor agreement with the experimental data, and such an explanation is deemed unlikely.

Accordingly, we conclude that the correlations suggested by Wemple and DiDomenico simply do not apply to ceria. We believe this discrepancy should arise from the fact that the nominal  $O2p \rightarrow Ce4f$  transition, which is forbidden by angular momentum selection rule, has strong  $Ce4d \rightarrow Ce4f$  character [101]. Marabelli [102] denotes that only half of the 48 p band electrons per unit cell have this d character. This consideration lowers  $N_e$  value to 4, which gives better agreement to typical  $\beta_{ionic}$ . Despite the unexpected energy terms, the substantial thickness, full density, and well-controlled microstructure of our dense PLD films permits us to conclude that the dispersion behavior obtained here, Fig. 5.5(a), accurately describes the intrinsic, bulk optical properties of ceria.

### 5.5.2 Microstructural parameter

#### - Dense films

With the index of the ceria compositions well characterized, an initial validation of the fitting procedure was carried out using the data from the three dense films. The varied parameters were density, roughness and film thickness. In this case, because both  $k$  and  $n$  are taken as known input parameters, there is no need to make use of the envelop method for any of the calculations, and only minimization of  $\chi^2$  in Eq. (5.4) was implemented. Table 5.3 summarizes the fitting results, and the computed  $T$  values for this case are shown in Fig 5.4 as the blue curves (“structure fit”). The parameters obtained from the fitting are in good agreement with the independently measured values, providing a validation of the procedures.

Table 5.3 Comparison between measured and fit microstructural parameters for dense, flat, thick ceria PLD films in Fig. 5.3, obtained using index of refraction values shown in Fig. 5.4. In all cases, fitted value of film porosity was below 0.01.

Film #	Composition	Thickness Fit/SEM (nm)	Film density Fit/set (relative)	rms Roughness Fit/AFM (nm)	$\chi^2$
1	undoped	1822 / 1820	>0.99 / 1	4 / 2.5	210
2	20SDC	1900 / 1900	>0.99 / 1	5 / 2	112
3	undoped	2300 / 2300	>0.99 / 1	10 / 13	762

- Arbitrary typical films

Films 4 – 6 are representative of typical deposition conditions. Film 4 is a CVD-derived film of undoped ceria (growth temperature: 500 °C; deposition pressure: 1 Torr); films 5 and 6 are PLD-derived films of 20SDC deposited under 100 mTorr oxygen pressure, which, as already indicated, generates high porosity. The two PLD films differ only in terms of growth time (22K and 30K shots, respectively), leading to films of differing thickness. For all three analyses the  $n(\lambda)$  and  $k(\lambda)$  were taken from the results of the dense films and only microstructural parameters were varied. Because the films are less than 1  $\mu\text{m}$  in thickness, as detailed below, only a limited number of interference fringes occur (Figures 5.6 and 5.7), and the fitting results were not particularly sensitive to film roughness (reflected in how sharp the interference fringes are). Accordingly, only thickness and porosity were evaluated with roughness set to zero. Both the S-BG and LLL models for treating the porosity were considered. The limited number of fringes also implies that analysis by an envelope method alone would lead to high errors. Indeed, a comparative evaluation by the latter was found to severely underestimate the porosity (by 25% to 40%).



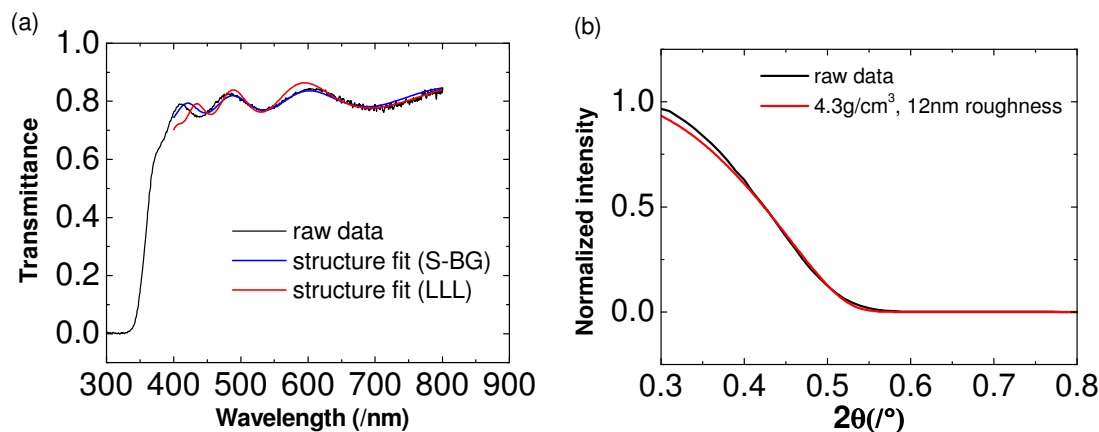


Figure 5.6 Properties of porous, undoped ceria deposited on YSZ(100) by CVD (Film #4): (a) Measured and modeled transmittance spectra, where fits were performed by varying microstructural parameters within the framework of the S-BG and LLL effective medium models; and (b) measured and simulated X-ray reflectometry curves, where the simulation was performed for a film of manually optimized porosity of 40% ( $4.3 \text{ g/cm}^3$  is 60% of the theoretical value of  $7.22 \text{ g/cm}^3$ ) and rms roughness of 12 nm.

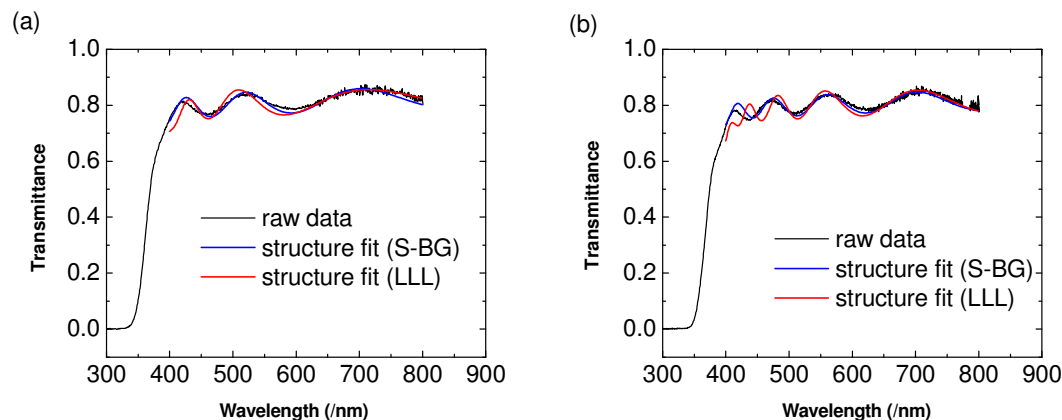


Figure 5.7 Transmittance measurement and analysis for porous PLD films of undoped ceria of differing thicknesses: (a) 22K shots (Film #5), and (b) 30K shots (Film #6). Fits were performed by varying microstructural parameters within the framework of the S-BG and LLL effective medium models.

The fitting results for these three films are presented in Fig 5.6(a), 7(a) and (b), where the measured data are in black, the fits for the S-BG model are in blue, and the fits for the LLL model are in red. The results clearly demonstrate that the transmittance behavior is much better captured by the S-BG model. Though not shown, for completeness,

the A-BG model was also explored and, not surprisingly, the result was barely distinguishable from the S-BG model for all three films. The extracted microstructural parameters are summarized in Table 5.4. For all three films the  $\chi^2$  values, also provided in the table, are significantly smaller for the S-BG model than the LLL model, consistent with the visual differences evident in relevant figures indicating that the former provides a better representation of the film microstructures. In the case of Film 4, for which XRR analysis was performed, the porosity value of  $0.397 \pm 0.13$  determined from the S-BG fit matches quite well to the XRR value of 0.4, and is closer to this XRR porosity than the LLL model value of  $0.367 \pm 0.001$ . Similarly, in the case of Film 6, for which SEM imaging was performed, the thickness value of  $717 \pm 29$  nm determined from the S-BG fit matches quite well to the directly measured value of 740 nm, and is closer than the value of  $649 \pm 33$  determined from the LLL model. The computed thickness of Film 5 using the S-BG model is  $532 \pm 67$ , almost precisely consistent with the 35% shorter growth time for this film relative to Film 6. Although roughness was not evaluated from the transmittance data, it is noteworthy that the XRR measurement yielded a root-mean-square roughness of 12 nm for Film 4 (Fig. 5.6(b)), comparable to the value of 10 nm obtained from an AFM measurement of this same film.

While a detailed discussion of film growth characteristics is beyond the scope this work, the two porous PLD-grown films [20SDC on YSZ(100)] reveal interesting behavior. Despite the identical growth conditions, the computed porosities differ, determined as 0.45 and 0.40, respectively, for Films 5 and 6. This result is taken to represent the actual film growth characteristics. It has been observed that with increasing film thickness, the

individual columns of the columnar structure increase in diameter, whereas the number density of columns decreases [103]. This overall coarsening of the structure apparently causes an increase in overall film density with increasing film thickness. Although the model for transmittance employed here does not account for graded porosity, the variation observed here, just 10% over a thickness corresponding to 35% of the total, is sufficiently small that it does not have significant impact, for example, on the accuracy of the derived film thickness.

Table 5.4 Summary of microstructural fit parameters obtained from transmittance spectra analysis of Films 4-6. Results obtained from S-BG and LLL effective medium theories are compared, and where available, these are also compared to independent structural measurements.

Film #	method	Thickness(/nm)	Porosity	$\chi^2$
4 <sup>a</sup>	S-BG	589 ± 63	0.397 ± 0.13	672
	LLL	507 ± 36	0.367 ± 0.001	1964
	XRR	--	0.4	--
5	S-BG	532 ± 69	0.453 ± 0.073	687
	LLL	420 ± 41	0.364 ± 0.001	1610
6	S-BG	717 ± 29	0.404 ± 0.093	669
	LLL	649 ± 33	0.333 ± 0.001	2270
	SEM	740 ± 30	--	--

<sup>a</sup> rms roughness by AFM = 10 nm, by XRR = 12 nm

- Very thin films (<50nm)

Films 7 and 8 (Table 5.1) are very thin samples representing the initial conditions of CVD films growth. The deposition was carried out for only ~10 seconds on two different substrates: MgO(100) and YSZ(100). These films were grown simultaneously in a single deposition run (growth temperature: 450 °C; deposition pressure: 3 Torr) so as to insure a meaningful interpretation of substrate influence. Given the good lattice match between ceria and YSZ, whereas that between ceria and MgO is poor, one can anticipate a difference in growth characteristics, particularly at the initial stages. The spectra, Fig 5.8, are almost featureless as a result of the extreme thinness of the films, entirely precluding an analysis by the envelope method. Using the full spectrum fitting approach and the S-BG model for porosity, we extract film thickness and porosity for both samples as reported in Table 5.5. The raw data are shown in black and the fits in red. As with the earlier films, the data are well represented. The porosity in the case of deposition on MgO is 0.4, whereas on YSZ it is negligible. As a measure of the sensitivity of the numerical procedures, simulated spectra assuming a porosity of 0.2 are shown (blue curves) on both plots. The simulation confirms that a porosity of 0.2 underestimates the transmittance through the more porous film on MgO and overestimates that through the denser film on YSZ. Thus, it is apparent that the substrate indeed has a profound influence on film growth characteristics.

To confirm the validity of the transmittance fitting results, we utilize two different additional experimental tools, namely XRR and SWLI. Fig 5.9 shows an experimental reflection data and simulated curves. In a very general sense, the frequency of the oscillations in the XRR spectrum reflects the film thickness and the sharpness and position of the first drop-off reflect a convolution of roughness and density. It is apparent that

precise determination of the physical parameters from these data is a major challenge.

Nevertheless, one can conclude from the left-side plot that the spectrum is consistent with a film that is 10~20nm in thickness, and from the right-side plot with one that has a density of approximately 85%. These values are, in turn, consistent with the values of thickness and density,  $14 \pm 10\text{nm}$  and  $100 \pm 21\%$ , respectively, obtained from the analysis of the optical transmittance data.

SWLI measurements are done for a set of simultaneous grown films, one on MgO(100) and another on YSZ(100). The deposition time is again kept at 10 seconds. The results are shown in Fig 5.10. In all cases shown, root-mean-square roughness turns out to be 0nm in spite of obvious difference on the surface morphology between MgO(100) and YSZ(100) cases. On MgO(100) bare surface, there are embossed line-shape features meeting at  $90^\circ$ . This irregularity of the bare MgO(100) surface is preserved over the thin film growth whereas there is no such irregularity for YSZ(100), and this difference is correctly detected. In table 5.5, the irregularity manifests itself as porosity.

This substrate effect in the early stage of growth is additionally reflected in the X-ray rocking curve pattern about the ceria 200 peak, Fig 5.11, which shows a sharp peak only when the substrate is YSZ.

Table 5.5 Summary of fitting results from Films #7 and #8. Larger  $\chi^2$  for Film #8 is mainly from the higher level of noise in the spectrum (Fig. 5.9)

Film #	Substrate	Thickness(/nm)	Porosity	$\chi^2$
7	MgO(100)	$30 \pm 80$	$0.40 \pm 0.10$	184
8	YSZ(100)	$14 \pm 10$	$0.00 \pm 0.21$	415

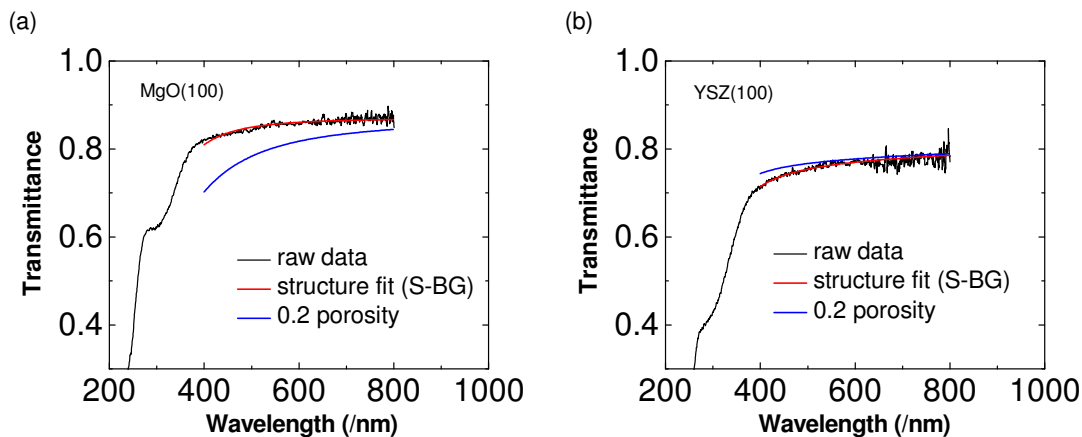


Figure 5.8 Transmittance measurement and analysis for ultra-thin CVD films of undoped ceria on differing substrates: (a) on MgO(100) (Film #7), and (b) on YSZ(100) (Film #8). Fits were performed by varying microstructural parameters within the framework of the S-BG, varying thickness and porosity (red lines). Blue lines are simulated transmittance curves, generated assuming 0.2 porosity and the thickness as obtained from the initial respective fits.

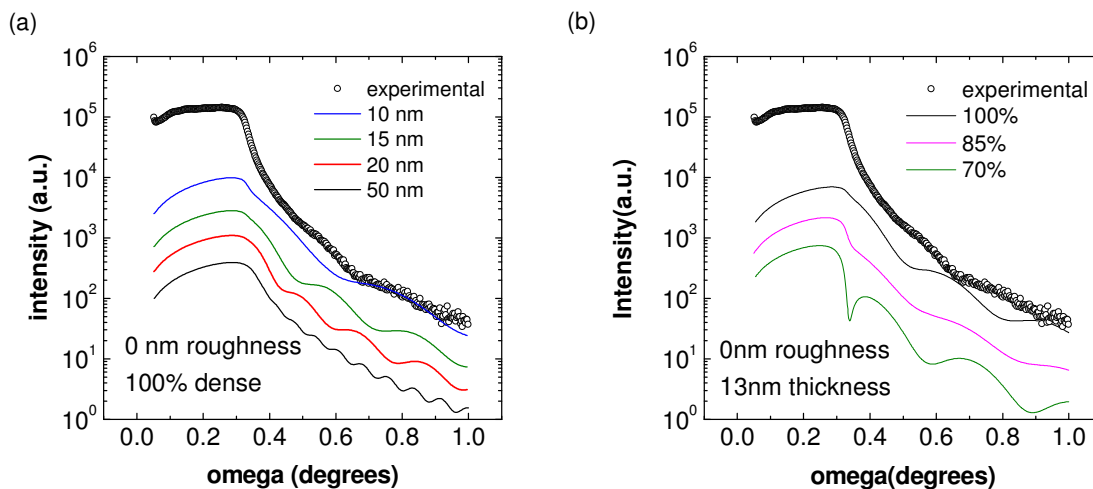


Figure 5.9 XRR trace for a film comparable to film #8 (same deposition condition). Experimental data compared to simulations with parameters as given on the plots. Simulated curves are from (a) thickness variation, (b) density variation.

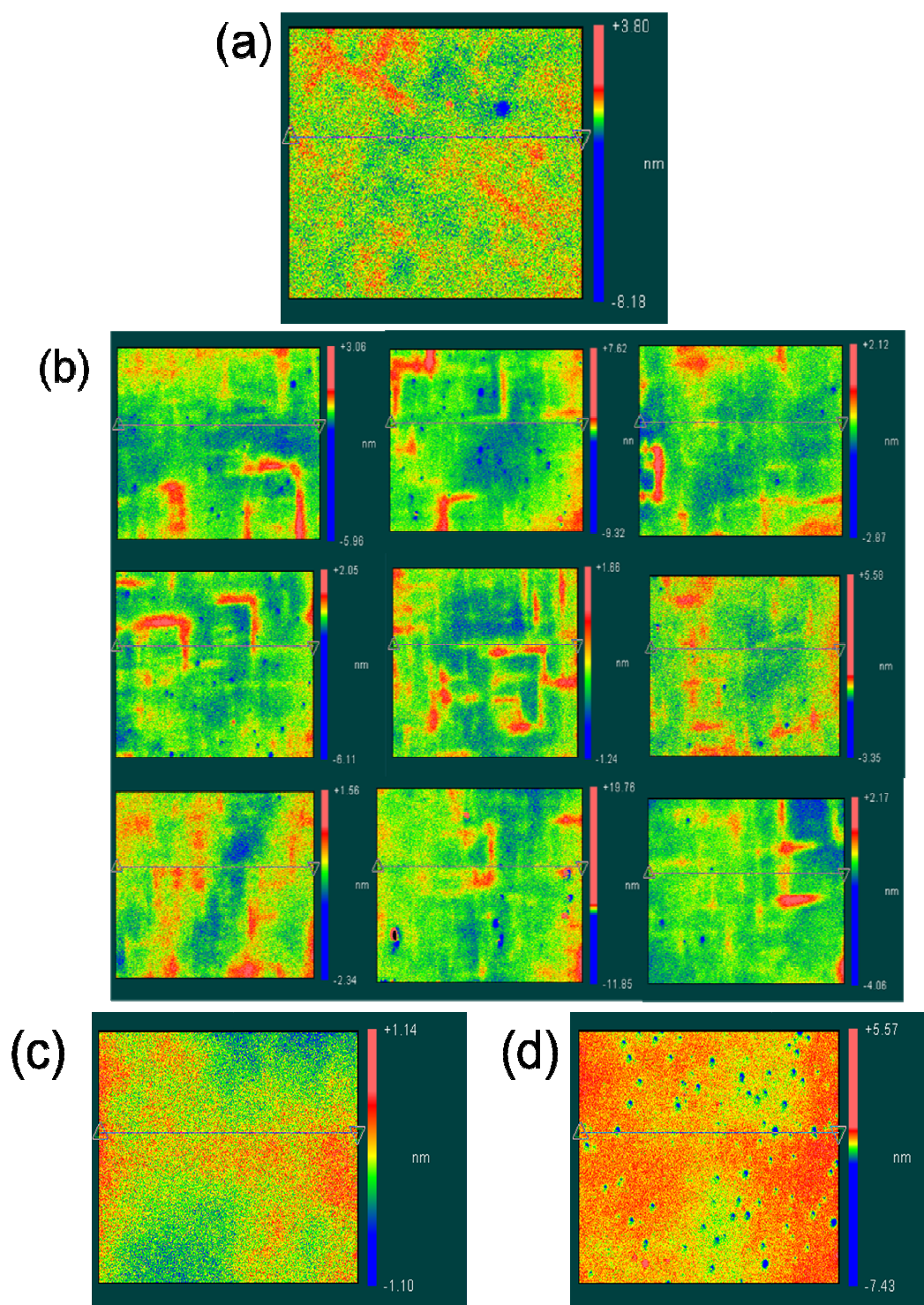


Figure 5.10 Surface maps. MgO(100) substrate; (a) before deposition, (b) after deposition. YSZ(100) substrate; (c) before deposition, (d) after deposition.

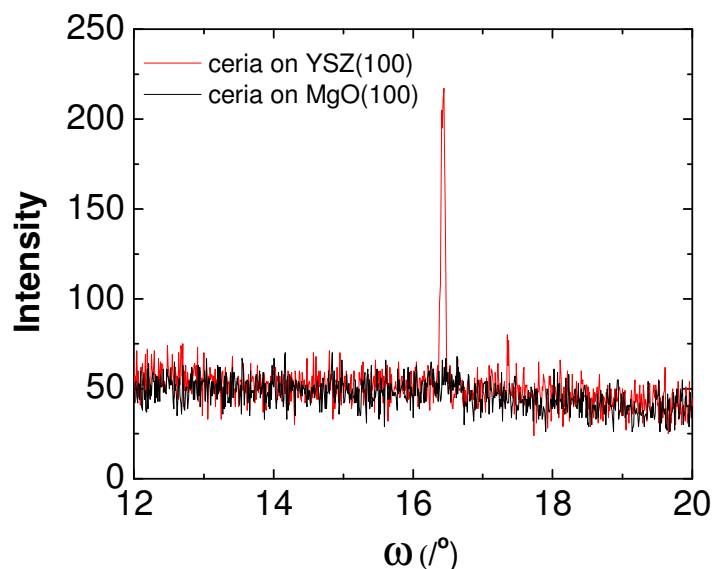


Figure 5.11 X-ray rocking curves ( $\omega$  scan) about the ceria 200 peak for two different films with ultra-thin ceria grown by CVD (Films #7 and # 8). The ceria on YSZ(100) shows a sharp peak, indicating an epitaxial relationship at the initial stages of film growth, whereas that grown on MgO does not. The FWHM of the peak is found to be 0.066 degrees by Gaussian fitting.

## 5.6 Conclusion

An optical transmittance analysis procedure was developed to extract the complex refractive index  $n$ , film thickness, and porosity of a film grown on a substrate with known index and zero extinction. Using thick, dense, smooth films, the dispersion behavior of undoped and 20% Sm-doped ceria was measured. The optical properties of the two compositions are similar, reflecting similarity in the electronic bonding characteristics. The indirect band gap implied by these data,  $\sim 3.2$  eV, falls within the range of values reported in the literature. In contrast, the direct band gap, derived assuming correlations between optical and electronic properties suggested by Wemple and DiDomenico (also  $\sim 3.2$  eV), is



smaller than the accepted value for ceria ( $\sim 3.7\text{eV}$ ). The source of the discrepancy remains to be elucidated, but may imply inapplicability of the correlations to ceria.

For films with known dispersion behavior but unknown microstructural characteristics, the latter (film thickness, porosity, and roughness) could be accurately extracted from the analysis methodology, as confirmed by comparison with SEM, profilometry, AFM and XRR measurements. It was further found that the symmetric Bruggeman model for material microstructure best represents the optical transmittance data over the alternative LLL model. The analysis results demonstrate the value of the transmittance method for evaluating film growth characteristics. Even for films as thin as 14 nm which display no interference fringes in their transmittance spectra, thickness and porosity can be determined. While XRR could be used to evaluate such films, optical transmittance has the advantage of fast measurements and ease of data acquisitions. In addition, unlike XRR, even very small area samples can be evaluated. Indeed, one can envision confining the illumination area to perform 2D mapping of the transmittance. Such an approach has recently been demonstrated to obtain thickness maps for relatively thick films ( $>5\mu\text{m}$ ) with presumably well-defined interference fringes [104].

## Chapter 6

# Summary and conclusions

Electrical, electrochemical, and optical properties of ceria films are studied. A chemical vapor deposition system is home-built for this study.

In electrical characterization, it was found that

- (1) Proton conductivity exists in porous columnar ceria films grown by MOCVD.
- (2) Unexpected water vapor dependence of proton conductivity unambiguously indicates that proton conduction occurs along exposed grain surfaces and parallel grain boundaries
- (3) The aligned microstructure of the ceria columnar films showed higher proton conductivity (factor of 4) compared to nanograined ceria sintered pellets in literature.

In electrochemical characterization, symmetric cell measurements were made to find the following.

- (1) Gas reaction orders were generally between 0 and 1, and ASR monotonically decreases with increasing  $p_{H_2O}$  or  $p_{O_2}$ .
- (2) Sm doping level does not provide satisfactory correlation with electrochemical reaction kinetics.
- (3) The ASR gas reaction orders change with degree of film texturing, and more (100) aligned film shows better performance with gas dependence similar to that of Pt nanoparticle decorated PLD porous films.

- (4) Best performance (smallest ASR) is linked to strong water dependence and weak hydrogen dependence. With opposite gas reaction orders, the ASR is large.

With asymmetric cells, we found the following.

- (1) ASR shows metal dependence conflicting previous work done with metal line patterns [24].
- (2) Anode polarization behavior deviates from Butler-Volmer type charge transfer mechanism.

In optical characterization,

- (1) We measured “true” bulk refractive index for undoped ceria and Sm-doped ceria.
- (2) With reference refractive index at hand, we demonstrate that it is possible to extract microstructural parameters from transmittance spectrum fitting.

## **Appendix A ACIS (alternating current impedance spectroscopy)**

### *A.1 ACIS principles*

In AC impedance spectroscopy (dielectric spectroscopy, electrochemical impedance spectroscopy, immittance spectroscopy), “resistance” is measured in a complex form to probe processes with different characteristic time constants. This is called (electrical) impedance, defined as the ratio of the voltage phasor to the electric current phasor in the frequency domain. Serial steps in the fastest route show up in the obtained spectra for electrochemical phenomena under study. Perturbation around thermodynamic equilibrium is induced by applying sinusoidal excitation voltage (or current). Typically, voltage/current amplitude stays in small range to ensure that system of interest is within the linear regime unless one intentionally increases the voltage/current amplitude to analyze system response by looking at higher-order harmonic signal.

One varies the frequency of this sinusoidal voltage (or current) wave to stimulate a process with matching time constant. This is quite similar to optical characterization tools such as raman spectroscopy and IR spectroscopy. In these methods, the probe, electromagnetic wave with a certain frequency, stimulates a specific vibrational mode in the system at the same frequency. In ACIS, excitation voltage wave with certain frequency serves as a probe stimulating a specific electrochemical process in the system at the same frequency. This measurement is performed in a set of discrete frequencies and often plotted in a complex plane (Nyquist plot). In another common data presentation, the real part and imaginary part are plotted separately against frequency (Bode plot).

When there is no DC bias (perturbation around open circuit condition), the impedance can be written as

$$Z(\omega) = \frac{V_o \exp(j\omega t)}{I_o \exp(j(\omega t + \theta))} = \frac{V_o}{I_o} \exp(-j\theta) = \frac{V_o}{I_o} (\cos \theta - j \sin \theta) = Z' + jZ'' \quad (\text{A.1})$$

where  $\theta$  is the frequency-dependent phase shift, and  $\omega$  is the angular frequency ( $\text{rad s}^{-1}$ ). For pure resistance, there is no phase shift, for instance. If inductive processes are involved, then the current wave precedes the voltage wave. On the contrary, a capacitive process retards the current wave so that voltage wave precedes it.

Fig. A.1 describes how ACIS measurements are made. It should be noted that the entire I-V polarization curve (steady state) can be reconstructed by measuring ACIS at different bias voltages (overpotentials) since ACIS measures the slope of the polarization curve. This is also possible in time domain measurements such as galvanostatic intermittent titration technique (GITT) or potentiostatic intermittent titration technique (PITT). However, analyzing data in the frequency domain helps to see the clear separation of the processes with different time constants.

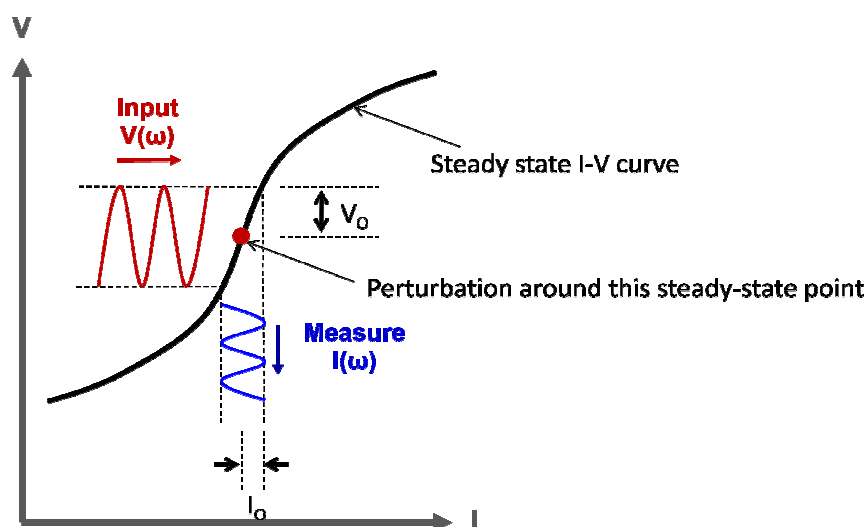


Figure A.1 AC impedance measurement scheme.

In Fig A.2, a Nyquist plot and two Bode plots are presented for an R-C parallel circuit to illustrate the conventional impedance data presentation. Two specific points are marked distinctly to help interpretation.

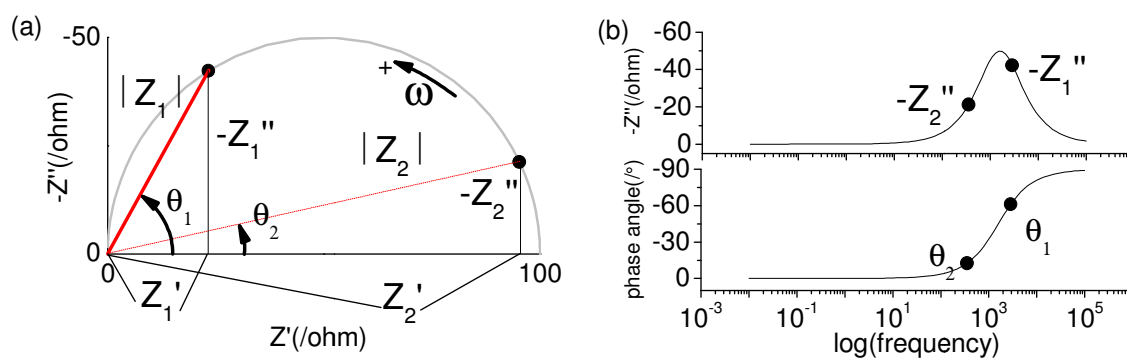


Figure A.2 The two common impedance data representations. (a) Nyquist plot which shows the impedance plane. This helps to recognize the characteristic pattern of relevant circuit. (b) Bode plots which show frequency dependence explicitly.

In ACIS literature, one can often find terms such as admittance,  $Y(\omega)$ , complex capacitance,  $C(\omega)$ , dielectric function,  $\varepsilon(\omega)$ , and modulus,  $M(\omega)$ . They are different forms of the same information. Their relationships to impedance,  $Z(\omega)$  is summarized;

$$Y(\omega) = \frac{1}{Z(\omega)}, C(\omega) = \frac{1}{Z(\omega)j\omega}, \varepsilon(\omega) = \frac{1}{Z(\omega)j\omega C_0}, M(\omega) = Z(\omega)j\omega C_0 \quad (\text{A.2})$$

Here,  $C_0$  means the capacitance of the empty cell calculated from cell dimensions and vacuum permittivity.

### A.2 Impedance of individual circuit elements

Pure resistor has no phase shift, so one can easily see that there is no imaginary part on its impedance expression. For a resistor, its impedance,  $Z(\omega)$  is simply  $R$  (positive real number). For a capacitor ( $C$ ), the impedance derivation is presented here;

$$I = \frac{dQ}{dt} = C \frac{dV}{dt}, \quad (\text{A.3-1})$$

$$V = V_0 \exp(j\omega t), \quad (\text{A.3-2})$$

$$I = C \frac{d(V_0 \exp(j\omega t))}{dt} = j\omega C V, \quad (\text{A.3-3})$$

$$Z_{\text{capacitor}}(\omega) = \frac{V(\omega)}{I(\omega)} = \frac{1}{j\omega C}. \quad (\text{A.3-4})$$

For an inductor ( $L$ ), the impedance derivation is given as

$$V = L \frac{dI}{dt}, \quad (\text{A.4-1})$$

$$I = I_0 \exp(j\omega t), \quad (\text{A.4-2})$$

$$V = L \frac{d(I_o \exp(j\omega t))}{dt} = j\omega LI \quad (A.4-3)$$

$$Z_{\text{inductor}}(\omega) = \frac{V(\omega)}{I(\omega)} = j\omega L \quad (A.4-4)$$

### A.3 Impedance of combined circuit elements

Firstly, R-C series circuit is considered. In a series connection, impedances can be added in a linear fashion.

$$Z_{\text{RC series}} = R + \frac{1}{j\omega C}, Y_{\text{RC series}} = \frac{1}{R - j/\omega C} = \frac{\omega^2 C^2 R}{1 + \omega^2 C^2 R^2} + j \frac{\omega C}{1 + \omega^2 C^2 R^2} \quad (A.5)$$

For R-C parallel circuit, admittance can be added in a linear fashion.

$$Y_{\text{RC parallel}} = \frac{1}{R} + j\omega C, Z_{\text{RC parallel}} = \frac{R}{1 + \omega^2 R^2 C^2} - j \frac{\omega R^2 C}{1 + \omega^2 R^2 C^2} \quad (A.6)$$

For R-L parallel circuit,

$$Y_{\text{RL parallel}} = \frac{1}{R} + \frac{1}{j\omega L}, Z_{\text{RL parallel}} = \frac{R\omega^2 L^2}{R^2 + \omega^2 L^2} + j \frac{R^2 \omega L}{R^2 + \omega^2 L^2} \quad (A.7)$$

For R-L-C parallel circuit,

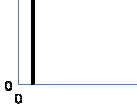
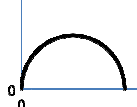
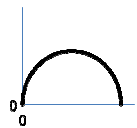
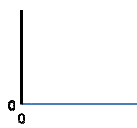
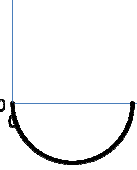
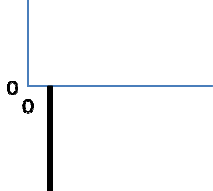
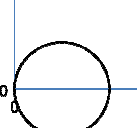
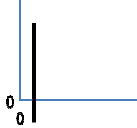
$$Y_{\text{RLC parallel}} = \frac{1}{R} + \frac{1}{j\omega L} + j\omega C, \quad (A.8)$$

$$Z_{\text{RLC parallel}} = \frac{1}{R(\frac{1}{R^2} + (\omega C - \frac{1}{\omega L})^2)} + j(\frac{1}{\omega L(\frac{1}{R^2} + (\omega C - \frac{1}{\omega L})^2)} - \frac{\omega C}{\frac{1}{R^2} + (\omega C - \frac{1}{\omega L})^2})$$

For all the cases, either semi-circular or circular Nyquist plot can be obtained in either admittance or impedance plane. This is illustrated in table A.1. To get the analytic expression of the impedance as in Eq. (A.8), an online mathematics tool is used [105].



Table A.1 Nyquist plot on impedance/admittance plane for combined circuit elements

	Nyquist plot	
	Impedance plane x axis; $Z'$ , y axis; $-Z''$	Admittance plane x axis; $Y'$ , y axis; $Y''$
R-C series		
R-C parallel		
R-L parallel		
R-L-C parallel		

From Eq. (A.5), we can take derivative on  $Y''$  to get the  $\omega_{top}$  expression.

$$\frac{d\left(\frac{\omega C}{1 + \omega^2 C^2 R^2}\right)}{d\omega} = 0 \text{ when } \omega = \omega_{top}.$$

Solving this, one can see that  $\omega_{top} = \frac{1}{RC}$  for R-C series circuit.

The same calculation on  $Z''$  proves that  $\omega_{top} = \frac{1}{RC}$  also for R-C parallel circuit (Eq.

(A.6)).

These time constants are defined in admittance plane for R-C series circuit and in impedance plane for R-C parallel circuit, respectively.

In practice, these simple combinations cannot represent the total signal of an electrochemical system over several decades of frequency range. One needs to consider an equivalent circuit involving larger number ( $N=N_0$ ) of simple sub-circuit elements described so far or combination of “distributed” elements ( $N \leq N_0$ ). One example of these distribution elements is given in the following section. For a fuel cell under operational condition, the equivalent circuit often requires 5 or more R-C parallel circuits in series. Fig. A.3 shows an example of the impedance data from a fuel cell under operation [106]. Individual contributions (anode processes, cathode processes, gas diffusion, and conversion [107]) with different time constants are marked as small semicircles inside the total impedance trace.

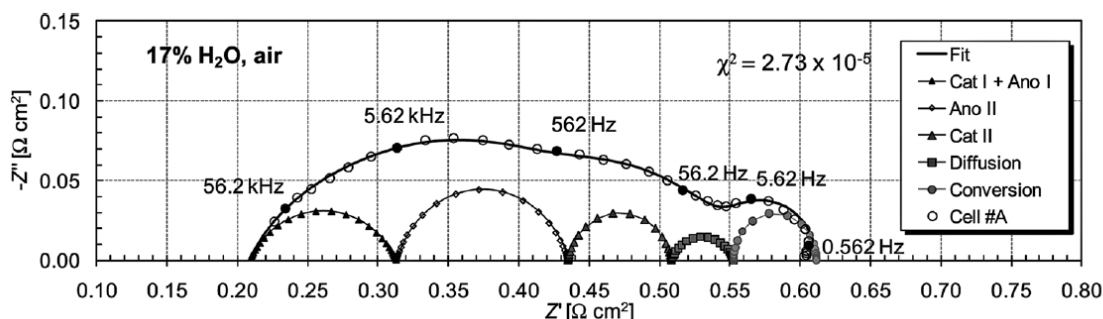


Figure A.3 Impedance spectrum and corresponding fit for an anode supported fuel cell. Anode condition: 83% hydrogen and 17% water. Cathode condition: air. Operation temperature: 750°C [106].

#### A.4 Constant phase element (CPE)

In ACIS experiments, depressed semicircles are often encountered. This is explained by exponential distribution of the relaxation times. A circuit element that can describe this behavior has been proposed as a constant phase element. The impedance of a constant phase element is defined [108];

$$Z_{CPE} = \frac{1}{A(j\omega)^n}, -1 \leq n \leq 1. \quad (A.9)$$

When  $A=C$ , and  $n=1$ , the CPE acts like a capacitor. When  $A=R^{-1}$ , and  $n=0$ , the CPE acts like a resistance. When  $A=L^{-1}$ , and  $n=-1$ , the CPE acts like an inductor. The constant phase angle,  $\theta$  is determined as  $n\pi/2$ , which is the reason of the name. This behavior is described in Fig. A.4 using a ZARC element (parallel connection of a CPE and a resistor) with various  $n$  values. Simulation curves are drawn with  $R=100\Omega$ ,  $C=10^{-6}F$ , and various  $n$  (0.6~1) using ZView2 software.

For a ZARC element, one can perform the same procedure (taking derivative on  $Z''$  and setting it equal to zero) in section 1.3.3 to calculate  $\omega_{top}$  in terms of  $R$ ,  $Q (=A^{1/n})$ , and  $n$ . Then, from this expression one can estimate equivalent capacitance.

$$RC_{equivalent} = \text{time constant} = \frac{1}{\omega_{top}} = R^{1/n} Q \quad (A.10)$$

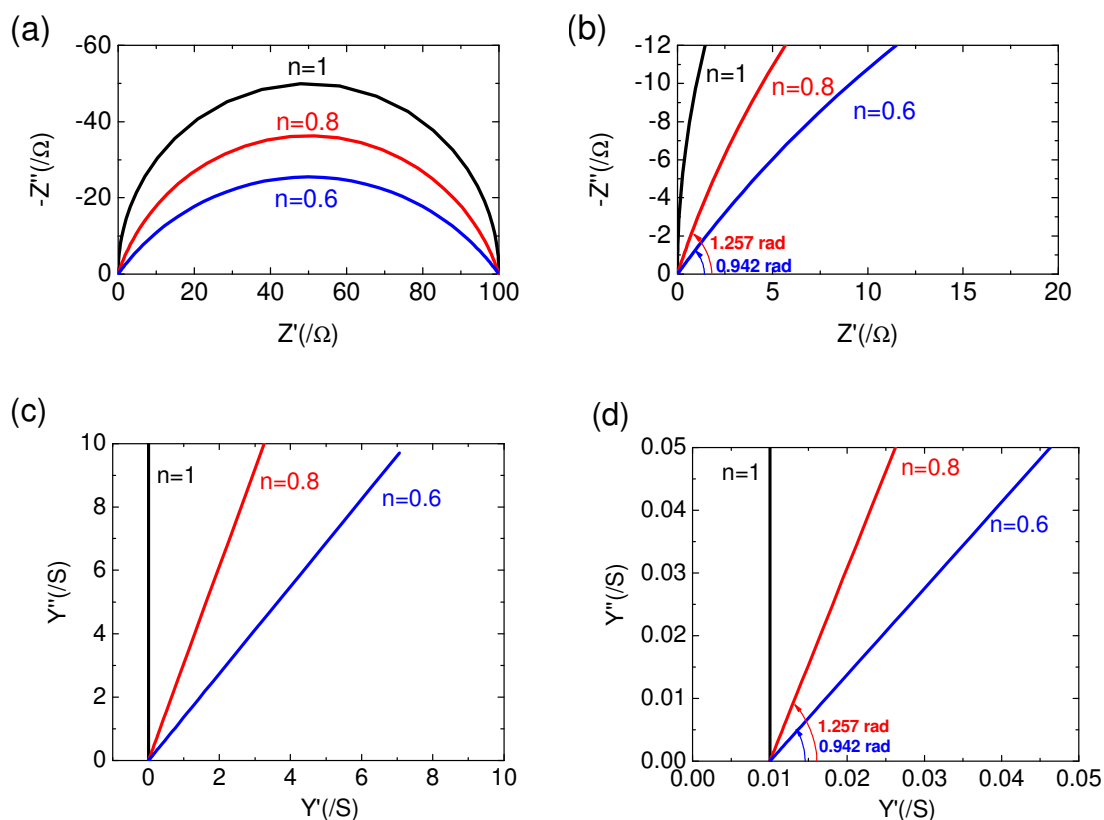


Figure A.4 ZARC circuit impedance Nyquist plot. (a) impedance presentation, (c) admittance presentation. (b) and (d) are the zoomed-in view of the (a) and (c) near origin, respectively.

In Fig. A.5, the distribution of the relaxation time is numerically calculated for synthetic ZARC impedance data with three different  $n$  values. This type of calculation is usually done when there is no appropriate model available to fit the impedance data. Here, the distribution of the relaxation time (DRT) is calculated to demonstrate how lower  $n$  corresponds to the broader distribution of the relaxation times in a quantitative manner. LEVMW software (Version 8. 11) from Macdonald is used with 19 R-C parallel circuit elements in series (hence, 19 different time constants) to get the distribution function. The number of circuit elements is limited to 19 due to technical reason, and can be increased by modifying the original code. This circuit here is called Voigt circuit in literature [109].

Synthetic data is produced with  $R=100$  ohms,  $Q=1E-6 \Omega^{-1/n}\text{sec}$ ,  $n=0.6\sim 0.8$ . (QPE, constant phase element#2 in ZView2 notation). Solid lines are from Gaussian fittings to the 19 “data points” per curve. Log-normal nature of the distribution is well presented. With fixed  $R$  and  $Q$ , the increase of the time constant with decreasing  $n$  value is expected according to Eq. (A.10). One depressed semi-circle has been decomposed into 19 smaller perfect semicircles with definite time constants. For this demonstration, number of R-C parallel circuit elements was increased from 1 to 19 one by one, achieving stable fitting at each step.

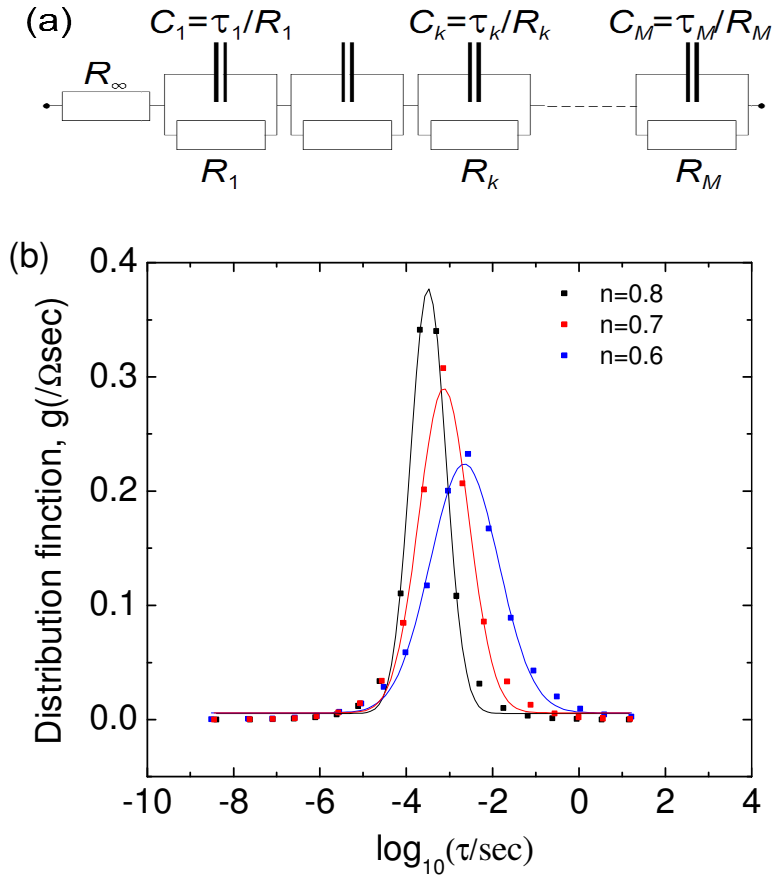


Figure A.5 Distribution of relaxation times. (a) Voigt circuit with 19 different time constants ( $M=19$ ). For this demonstration,  $R_\infty$  is set to zero for simplicity. (b) ZARC circuit impedance relaxation time distribution.

## Appendix B Optical transmittance

### B.1 Transmittance basics

In a broad context, transmittance measures transmitted fraction of incident energy flux. In optical transmittance, energy is related to light intensity. Optical transmittance often denoted as  $T$ , decreases whenever there is absorption, reflection or scattering event for the incident photons. When traveling from the light source through the sample to the detector, a photon with certain wavelength has a probability to encounter these absorption/reflection/scattering events. This probability differs from that of another photon at different energy level. Thus, transmittance depends on the incident photons' wavelength and their interaction with sample.

In this work, optical transmittance means in-line transmittance ( $0 \leq T \leq 1$ ). No integrating sphere was used.

For transmittance as defined here,

$$T + A + R = 1; \quad (\text{B.1})$$

$T$  means transmittance,  $A$  means absorptance (different from absorbance), and  $R$  means reflectance. Absorbance as defined in Beer-Lambert law becomes 1 when 90% of the light is absorbed (Absorbance =  $\log_{10} I_0/I$ ) whereas absorptance becomes 1 when all the light is absorbed.

In practice, the spectrometer determines transmittance from the following equation.

$$T = \frac{S - D}{R - D} \quad (\text{B.2})$$

$S$  is the measured intensity, determined by the current at the light detector, when the sample is inserted in the light path.  $D$  means dark intensity (dark current) quantifying the

background signal when there is no light shining on the detector.  $R$  is the reference intensity. Here, the empty cell is the reference with  $T=1$ .

The sample has two distinct groups of features that determine how the light will interact with it. The first group consists of intrinsic optical properties of the constituent material(s), which manifest as refractive indices. The other comes from the geometry, or microstructural features such as thickness, porosity and surface roughness.

For thin film geometry, the “sample” consists of a substrate and film on top of it. Thus, the substrate refractive index also affects resultant transmittance. There are three interfaces under consideration; (i) air-film, (ii) film-substrate, (iii) substrate-air.

The transmittance expression for an ideal thin film with uniform thickness  $d$ , and uniform optical property has been reported [93] (light absorption in substrate ignored);

$$T = \frac{Fx}{G - Hx + Kx^2}, \quad (\text{B.3})$$

where

$$x = \exp(-\alpha d), \quad (\text{B.3-1})$$

$$\alpha = \text{absorption coefficient} = 4\pi k / \lambda, \quad (\text{B.3-2})$$

$$F = 16s(n^2 + k^2), \quad (\text{B.3-3})$$

$$G = [(n+1)^2 + k^2][(n+1)(n+s^2) + k^2], \quad (\text{B.3-4})$$

$$H = [(n^2 - 1 + k^2)(n^2 - s^2 + k^2) - 2k^2(s^2 + 1)] \cdot 2\cos\phi - k[2(n^2 - s^2 + k^2) + (s^2 + 1)(n^2 - 1 + k^2)] \cdot 2\sin\phi, \quad (\text{B.3-5})$$

$$K = [(n-1)^2 + k^2][(n-1)(n-s^2) + k^2], \quad (\text{B.3-6})$$

and

$\phi$  = the phase (in wavelength space) of the interference fringes  $= 4\pi nd / \lambda$ . (B.3-7)

$$\mathbf{n}_{\text{subtrate}} = s - ik_s = s(\lambda),$$

$$\mathbf{n}_{\text{film}} = n - ik = n(\lambda) - ik(\lambda).$$



## Appendix C Effective medium theory

### C.1 *Effective medium theory basics*

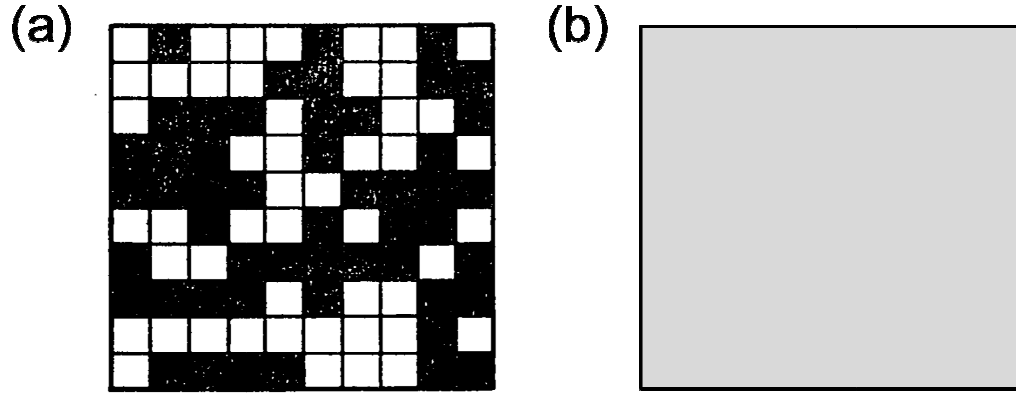


Figure C.1 Graphical description of effective medium theory. (a) 2D representation of a porous material [110]. Black squares: material with full density, and white squares: pore filled with air. Different effective medium models can develop at this stage depending on how one simplifies the complex microstructure into “black and white pattern” (b) hypothetical material with “average” dielectric constant. There is no pore structure left. The sample response to an external stimulation is indistinguishable between (a) and (b) regarding conductivity or transmittance, for instance.

To extract porosity from transmittance fitting as done in chapter 5, there should be a mathematical expression that correlates the refractive indices and mass density. There exist several models that deal with effective dielectric constant of mixtures. Often, they are called dielectric mixing rules. In this line of reasoning, we view the porous system as two-phase mixture of air and fully dense material of interest, and replace the microstructure-specific optical constants with those of a hypothetical one-phase material of averaged-out property. This is illustrated in Fig. C.1.

Resultant effective complex dielectric constant ( $\epsilon = \epsilon_1 - i\epsilon_2$ ) can then be easily converted to effective complex refractive index ( $n = n - ik$ ) using following equations [111].

$$\begin{aligned}
\varepsilon_1 &= n^2 - k^2, \quad \varepsilon_2 = 2nk. \\
n &= \left( \frac{(\varepsilon_1^2 + \varepsilon_2^2)^{1/2} + \varepsilon_1}{2} \right)^{1/2}, \\
k &= \left( \frac{(\varepsilon_1^2 + \varepsilon_2^2)^{1/2} - \varepsilon_1}{2} \right)^{1/2}.
\end{aligned} \tag{C.1}$$

This effective complex refractive index is fed to Eq. (B.3), and the theoretical transmittance can be determined for known film thickness and known film porosity.

The Maxwell Garnett function is the most well documented model among various dielectric mixing rules [112]. Its mathematical form for spherical inclusion is presented here (for ellipsoidal inclusion, generalized Maxwell Garnett function is also well-known);

$$\varepsilon_{eff} = \varepsilon_b \left[ 1 + \frac{3f_p \left( \frac{\varepsilon_p - \varepsilon_b}{\varepsilon_p + 2\varepsilon_b} \right)}{1 - f_p \left( \frac{\varepsilon_p - \varepsilon_b}{\varepsilon_p + 2\varepsilon_b} \right)} \right] \tag{C.2}$$

The meaning of symbols can be found in following Eq. (C.3). One distinct feature of this function is that the matrix and inclusion are not exchangeable. The resultant effective dielectric constant depends on the how one attribute each phase: it matters which phase is treated as matrix and which phase corresponds to inclusion.

After its first derivation by Maxwell Garnett, it has been rederived under various sets of assumptions. However, we did not use this model. Instead, we considered symmetric Bruggeman model. Both of them come from the same parent integral equation. The difference stems from approximations that are made. The approximation leading to symmetric Bruggeman model is called CPA (coherent potential approximation) while the

other one for Maxwell Garnett model is called ATA (average t-matrix approximation) [113]. It is beyond the scope of this work to discuss these approximations.

In total, we considered three specific forms of effective medium models. The first is just mentioned symmetric Bruggeman (S-BG) model for binary mixtures, in which there is no distinction between continuous (matrix) and discontinuous (inclusion) phases; each inclusion is in contact with other inclusions of either phase. It is called symmetric since the resultant effective dielectric constant does not change when we swap the matrix and inclusion. The result for sphere-shaped inclusions is expressed as [111]

$$f_b \frac{\epsilon_b - \epsilon_{eff}}{\epsilon_{eff} + \frac{1}{3}(\epsilon_b - \epsilon_{eff})} + f_p \frac{\epsilon_p - \epsilon_{eff}}{\epsilon_{eff} + \frac{1}{3}(\epsilon_p - \epsilon_{eff})} = 0 \quad (C.3)$$

where

$f_b$  = volume fraction of oxide,

$f_p$  = volume fraction of pore (total porosity) ,

$\epsilon_b$  = dielectric function of fully dense oxide,

$\epsilon_p = 1$  (air) =  $\epsilon_p$ ,

$\epsilon_{eff}$  = effective dielectric function (oxide/air composite).

Of the two roots to Eq. (C.3), only one is physically meaningful, and it reads

$$\epsilon_{eff} = \frac{(3f_b\epsilon_b - \epsilon_b - \epsilon_p + 3f_p\epsilon_p) + \sqrt{(3f_b\epsilon_b - \epsilon_b - \epsilon_p + 3f_p\epsilon_p)^2 + 8\epsilon_b\epsilon_p}}{4} \quad (C.4)$$

The second formalism is the asymmetric Bruggeman (A-BG) model, in which it is assumed that the inclusions, air-filled pores in our case, are always spherical and are coated

with matrix material such that pores cannot make direct contact each other [114]. The A-BG model yields an implicit form for  $\epsilon_{eff}$  as shown below:

$$\frac{\epsilon_p - \epsilon_{eff}}{\epsilon_p - \epsilon_b} = (1 - f_p) \left( \frac{\epsilon_{eff}}{\epsilon_b} \right)^{1/3} \quad (C.5)$$

The solution for  $\epsilon_{eff}$  from the above is obtained using Sihvola's series expansion method.

The complete form can be found in Ref. [115] (p. 221).

Looyenga and Landau-Lifshitz independently derived a third dielectric mixing law (henceforth the LLL model) in which the host and matrix phases are assigned dielectric constant values of  $\epsilon_{eff} + \Delta\epsilon$  and  $\epsilon_{eff} - \Delta\epsilon$  [116, 117], and no assumptions are made regarding phase distributions. The result is given as

$$\epsilon_{eff} = [(\epsilon_p^{1/3} - \epsilon_b^{1/3})f_p + \epsilon_b^{1/3}]^3 \quad (C.6)$$

While there are some instances in which this expression fits experimental data more closely than the Bruggeman expressions and the absence of microstructural assumptions renders the approach attractive, the LLL model fails when the permittivity of the host material differs greatly from that of the inclusion.

Fig. C.2 compares how these three models differ from each other.

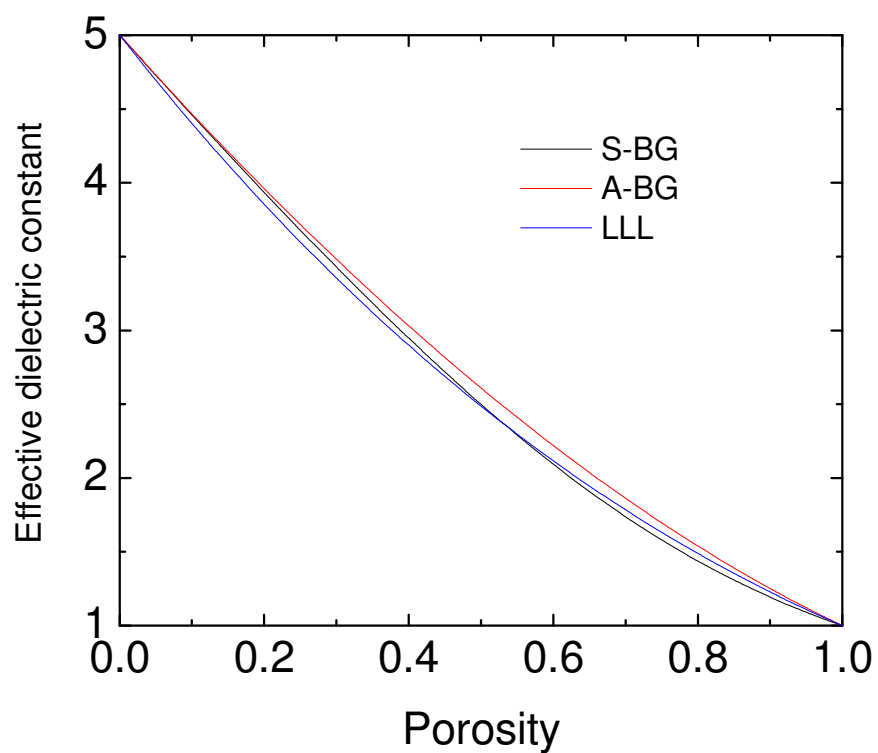


Figure C.2 Effective dielectric constant of a mixture. In real system, only the region where the porosity is below 0.5 becomes relevant. This mixing curve is drawn for a certain frequency where pore dielectric constant is 1 (air), and material dielectric constant is 5.

## Appendix D Thin film characterization by X-ray

### D.1 X-ray diffraction

Thin film microstructure is often studied by X-ray diffraction. For thin films, typical  $\theta$ - $2\theta$  scan, which represents overall property in the case of powder sample, gives information on the z-direction only. Thus, lattice constants or crystallite size calculated from this scan can only correspond to out-of-plane properties. In this work, in-plane property has not been analyzed from X-ray. No phi-scan has been done since MOCVD grown films are expected to have random orientation in this direction.

A rocking curve often reveals the substrate-film structural relationship. In this measurement, only the sample moves (omega changes) with the detector and X-ray tube staying put. For perfect lattice matching as in the case of homoepitaxy (for instance, Si on Si), the FWHM of the rocking curve is expected to be zero, ideally. This never happens, since even single crystals are not free from defects, and instrumental broadening always exists. With this omega scan, one essentially looks into the lateral (in-plane) spread of the out-of-plane texture.

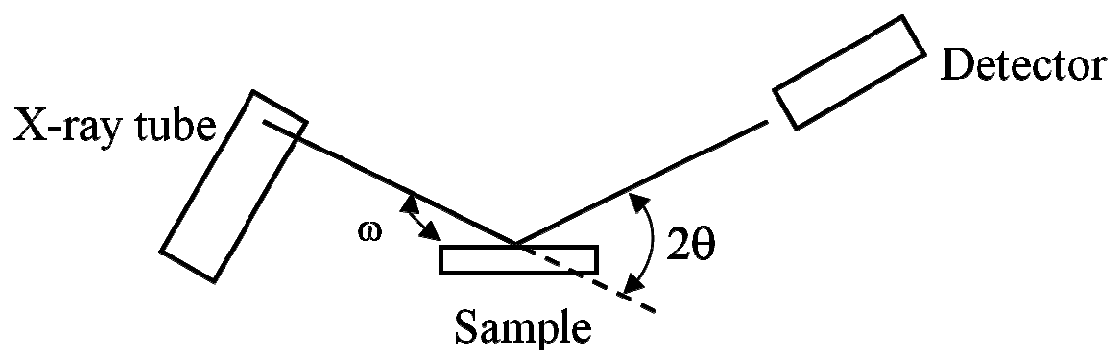


Figure D.1 Bragg-Brentano geometry for typical X-ray diffractometer.

## D.2 X-ray reflection

Film thickness, density and surface roughness are the parameters that can be studied by X-ray reflection. To the first approximation, critical angle, the angle where the reflected intensity starts to drop off, is largely determined by film density. Higher density means larger critical angle. The steepness of the intensity drop is largely determined by film roughness. The oscillation period at low intensity region is determined by film thickness (Kiessig fringe, which is just an interference fringe). In XRR, what is probed is the electron density change at the interface, and how quickly this change happens (roughness). If there are two different imaginary materials that have same electron density, then the incident X-ray photons will not feel the difference, and XRR will not work. Electron density is important because photons of X-ray wavelength gets reflected by electron cloud around nucleus. This parameter is also closely related to mass density. This is why XRR is a good method to determine film density as long as the film thickness within suitable range. After collecting the reflection intensity as a function of incident angle, one needs to fit the reflectivity trace to model. The fitting parameters will be film thickness, film density, and surface roughness. In this regards, it is very similar to the fitting procedure developed in chapter 5 for transmittance.

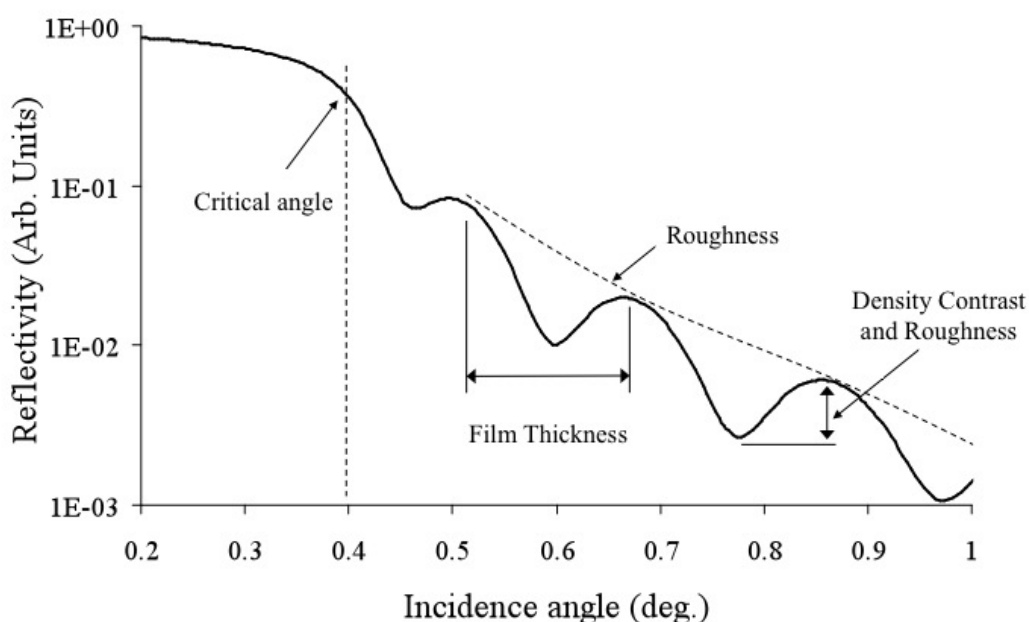


Figure D.2 XRR pattern example and interpretation [118].

One may realize that there should be two critical angles for a single layer film on a substrate: one for the film, and the other for the substrate. This is true, but the two critical angles are not always clearly detected. When the electron density of the film is larger than the electron density of the substrate, it is likely to see only one critical angle, which is for the film. In the opposite case, one has higher chance to see the two separate critical angles.

This is illustrated in Fig. D.3. For these two theoretical curves, simulation is done with X'Pert Reflectivity software (version 1.0) using common substrate (MgO, mass density =  $3.58\text{g/cm}^3$ ). Critical angles for three components are indicated by vertical markers. Mass density for  $\text{SiO}_2$  is  $2.64\text{ g/cm}^3$ , and that for  $\text{CeO}_2$  is  $7.21\text{ g/cm}^3$ . One can see that there are interference fringes between the critical angle of the film and the critical angles of the substrate for case (b). For case (a), it is hard to see the critical angle of the low density substrate.



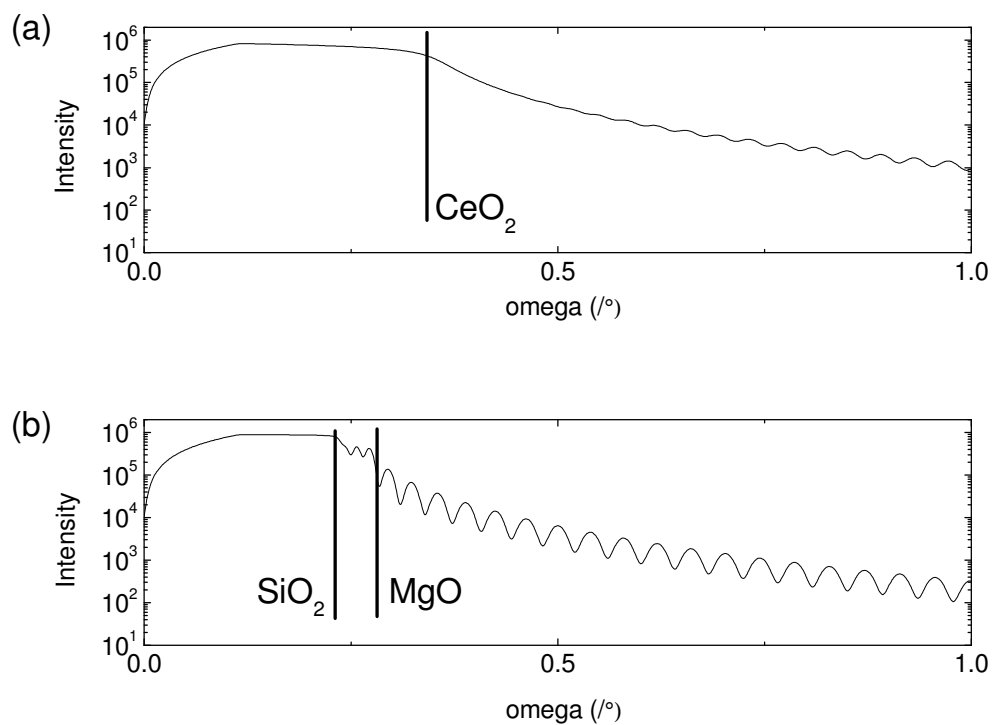


Figure D.3 XRR pattern examples for two different cases. (a) High electron density film on low electron density substrate. (b) Low electron density film on high electron density substrate. Electromagnetic wave penetrates through the low electron density film whereas it cannot penetrate through high electron density film.

# Reference

1. W. R. Grove. On voltaic series and the combination of gases by platinum. *Phil. Mag.* 14 (1839) 127-130.
2. Ishihara, T., J. Yan, M. Shinagawa, and H. Matsumoto. Ni-Fe Bimetallic Anode as an Active Anode for Intermediate Temperature SOFC Using LaGaO<sub>3</sub> Based Electrolyte Film. *Electrochimica Acta* 52 (2006) 1645-1650.
3. D. R. Gaskell. *Introduction to the Thermodynamics of Materials*. 5<sup>th</sup> edition. Taylor & Francis (2008).
4. R. O'Hayre, Suk-Won Cha, Whitney Colella, and Fritz Prinz. *Fuel Cell Fundamentals*. Wiley (2005).
5. C. Wagner. Proc. 7th Int. Comm. Electrochem. Thermodyn. Kinet., Lindau 1955 Butterworth, London (1956) 361-377.
6. H.-I. Yoo. EMF behavior of oxygen concentration cells involving a ternary or higher oxide with mobile cations. *Solid State Ionics* 154-155 (2002) 87-91.
7. S.M. Haile. Fuel cell materials and component. *Acta Materialia* 51 (2003) 5981-6000.
8. Duncan, Keith L., Kang-Taek Lee, and Eric D. Wachsman. Dependence of Open-Circuit Potential and Power Density on Electrolyte Thickness in Solid Oxide Fuel Cells with Mixed Conducting Electrolytes. *Journal of Power Sources* 196 (2011) 2445-2451.

9. Bard, A. J.; Faulkner, L. R. *Electrochemical Methods: Fundamentals and Applications*. Wiley (2000).
10. Kyung Joong Yoon, Srikanth Gopalan, and Uday B. Pal. Analysis of electrochemical performance of SOFCs using polarization modeling and impedance measurements. *Journal of the Electrochemical Society* 156 (2009) B311-B317.
11. G. W. Castellan. *Physical Chemistry*. 3<sup>th</sup> edition. Addison Wesley (1983).
12. A. V. da Rosa. *Fundamentals of Renewable Energy Processes*. Academic Press (2005)
13. Wei Lai and Sossina M. Haile. Impedance Spectroscopy as a Tool for Chemical and Electrochemical Analysis of Mixed Conductors: A Case Study of Ceria. *Journal of the American Ceramic Society* 88 (2005) 2979-2997.
14. M. Mogensen and K. Kammer. Conversion of hydrocarbons in solid oxide fuel cells. *Annual Review of Materials Research* 33 (2003) 321-331.
15. EG & G Services and National Energy Technology Laboratory. *Fuel cell handbook: 7th edition* (2004).
16. S. J. Litzelman, J. L. Hertz, W. Jung, and H. L. Tuller. Opportunities and Challenges in Materials Development for Thin Film Solid Oxide Fuel Cells. *Fuel Cells* 8 (2008) 294-302
17. J. Will, A. Mitterdorfer, C. Kleinlogel, D. Perednis, and L.J. Gauckler. Fabrication of thin electrolyte for second-generation SOFC. *Solid State Ionics* 131 (2000) 79-96.

18. Tsepin Tsai and Scott A. Barnett. Bias Sputter Deposition of Dense Ytria-Stabilized Zirconia Films on Porous Substrates. *Journal of the Electrochemical Society* 142 (1995) 3084-3087.
19. Cheng-Chieh Chao, Ching-Mei Hsu, Yi Cui and Fritz B. Prinz. Improved Solid Oxide Fuel Cell Performance with Nanostructured Electrolytes. *ACS Nano* 5 (2011) 5692-5696.
20. Ying Liu, William Rauch, Shaowu Zha, Meilin Liu. Fabrication of  $\text{Sm}_{0.5}\text{Sr}_{0.5}\text{CoO}_3\text{-Sm}_{0.1}\text{Ce}_{0.9}\text{O}_2$  cathodes for solid oxide fuel cells using combustion CVD. *Solid State Ionics* 166 (2004) 261-268.
21. WooChul Jung, Julien O. Dereux, William C. Chueh, Yong Hao, and Sossina M. Haile. High electrode activity of nanostructured, columnar ceria films for solid oxide fuel cells. *Energy Environ. Sci.*, 5 (2012) 8682-8689.
22. V. Brichzin, J. Fleig, H.-U. Habermeier, and J. Maier. Geometry Dependence of Cathode Polarization in Solid Oxide Fuel Cells Investigated by Defined Sr-Doped  $\text{LaMnO}_3$  Microelectrodes. *Electrochemical and Solid-State Letters* 3 (2000) 403-406.
23. WooChul Jung and Harry L. Tuller. Investigation of Cathode Behavior of Model Thin-Film  $\text{SrTi}_{1-x}\text{Fe}_x\text{O}_{3-\delta}$  ( $x = 0.35$  and  $0.5$ ) Mixed Ionic-Electronic Conducting Electrodes. *Journal of the Electrochemical Society* 155 (2008) B1194-B1201.
24. William C. Chueh, Yong Hao, WooChul Jung and Sossina M. Haile. High electrochemical activity of the oxide phase in model ceria-Pt and ceria-Ni composite anodes. *Nature Materials* 11 (2012) 155-161.

25. Huang, Hong, Masafumi Nakamura, Peichen Su, Rainer Fasching, Yuji Saito, and Fritz B. Prinz. High-Performance Ultrathin Solid Oxide Fuel Cells for Low-Temperature Operation. *Journal of the Electrochemical Society* 154 (2007) B20-B24.
26. Yunxiang Lu, Cortney Kreller, and Stuart B. Adler. Measurement and Modeling of the Impedance Characteristics of Porous  $\text{La}_{1-x}\text{Sr}_x\text{CoO}_3$  Electrodes. *Journal of the Electrochemical Society* 156 (2009) B513-B525
27. Weiwei Sun, Xiqiang Huang, Zhe Lu, Lijun Zhao, Bo Wei, Shuyan Li, Kongfa Chen, Na Ai, and Wenhui Su. NiO+YSZ anode substrate for screen-printing fabrication of YSZ electrolyte film in solid oxide fuel cell. *Journal of Physics and Chemistry of Solids* 70 (2009) 164–168.
28. Ulrich P. Muecke, Daniel Beckel, Andre Bernard, Anja Bieberle-Hütter, Silvio Graf, Anna Infortuna, Patrik Müller, Jennifer L. M. Rupp, Julian Schneider, and Ludwig J. Gauckler. Micro Solid Oxide Fuel Cells on Glass Ceramic Substrates. *Advanced Functional Materials* 18 (2008) 3158-3168.
29. I. Zhitomirsky and A. Petric. Electrophoretic deposition of electrolyte materials for solid oxide fuel cells. *Journal of Materials Science* 39 (2004) 825-831.
30. Milton Ohring. *The Materials Science of Thin Films*. Academic Press (1992).
31. Li Qingwen, Yan Hao, Cheng Yan, Zhang Jin, and Liu Zhongfan. A scalable CVD synthesis of high-purity single-walled carbon nanotubes with porous MgO as support material. *Journal of Materials Chemistry* 12 (2002) 1179-1183.
32. Albert Burk. Development of Multiwafer Warm-Wall Planetary VPE Reactors for SiC Device Production. *Chemical Vapor Deposition* 12 (2006) 465-473.

33. Jesus J. Gallegos III, Timothy L. Ward, Timothy J. Boyle, Mark A. Rodriguez, and Laila P. Francisco. Neo-pentoxide Precursors for MOCVD Thin Films of  $\text{TiO}_2$  and  $\text{ZrO}_2$ . *Chemical Vapor Deposition* 6 (2000) 21-26.
34. Kueir-Weei Chour, Jong Chen, and Ren Xu. Metal-organic vapor deposition of YSZ electrolyte layers for solid oxide fuel cell applications. *Thin Solid Films* 304 (1997) 106-112
35. Johannes Seydel, Michael Becker, Ellen Ivers-Tiffée, and Horst Hahn. Granular nanocrystalline zirconia electrolyte layers deposited on porous SOFC cathode substrates. *Materials Science and Engineering B* 164 (2009) 60-64
36. Christoph Peters, Andre Weber, Benjamin Butz, Dagmar Gerthsen, and Ellen Ivers-Tiffée. Grain-Size Effects in YSZ Thin-Film Electrolytes. *Journal of the American Ceramic Society*. 92 (2009) 2017–2024.
37. Marcus C. Göbel, Giuliano Gregori, Xiangxin Guo, and Joachim Maier. Boundary effects on the electrical conductivity of pure and doped cerium oxide thin films. *Phys. Chem. Chem. Phys.* 12 (2010) 14351-14361.
38. N. Schichtel, C. Korte, D. Hesse, and J. Janek. Elastic strain at interfaces and its influence on ionic conductivity in nanoscaled solid electrolyte thin films—theoretical considerations and experimental studies. *Phys. Chem. Chem. Phys.* 11 (2009) 3043-3048.
39. Darja Kek-Merl, Jyrki Lappalainen and Harry L. Tuller. Electrical Properties of Nanocrystalline  $\text{CeO}_2$  Thin Films Deposited by In Situ Pulsed Laser Deposition. *J. Electrochem. Soc.* 153 (2006) J15-J20.

40. Frank S. Baumann, Jürgen Fleig, Hanns-Ulrich Habermeier, and Joachim Maier. Impedance spectroscopic study on well-defined (La,Sr)(Co,Fe)O<sub>3-δ</sub> model electrodes. *Solid State Ionics* 177 (2006) 1071-1081.
41. WooChul Jung and Harry L. Tuller. Impedance study of SrTi<sub>1-x</sub>Fe<sub>x</sub>O<sub>3-δ</sub> (x=0.05 to 0.80) mixed ionic-electronic conducting model cathode. *Solid State Ionics* 180 (2009) 843-847.
42. J. Mizusaki, H. Tagawa, T. Saito, T. Yamamura, K. Kamitani, K. Hirano, S. Ehara, T. Takagi, T. Hikita, M. Ippommatsu, S. Nakagawa, and K. Hashimoto. Kinetic studies of the reaction at the nickel pattern electrode on YSZ in H<sub>2</sub>-H<sub>2</sub>O atmospheres. *Solid State Ionics* 70/71 (1994) 52-58.
43. A. Bieberle, L.P. Meier, and L.J. Gauckler. The Electrochemistry of Ni Pattern Anodes Used as Solid Oxide Fuel Cell Model Electrodes. *J. Electrochem. Soc.* 148 (2001) A646-A656.
44. B. de Boer. Ph.D. thesis, University of Twente (1998).
45. Kenji A. Sasaki, Yong Hao, and Sossina M. Haile. Geometrically asymmetric electrodes for probing electrochemical reaction kinetics: a case study of hydrogen at the Pt–CsH<sub>2</sub>PO<sub>4</sub> interface. *Phys. Chem. Chem. Phys.* 11 (2009) 8349-8357.
46. William C. Chueh, Christoph Falter, Mandy Abbott, Danien Scipio, Philipp Furler, Sossina M. Haile, and Aldo Steinfeld. High-Flux Solar-Driven Thermochemical Dissociation of CO<sub>2</sub> and H<sub>2</sub>O Using Nonstoichiometric Ceria. *Science* 330 (2010) 1797-1801.

47. S. Guo, H. Arwin, S. N. Jacobsen, K. Järrendahl, and U. Helmersson. A spectroscopic ellipsometry study of cerium dioxide thin films grown on sapphire by RF magnetron sputtering. *J. Appl. Phys.* 77 (1995) 5369-5376.
48. F. Marabelli and P. Wachter. Covalent insulator CeO<sub>2</sub>: optical reflectivity measurements. *Phys. Rev. B.* 36 (1987) 1238-1243.
49. G. Hass, J. B. Ramsey, and R. Thun. Optical properties and structures of cerium dioxide films. *J. Opt. Soc. Am.* 48 (1958) 324-327.
50. P. Patsalas, S. Logothetidis, and C. Metaxa. Optical performance of nanocrystalline transparent ceria films. *Appl. Phys. Lett.* 81 (2002) 466-468.
51. R. M. Bueno, J. M. Martinez-Duart, M. Hernandez-Velez and L. Vasquez. Optical and structural characterization of RF sputtered CeO<sub>2</sub> thin films. *J. Mater. Sci.* 32 (1997) 1861-1865.
52. L. Méchin, A. Chabli, F. Bertin, M. Burdin, G. Rolland, C. Vannuffel, and J.-C. Villégier. A combined x-ray specular reflectivity and spectroscopic ellipsometry study of CeO<sub>2</sub>/yttria-stabilized-zirconia bilayers on Si(100) substrates. *J. Appl. Phys.* 84 (1998) 4935-4940.
53. Atsushi Mineshige, Minoru Inaba, Shinji Nakanishi, Masafumi Kobune, Tetsuo Yazawa, Kenji Kikuchi, and Zempachi Ogumi. Vapor-Phase Deposition for Dense CeO<sub>2</sub> Film Growth on Porous Substrates. *Journal of the Electrochemical Society* 153 (2006) A975-A981.
54. Ian M. Watson, Matthew P. Atwood, David A. Cardwell and Toby J. Cumberbatch. MOCVD of High-quality YBa<sub>2</sub>Cu<sub>3</sub>O<sub>7-x</sub> Films: in situ Preparation



- of Fluorine-free layers from a Fluorinated Barium Source. *Journal of Materials Chemistry* 4 (1994) 1393-1401.
55. Mohamed Y. El-Naggar, David A. Boyd, and David G. Goodwin.  
Characterization of highly-oriented ferroelectric  $\text{Pb}_x\text{Ba}_{1-x}\text{TiO}_3$  thin films grown by metalorganic chemical vapor deposition. *Journal of Materials Research* 20 (2005) 2969-2976.
  56. Yinzhu Jiang, Haizheng Song, Qianli Ma, Guangyao Meng. Deposition of  $\text{Sm}_2\text{O}_3$  doped  $\text{CeO}_2$  thin films from  $\text{Ce}(\text{DPM})_4$  and  $\text{Sm}(\text{DPM})_3$  by aerosol-assisted metal-organic chemical vapor deposition. *Thin Solid Films* 510 (2006) 88-94
  57. Z. Lu, R.S. Feigelson, R.K. Route, S.A. DiCarolis, R. Hiskes and R.D. Jacowitz.  
Solid source MOCVD for the epitaxial growth of thin oxide films. *Journal of Crystal Growth* 128 (1993) 788-792.
  58. M. Pan, G.Y. Meng, H.W. Xin, C.S. Chen, D.K. Peng, Y.S. Lin. Pure and doped  $\text{CeO}_2$  thin films prepared by MOCVD process. *Thin Solid Films* 324 (1998) 89-93.
  59. V. Selvamanickam, G. Carota, M. Funk, N. Vo, and P. Haldar. High-Current Y-Ba-Cu-O Coated Conductor using Metal Organic Chemical-Vapor Deposition and Ion-Beam-Assisted Deposition. *IEEE Transactions on Applied Superconductivity* 11 (2001) 3379-3381.
  60. Dae-Hwan Kim, Woo-Young Yang, and Shi-Woo Rhee. Low Temperature CVD of  $\text{Pb}(\text{Zr,Ti})\text{O}_3$  Using  $\text{Pb}(\text{tmhd})_2$ ,  $\text{Zr}(\text{dmae})_4$ , and  $\text{Ti}(\text{dmae})_4$ . *Journal of the Electrochemical Society* 150 (2003) C516-A522.

61. M. Pan, G.Y. Meng, H.W. Xin, C.S. Chen, D.K. Peng, Y.S. Lin. Pure and doped CeO<sub>2</sub> thin films prepared by MOCVD process. *Thin Solid Films* 324 (1998) 89-93.
62. Hee-Gyoun Lee, Young-Min Lee, Hyung-Shik Shin, Chan-Joong Kim, Gye-Won Hong. Parameters on the texture development of CeO<sub>2</sub> films directly deposited on a Ni metal substrate by chemical vapor deposition. *Materials Science and Engineering B* 90 (2002) 20-24
63. W.B. Carter, G.W. Book, T.A. Polley, D.W. Stollberg, J.M. Hampikian. Combustion chemical vapor deposition of CeO<sub>2</sub> film. *Thin Solid Films* 347 (1999) 25-30.
64. R. D. Present. *Kinetic theory of gases*. McGraw-Hill (1958).
65. B. Viswanath, Changhyun Ko, and Shriram Ramanathan. Thickness-dependent orientation evolution in nickel thin films grown on yttria-stabilized zirconia single crystals. *Philosophical Magazine* 91 (2011) 4311–4323
66. M. Becht, F. Wang, J.G. Wen, T. Morishita. Evolution of the microstructure of oxide thin films. *Journal of Crystal Growth* 170 (1997) 799-802.
67. Michael Becht and Tadataka Morishita. Thin Film Growth and Microstructure Analysis of CeO<sub>2</sub> Prepared by MOCVD. *Chem. Vap. Deposition* 2 (1996) 191-197.
68. A. G. Zaitsev, G. Ockenfuss, D. Guggi, R. Wördenweber, and U. Krüger. Structural perfection of (001) CeO<sub>2</sub> thin films on (1102) sapphire. *J. Appl. Phys.* 81 (1997) 3069-3072.

69. Z. Shao and S. M. Haile. A high performance cathode for the next generation of solid-oxide fuel cells. *Nature*. 431 (2004) 170-173.
70. William C. Chueh, Chih-Kai Yang, Carol M. Garland, Wei Lai and Sossina M. Haile, *Phys.Chem. Chem. Phys.*, 13 (2011) 6442-6451
71. Avila-Paredes, Hugo J., Chien-Ting Chen, Shizhong Wang, Roger A. De Souza, Manfred Martin, Zuhair Munir, and Sangtae Kim. Grain Boundaries in Dense Nanocrystalline Ceria Ceramics: Exclusive Pathways for Proton Conduction at Room Temperature. *J. Mater. Chem.* 20 (2010) 10110-10112.
72. M. Shirpour, G. Gregori, R. Merkle, and J. Maier. On the proton conductivity in pure and gadolinium doped nanocrystalline cerium oxide. *Phys. Chem. Chem. Phys.* 13 (2011) 937-940.
73. Scherrer, P. *Göttinger Nachrichten*, 2 (1918) 98-100.
74. H. Huang, T. M. Gür, Y. Saito and F. Prinz. High ionic conductivity in ultrathin nanocrystalline gadolinia-doped ceria films. *Appl. Phys. Lett.* 89 (2006) 143107-1 – 143107-3.
75. E. Ballée, A. Ringuedé, M. Cassir, M. Putkonen and Lauri Niinistö. Synthesis of a Thin-Layered Ionic Conductor,  $\text{CeO}_2\text{--Y}_2\text{O}_3$ , by Atomic Layer Deposition in View of Solid Oxide Fuel Cell Applications. *Chem. Mater.* 21 (2009) 4614-4619.
76. J. H. Joo and G. M. Choi. Electrical conductivity of thin film ceria grown by pulsed laser deposition. *J. Eur. Ceram. Soc.* 27 (2007) 4273- 4277.
77. Xin Guo, Wilfried Sigle, and Joachim Maier. Blocking Grain Boundaries in Yttria-Doped and Undoped Ceria Ceramics of High Purity. *J. Am. Ceram. Soc.*, 86 (2003) 77-87.

78. Ted C. Yeh, Nicola H. Perry, and Thomas O. Mason. Nanograin Composite Model Studies of Nanocrystalline Gadolinia-Doped Ceria. *J. Am. Ceram. Soc.* 94 (2011) 1073-1078.
79. J. Fleig. The influence of non-ideal microstructures on the analysis of grain boundary impedances. *Solid State Ionics* 131 (2000) 117-127.
80. Enrique Ruiz-Trejo and John A. Kilner. Possible proton conduction in  $\text{Ce}_{0.9}\text{Gd}_{0.1}\text{O}_{2-\delta}$  nanoceramics. *Journal of Applied Electrochemistry* 39 (2009) 523-528.
81. H. Pöpke, E. Mutoro, C. Raß, B. Luerßen, M. Amati, M.K. Abyaneh, L. Gregoratti, J. Janek. The role of platinum oxide in the electrode system  $\text{Pt}(\text{O}_2)/\text{yttria-stabilized zirconia}$ . *Electrochimica Acta* 56 (2011) 10668-10675.
82. P. Fabry and M. Kleitz. Influence of the metal and the electrolyte composition on the characteristics of the oxygen electrode reaction on solid oxide electrolyte. *Electroanalytical Chemistry and Interfacial Electrochemistry* 57 (1974) 165-177.
83. P. Baker, J. Guindet, and M. Kleitz. Classification Criteria for Solid Oxide Fuel Cell Electrode Materials. *J. Electrochem. Soc.* 144 (1997) 2427-2432.
84. A. Bieberle, L.P. Meier, L.J. Gauckler. The Electrochemistry of Ni Pattern Anodes Used as Solid Oxide Fuel Cell Model Electrodes. *J. Electrochem. Soc.* 148 (2001) A646-A656.
85. B. de Boer. Ph.D. thesis, University of Twente (1998).
86. Kenji A. Sasaki, Yong Hao and Sossina M. Haile. Geometrically asymmetric electrodes for probing electrochemical reaction kinetics: a case study of hydrogen at the  $\text{Pt}-\text{CsH}_2\text{PO}_4$  interface. *Phys. Chem. Chem. Phys.* 11 (2009) 8349-8357.

87. E. C. Brown. *Electrochemically deposited ceria structures for advanced solid oxide fuel cells* Ph.D thesis. California Institute of Technology (2011).
88. Jose Conesa. Computer modeling of surfaces and defects on cerium dioxide. *Surface Science* 339 (1995) 337-352.
89. Friedrich Esch, Stefano Fabris, Ling Zhou, Tiziano Montini, Cristina Africh, Paolo Fornasiero, Giovanni Comelli, and Renzo Rosei. Electron Localization Determines Defect Formation on Ceria Substrates. *Science* 309 (2005) 752-755.
90. J. Newman. Resistance for Flow of Current to a Disk. *J. Electrochem. Soc.* 113 (1966) 501-502.
91. Alexander K. Opitz and Jürgen Fleig. Investigation of O<sub>2</sub> reduction on Pt/YSZ by means of thin film microelectrodes: The geometry dependence of the electrode impedance. *Solid State Ionics* 181 (2010) 684-693.
92. F. S. Baumann, J. Fleig, G. Cristiani, B. Stuhlhofer, H.-U. Habermeier and J. Maier. Quantitative comparison of mixed conducting SOFC cathode materials by means of thin film model electrodes. *J. Electrochem. Soc.* 154 (2007) B931-B941.
93. M.Odgaard and E.Skou. SOFC cathode kinetics investigated by the use of cone shaped electrodes: The effect of polarization and mechanical load. *Solid State Ionics* 86-88 (1996) 1217-1222.
94. William C. Chueh. *Electrochemical and Thermochemical Behavior of CeO<sub>2-x</sub>*. Ph.D thesis. California Institute of Technology (2011).
95. William C. Chueh, Christoph Falter, Mandy Abbott, Danien Scipio, Philipp Furler, Sossina M. Haile, Aldo Steinfeld. High-Flux Solar-Driven

Thermochemical Dissociation of CO<sub>2</sub> and H<sub>2</sub>O Using Nonstoichiometric

Ceria. *Science* 330 (2010) 1797-1801.

96. R. Swanepoel. Determination of the thickness and optical constants of amorphous silicon. *J. Phys. E: Sci. Instrum.* 16 (1983) 1214-1222.
97. Maley, N. Critical Investigation of the Infrared-Transmission-Data Analysis of Hydrogenated Amorphous Silicon Alloys. *Physical Review B* 46 (1992): 2078-2085.
98. R. Swanepoel. Determination of surface roughness and optical constants of inhomogeneous amorphous silicon films. *J. Phys. E: Sci. Instrum.* 17 (1984) 896-903.
99. S.R. Bhattacharyya, R.N. Gayen, R. Paul, and A.K. Pal. Determination of optical constants of thin films from Transmittance trace. *Thin Solid Films* 517 (2009) 5530-5536.
100. R. D. Shannon, R. C. Shannon, O. Medenbach, and R. X. Fischer. Refractive Index and Dispersion of Fluorides and Oxides. *J. Phys. Chem. Ref. Data.* 31 (2002) 931-970.
101. A. Hartridge, M. G. Krishna and A. K. Bhattacharya. Optical constants of nanocrystalline lanthanide-doped ceria thin films with the fluorite structure. *J. Phys. Chem. Solids* 59 (1998) 859-866.
102. R. D. Shannon. Dielectric polarizabilities of ions in oxides and fluorides. *J. Appl. Phys.* 73 (1993) 348-366

103. S. H. Wemple and M. DiDomenico. Behavior of the Electronic Dielectric Constant in Covalent and Ionic Materials. *Physical Review B*. 3 (1971) 1338-1351.
104. P. Patsalas, S. Logothetidis, L. Sygellou and S. Kennou. Structure-dependent electronic properties of nanocrystalline cerium oxide films *Physical Review B*. 68 (2003) 035104-1 – 035104-13.
105. F. Marabelli and P. Wachter. Covalent insulator CeO<sub>2</sub>: Optical reflectivity measurements. *Phys. Rev. B*. 36 (1987) 1238-1243.
106. N. Pryds, K. Rodrigo, S. Linderoth, and J. Schou. On the growth of gadolinia-doped ceria by pulsed laser deposition. *Appl. Surf. Sci.* 255 (2009) 5232-5235.
107. Y. Chang, G. Badano, E. Jiang, J.W. Garland, J. Zhao, C.H. Grein, S. Sivananthan. Composition and thickness distribution of HgCdTe molecular beam epitaxy wafers by infrared microscope mapping. *Journal of Crystal Growth* 277 (2005) 78-84
108. <http://www.wolframalpha.com>
109. Ramos, T., J. Hjelm, and M. Mogensen. Towards Quantification of Relations between Electrode Polarisation and Microstructure. *Journal of the Electrochemical Society* 158 (2011) B814-B824.
110. S. Primdahl and M. Mogensen. Gas Conversion Impedance: A Test Geometry Effect in Characterization of Solid Oxide Fuel Cell Anodes. *Journal of the Electrochemical Society* 145 (1998) 2431-2438.
111. J. Ross Macdonald. *Impedance Spectroscopy: Emphasizing Solid Materials and Systems*. Wiley-Interscience (1987).

112. Bernard A. Boukamp and J. Ross Macdonald. Alternatives to Kronig-Kramers transformation and testing, and estimation of distributions. *Solid State Ionics* 74 (1994) 85-101.
113. Kotaro Onizuka. Computer Experiment on a 3D Site Percolation Model of Porous Materials-Its Connectivity and Conductivity. *Journal of the Physical Society of Japan* 39 (1975) 527-535
114. V. Lucarini, J. J. Saarinen, K.-E. Peiponen, and E. M. Vartiainen, *Kramers–Kronig Relations in Optical Materials Research*. Springer (2005).
115. C. F. Bohren and D .R. Huffman. *Absorption and Scattering of Light by Small Particles*. Wiley-Interscience (1983).
116. D. Stroud. Generalized effective-medium approach to the conductivity of an inhomogeneous material. *Phys. Rev. B*. 12 (1975) 3368-3373.
117. W. M. Merrill, R. E. Diaz, M. M. LoRe, M. C. Squires, and N. G. Alexopoulos, Effective Medium Theories for Artificial Materials Composed of Multiple Sizes of Spherical Inclusions in a Host Continuum. *IEEE Transactions on antennas and propagation* 47 (1999) 142-148
118. E. Barsoukov, J. R. Macdonald, *Impedance spectroscopy: theory, experiment, and applications*. Wiley-Interscience (2005).
119. H. Looyenga, Dielectric Constants of Heterogeneous Mixtures. *Physica* 31 (1965) 401-406.
120. L. D. Landau and E. M. Lifshitz, *Electrodynamics of Continuous Media*. Pergamon (1984).



121. E. Bontempi, "X-Ray Reflectivity for the characterization of thin films" in *Recent Research Development in Chemical Physics*, Transworld Research Network (2004).